

122

RCA Review

March 1970 Volume 31 No. 1

GIFT OF RG 174-249
Lohnes and Culver

TO THE
BROADCAST PIONEERS LIBRARY
1771 N STREET, N.W., WASHINGTON, D. C. 20036

10/13/88

RCA Review, published quarterly in March, June, September, and December by RCA Research and Engineering, RCA Corporation, Princeton, New Jersey 08540. Entered as second class matter July 3, 1950 under the Act of March 3, 1879. Second-class postage paid at Princeton, New Jersey, and at additional mailing offices. Subscription price in the United States and Canada: one year \$4.00, two years \$7.00, three years \$9.00; in other countries, one year \$4.40, two years \$7.80, three years \$10.20. Single copies up to five years old \$2.00. For copies more than five years old, contact Walter J. Johnson, Inc., 111 Fifth Ave., New York, N. Y. 10003.

RCA Review

A technical journal published quarterly
by RCA Research and Engineering
in cooperation with the subsidiaries
and divisions of RCA.

Contents

- 3** Fabrication and Performance of Kilowatt L-Band Avalanche Diodes
S. G. Liu and J. J. Risko
- 20** High-Power L- and S-Band Transferred Electron Oscillators
B. E. Berson, R. E. Enstrom, and J.F. Reynolds
- 39** Sonic Film Memory
R. Shahbender, P. Herkart, K. Karstad,
K. Kurlansik, and L. Onyshkevych
- 60** Electron Optics and Signal Read-Out of High-Definition
Return-Beam Vidicon Cameras
O. H. Schade, Sr.
- 120** Stable Solid-State Vertical Deflection for High-Definition
Television Systems
O. H. Schade, Jr.
- 148** Linear Solid-State Horizontal Deflection Circuit for
High-Definition Television Systems
O. H. Schade, Jr.
- 171** RCA Technical Papers
- 173** Patents
- 175** Authors

RCA Corporation

Robert W. Sarnoff Chairman of the Board and President
Elmer W. Engstrom Chairman of the Executive Committee of the Board

Editorial Advisory Board

Chairman, J. A. Rajchman RCA Laboratories
E. D. Becken RCA Communications
G. H. Brown RCA Patents and Licensing
A. L. Conrad RCA Education Systems
H. L. Cooke, RCA Research and Engineering
A. N. Goldsmith Honorary Vice President, RCA
N. L. Gordon RCA Laboratories
G. B. Herzog RCA Laboratories
J. Hillier RCA Research and Engineering
R. S. Holmes RCA Research and Engineering
E. O. Johnson RCA Electronic Components
H. W. Leverenz RCA International Licensing
H. R. Lewis RCA Laboratories
D. S. McCoy RCA Laboratories
L. S. Nergaard RCA Laboratories
H. F. Olson RCA Laboratories
K. H. Powers RCA Laboratories
P. Rappaport RCA Laboratories
F. D. Rosi RCA Laboratories
L. A. Shottliff RCA International Licensing
T. O. Stanley RCA Laboratories
W. M. Webster RCA Laboratories
L. R. Weisberg RCA Laboratories

Secretary, Charles C. Foster RCA Research and Engineering

Editor Ralph F. Ciafone

Associate Editors

W. A. Chisholm RCA Limited
D. B. Dobson Aerospace System Division
M. G. Gander RCA Service Company
J. Gold Graphic Systems Division
T. G. Greene Missile and Surface Radar Division
W. O. Hadlock RCA Research and Engineering
W. A. Howard National Broadcasting System
C. Hoyt Consumer Electronic Systems Division
C. A. Meyer RCA Electronic Components
M. G. Pietz Defense Engineering
D. R. Pratt Commercial Electronic Systems Division
C. W. Sall RCA Laboratories
I. M. Seideman Astro-Electronics Division

Fabrication and Performance of Kilowatt L-Band Avalanche Diodes*[†]

S. G. Liu and J. J. Risko, RCA Laboratories, Princeton, N. J.

Abstract—A reliable process for the fabrication of high-efficiency high-power avalanche-diode oscillators is described. The key step in the process is a deep diffusion of boron into high-resistivity silicon epitaxial wafers. Such junctions have been found to be consistently free of microplasma effects and capable of handling high avalanche current, which is one of the essential requirements of the high-efficiency high-power avalanche-diode oscillator. Using these diodes in a multiple-stacked configuration, we have reached a 1.2 kW power output at 1.11 GHz with an efficiency of 25.6%. This power level is suitable for such applications as IFF transponder systems.

Combined power output has been obtained from series-connected, as well as from parallel-connected, diodes. The diodes have been operated in both simple coaxial circuits and microstrip circuits. The circuit impedance presented at the position of the diode has been computed for varying circuit parameters.

Introduction

The high-efficiency mode of oscillation in avalanche diodes was discovered at RCA Laboratories.¹ It was found that when a threshold current level is reached in a certain type of reverse-biased avalanche diode, rf oscillation is observed, accompanied by an abrupt decrease in average voltage across the diode and an increase in average current. The frequency of this "anomalous-mode" oscillation is much lower than the corresponding transit-time frequency of the diode; the power output and the efficiency are many times greater than those of the IMPATT diode oscillator.² Proposed theories as well as experimental evidence have indicated³⁻⁷ that support of higher-order harmonics, in-

* The research reported in this paper was jointly sponsored by the Air Force Avionics Laboratory, Wright-Patterson Air Force Base, Ohio, under Contract F33615-68-C-1688, the Sandia Corporation, Albuquerque, New Mexico, under Contract 57-6779, and RCA Laboratories, Princeton, N.J.

[†] A major portion of this paper was presented at the international Electron Device Meeting, Washington, D.C., Oct. 1969.

cluding the transit-time frequency, are necessary for this high-efficiency mode of oscillation.

Combined power output has been obtained from both series-connected and parallel-connected diodes, and series-connected diodes have been operated in both simple coaxial circuits and microstrip circuits. The circuits are capable of matching to the diode over a wide impedance range at the fundamental frequency, and simultaneously supporting the required higher-order harmonic frequencies. The circuit impedance presented at the position of the diode has been computed for varying circuit parameters.

The best duty cycle achieved with the present series-stacked geometry at the kilowatt level is 0.1%. With improved packaging and heat-sinking techniques, operation at 1% duty cycle should be possible. Methods of improving heat dissipation are discussed.

Device Fabrication

High-power high-efficiency avalanche diodes operating at L-band frequencies have the following salient features.³ First, the n-region of the diode has a low doping density. Secondly, the width of the n-region is narrower than the corresponding depletion width of the n-region at breakdown. Thus, the depletion layer sweeps across the n-region, i.e., the diode "punches through", before reaching the point of avalanche breakdown. Thirdly, the diode must be capable of handling high avalanche current.

A reliable fabrication process has been developed that satisfies these requirements and produces diodes capable of power outputs up to the 200-W level. The key element of the diodes is a deeply diffused junction. Such junctions have been found consistently to be free from microplasma effects and capable of handling high avalanche currents. Typical diffusion depths range from 8 to 15 microns. On the other hand, abrupt junctions formed by shallow diffusion from a high-surface-concentration source into high-resistivity materials are found, in general, to display microplasma effects and burn out easily.

Epitaxial Material

The fabrication process starts with silicon epitaxial wafers consisting of an n-layer on heavily doped n-type substrates. The resistivity and thickness of this n-layer are controlled during crystal growth. Epitaxial material is used because the doping density of a thin n-layer can be held uniform across the whole wafer. Silicon epitaxial wafers grown at RCA Electronic Components, Somerville,

New Jersey, have given excellent results in device performance and yield. The epitaxial layer is phosphor doped. Typical resistivity is 4 to 7 ohm-cm, and the layer thickness is 12 to 23 microns. The substrate is antimony doped, and the resistivity is between 0.005 and 0.01 ohm-cm. Both (111) and (100) oriented wafers have been used successfully in diode fabrication.

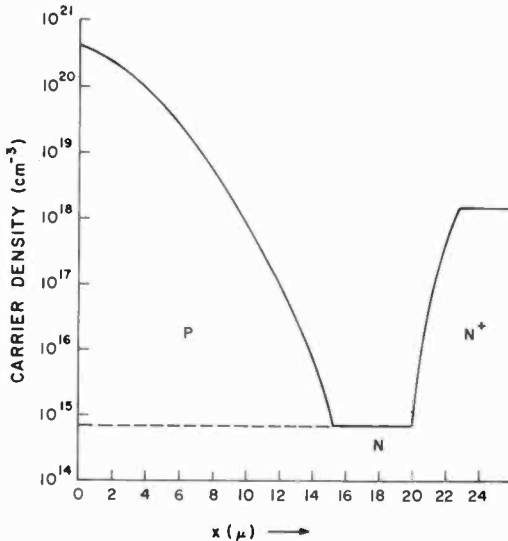


Fig. 1—Diffusion profile of "anomalous-mode" diode with a deep-diffused junction.

Deep Diffusion

A boron silicate glass is deposited onto the silicon wafer at 720°C. Diffusion of boron into the wafer at 1150°C follows. With precise control of the diffusion time, the diffusion depth, and hence the thickness of the n-layer, can be controlled within 0.5 micron. The precise control of the undiffused n-layer is essential to diode performance as a high-power microwave oscillator. An example of the diffusion profile assuming a complementary error-function distribution is shown in Fig. 1. A net undiffused n-region of 4 to 6 microns is desired for diodes operating around 1 GHz. The depletion width at breakdown will extend slightly into the graded p and n⁺ regions. This depletion width can be calculated from the capacitance measured at breakdown and diode dimensions. The calculated depletion width is about 2 microns wider than the undiffused n-region. It should be

noted that the diode has a graded p , as well as a graded $n-n^+$ region; the latter is a result of out-diffusion from the n^+ -substrate.

The fact that deep-diffused diodes with graded junctions have high current-handling capacity was shown in the following experiment. A silicon epitaxial wafer with a 6 ohm-cm epi-layer was sliced into six sections. Each section was diffused from a high-surface-concentration source for a different length of time at the same temperature. Large-size (0.020-inch diameter) diodes were then made from each section of the diffused wafers, and the I - V characteristics of the diodes were examined on a curve tracer. It was found that shallow diffused diodes, up to a depth of about 8 microns, show microplasma effects and burn-out at low current levels. The diodes diffused for longer time showed no microplasma effects and took much higher avalanche current. A comparison of I - V characteristics of a 4-hour-diffused diode, and an 8-hour-diffused diode is shown in Fig. 2.

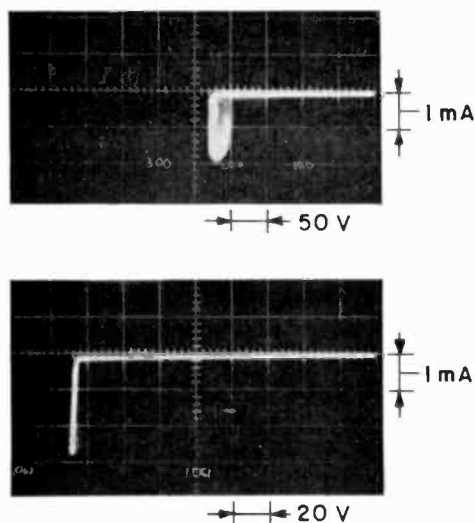


Fig. 2—Reverse-biased I - V characteristics of (top) shallow-diffused diodes showing microplasma effect, and (bottom) deep-diffused diodes showing no microplasma effect.

The diffusion process was followed by steps of metalization, masking (with a photoresist), and chemical etching to obtain disk-shaped diode chips. A cross-sectional drawing of the finished disk configuration is shown in Fig. 3.

The disk-shaped chip has a larger diameter on the p -side than on the n -side. This shape is produced by etching from the substrate

straight through the wafer. The wafer thickness is reduced to about 3 mils before metalization and etching. The disk configuration has several advantages. The larger diameter on the p-side facilitates handling and reduces possible mechanical damage of the junction when the chips are mounted p-side down for better heat sinking. Furthermore, the increased length at the edge of the junction reduces the electric field strength in this region and thus reduces the possibility of burnout. Diodes made with this process have operated at current levels of 10 A and produced power outputs of 200 W, as described later.

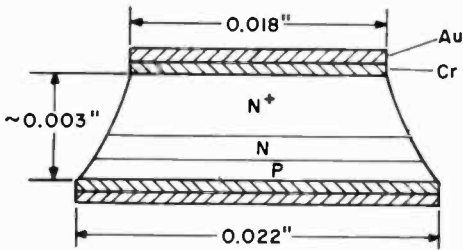


Fig. 3—Disk-shaped diode chip.

Device Testing

The power output from individual diodes using the deep-diffusion process ranges between 100 and 200 W, and efficiencies range from 25% to 40%. Combined power outputs have been obtained from diodes connected in series as a multiple-stacked unit.⁸ With this technique, a power level of 1.2 kW has been achieved, the first time that the kilowatt power level has been reached in these devices. Because the diodes are current-controlled, series operation is preferred to parallel operation. In a series string, all pass the same current, and the voltage division between diodes in the string is automatic; in a parallel set, all diodes see the same voltage, and individual currents may vary greatly. Series operation of diodes has been demonstrated in micro-strip, as well as in coaxial, circuits.

A block diagram of the experimental apparatus used for power and frequency measurements is shown in Figure 4. Precision calibrated attenuators and a peak power meter were used for accurate power measurement. The precision attenuator has a flat attenuation between dc and 12.4 GHz. A wavemeter connected between the crystal detector output and the oscilloscope is used for frequency measurement. The

pulsed rf output is also monitored on a spectrum analyzer, which is not shown in the diagram. The power rating of the attenuators has become important in high-power measurements. The power output from the five-stacked diodes burned out a medium-power attenuator that was rated at 1-kW peak power. Attenuators rated at 2 kW are presently used in power measurement.

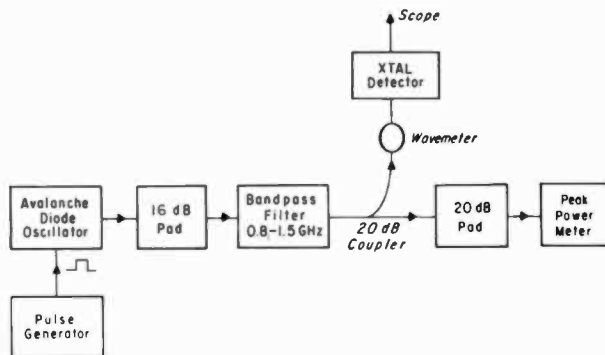


Fig. 4—Experimental setup for measurement of power and frequency.

A filter with a pass band from 0.8 to 1.5 GHz was included in the setup to ensure that only fundamental power was measured. Even without the external filter, the second-harmonic content in the output is usually more than 15 dB below the fundamental for diodes operating in the range of 1.0 to 1.5 GHz. The pulser has an internal impedance of 200 ohms, which is high compared to that of the diodes (~ 10 ohms). The use of a high-impedance pulse generator minimizes the sometimes self-destructive jump in current as the anomalous mode current threshold is exceeded.

The circuit in which the series-stacked diodes were tested consists of a coaxial line with a movable short-circuit and a low-pass-filter tuning section, as reported by Levine and Liu.⁹ A schematic diagram of the circuit is reproduced in Fig. 5. The circuit is capable of matching the diode impedance at the fundamental frequency, while simultaneously supporting the higher harmonics with a reactive termination. The main line has 50 ohms surge impedance, while the tuning section is formed by a length of 125-ohm impedance line and a lumped variable capacitor. The distances from the short circuit to the diode and from the tuning section to the diode determine the oscillation frequency of the diode within its range of oscillation.

Due to the simplicity of the circuit, the impedance presented at the

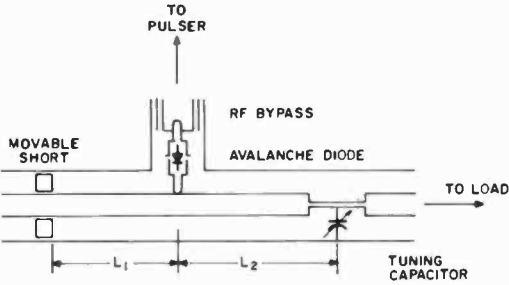


Fig. 5—Schematic diagram of L-band avalanche-diode oscillator.

position of the diode can be easily calculated for varying circuit parameters and frequencies. Such calculated results would provide information on the diode impedance when circuit parameters under optimum power output conditions are known, or vice versa. Fig. 6 shows the calculated impedance variation on a Smith chart, normalized to 50 ohms, for various positions of the short circuit and the tuning section. The frequency is chosen at 1 GHz, and the impedance of the tuning

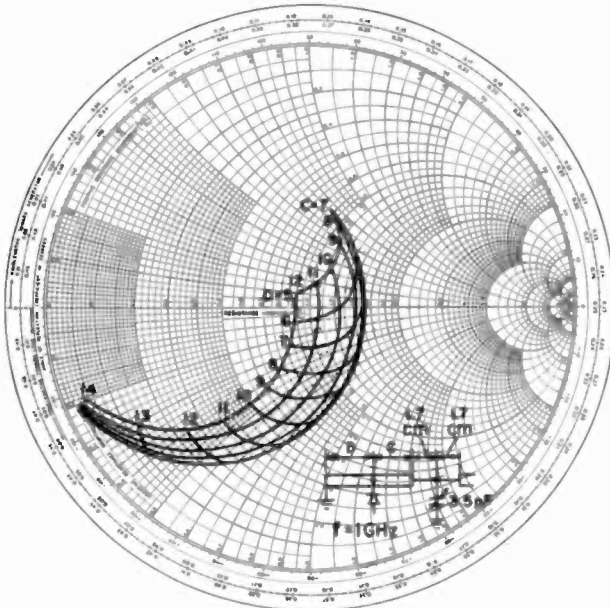


Fig. 6—Impedance calculation with varying positions of short-circuit and tuning section with respect to the diode.

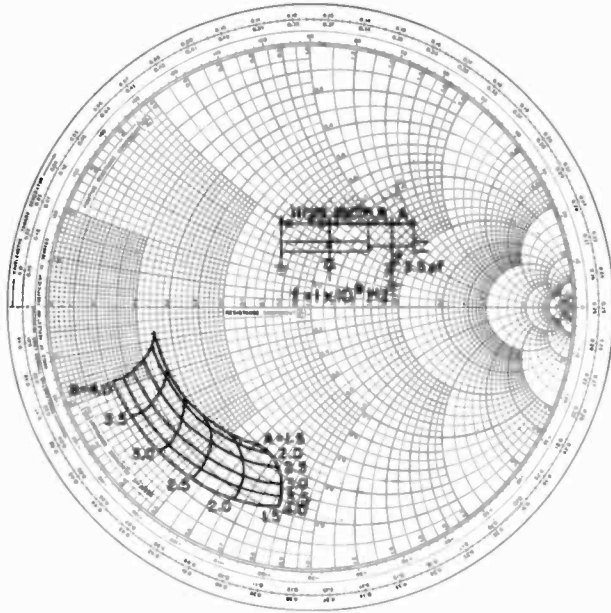


Fig. 7—Impedance calculation with varying length in tuning section.

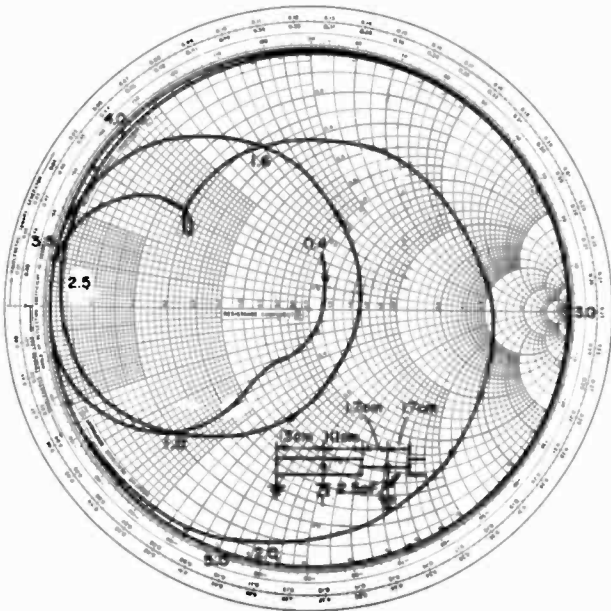


Fig. 8—Impedance calculation with varying frequency.

section is fixed as shown in the figure. The curves show that the circuit is capable of matching to the diode at a wide range of impedance levels. Fig. 7 shows the impedance variation with various lengths of high-impedance line in the tuning section. The frequency and other circuit parameters are fixed as shown. Fig. 8 shows the calculated impedance presented at the position of the diode for a frequency variation from the fundamental through its fifth harmonic. Circuit parameters in this case are fixed and are taken from experimental settings. At harmonic frequencies, the impedances appear to be purely reactive.

Series Configuration

The configuration of a multiple-stacked diode unit is shown in Fig. 9, where five diodes are series-connected in the single package. Individual diode chips are first mounted in pillboxes, which are then inserted into a modified 1N23 rectifier cartridge. The stacked geometry has the advantage that it can be treated as a single unit for the circuit, while each diode can easily be separated for testing or replacement. A schematic drawing of the pillbox with a disk-shaped diode mounted inside is also shown.

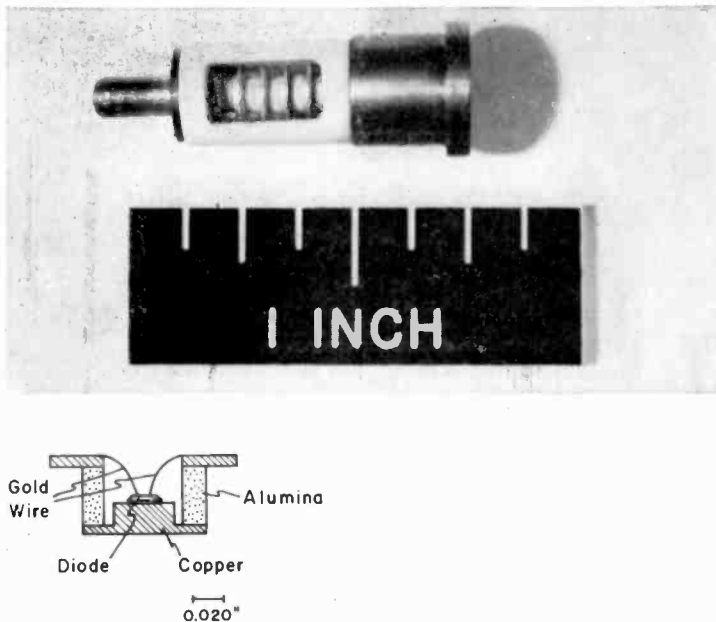


Fig. 9—Photograph of a kilowatt series-stacked five-diode unit and schematic of pill-box with a diode chip mounted inside.

Fig. 10 shows the power output and efficiency of several five-stacked units in the coaxial circuit described above with optimized circuit parameters. The data are plotted against pulsed current passing through the diodes. The maximum power output of all units is above 1 kW, and the efficiency about 25%. The best stacked-unit out of five units tested produced a power output of 1.2 kW with an efficiency of 25.6%. The operating frequency was 1.109 GHz. The upper current

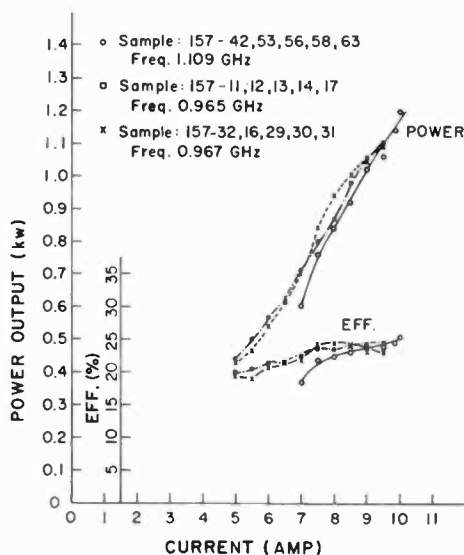


Fig. 10—Power output and efficiency versus current of several series-stacked five-diode units.

level approaches the limit of the pulser. The power output shows no sign of saturation at this current level. Individual diodes can usually take about 12 A before burning out.

The above results were obtained under pulsed conditions with a pulse width of 0.5 microsecond and a repetition rate of 400 Hz. The average voltage across the five series-stacked diodes typically drops from 680 V at breakdown to 460 V during oscillation. The applied pulse current through the diode and the corresponding detected microwave envelope at a power level of 1.2 kW are shown in Fig. 11; the corresponding $\sin x/x$ frequency spectrum is shown in Fig. 12.

One feature that seems particularly interesting is that the selection of diodes for series operation is not critical. Table I shows a summary of performance of four five-stacked units. It should be noted that al-

Table I—Summary of Performance of Four Five-Diode Series-stacked Units.

Five-Diode Units	P_{out} (kW)	Frequency (GHz)	Efficiency (%)	Breakdown Voltage Range (V)
1	1.20	1.109	25.6	124 ~ 128
2	1.00	0.965	22.0	132 ~ 140
3	1.09	0.967	23.0	128 ~ 140
4	1.10	0.965	24.6	132 ~ 140

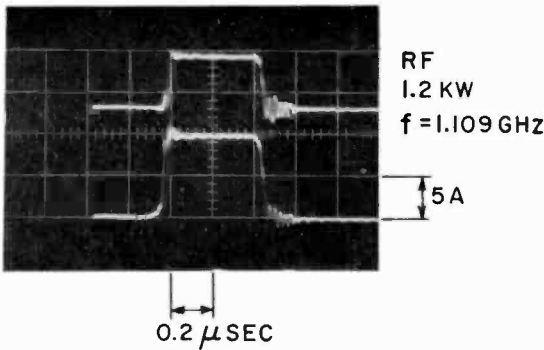


Fig. 11—Waveforms of rf envelope at 1.2 kW, 1.109 GHz (top), and current (bottom) for a series-stacked five-diode unit. Scale: current — 5 A/cm; time — 0.2 $\mu\text{s/cm}$.

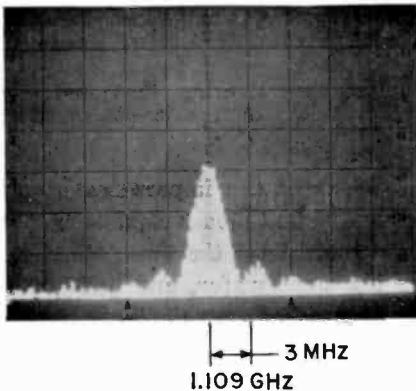


Fig. 12—Frequency spectrum of pulsed power output at 1.1 kW. Center frequency: 1.109 GHz; horizontal scale: 3 MHz/division.

though the breakdown voltages of the diodes varied between 128 and 140 volts, they still operated satisfactorily in series.

Series-connected diode oscillators increase the operating impedance level, a feature that is generally desirable in the circuit design. The circuit impedance seen by the diode and package has been measured on a network analyzer using a probe inserted in place of the diode after the circuit has been tuned for optimum power. Assuming that the circuit presents the negative of the large-signal diode impedance, the impedance of a two-stacked unit including package has a resistance of about -20 ohms, a three-stacked unit -28 ohms, and individual diodes in package -8 to -12 ohms. The susceptances are small at the measuring frequency. It is seen that the increase in circuit impedance is approximately proportional to the number of diodes stacked in series. This measurement was performed on earlier three-stacked units. The diameter of these diodes was 0.018 inch, which is smaller than that used in the five-stacked kW units.

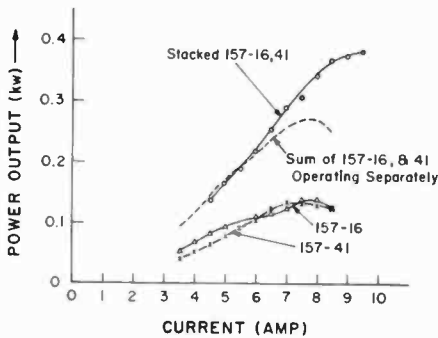


Fig. 13—Power output versus current showing that individual diodes saturate at a lower current level than series-connected diodes.

Another experiment that indicates the importance of circuit impedance level was performed. Individual diodes capable of 200 W were tested in the circuit that is best suited for the five-stacked diodes. All diodes were fabricated from the same wafer, and had a diameter of 0.022 inch. It is noteworthy that, of the four diodes tested, individual diodes showed power saturation at a lower current level than when the diodes were series connected. This result is shown in Fig. 13, where two lower curves show the power output of two diodes measured separately, and the solid curve on the top shows the measured power when

two diodes are stacked in series. The curve for the sum of the individual power outputs shows saturation at a current level where the stacked diodes continue to show a power increase.

The capability of frequency tuning of the series-stacked diode units has been studied experimentally. The frequency was varied in steps by varying the positions of the tuning section and the short-circuit with respect to the diode. A unit with five series-stacked diodes was tested at a current level of 8.5 A. Fig. 14 shows the results of the power output versus frequency for a given series-stack. The frequency extends

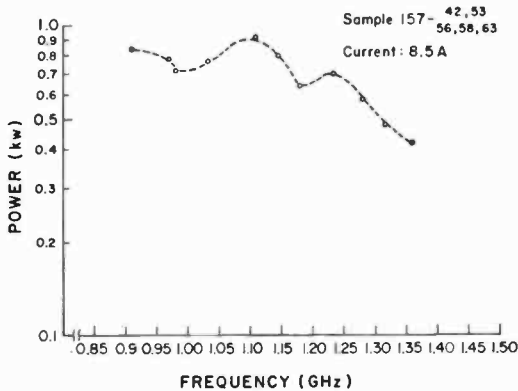


Fig. 14—Power output versus frequency of a series-stacked five-diode unit.

from 0.9 to 1.3 GHz, with a variation in power output of about 2 dB. The upper level of the power is about 800 W to 900 W. The somewhat reduced tuning range compared to the case of a single diode⁹ is not surprising, because the diodes are not identical, and do not all have the same preferred frequency.

The circuit and the series-stacked geometry described above work excellently at the kilowatt level. However, the diodes are difficult to heat sink for high-duty cycle operation. The best duty cycle achieved with five-stacked diodes in the present package, operating at the kilowatt level was 0.1%. With improved mounting, packaging, and heat-sinking techniques, it is believed that one can increase the duty cycle to, say, 1%, without much difficulty. Such techniques may require the use of insulating mounting materials of high thermal conductivity, such as berillium oxide. Using such techniques, dissipation of power up to 70 W has been demonstrated in series-connected varactor diodes.¹¹

Parallel Configuration

As pointed out previously, parallel operation of the "anomalous-mode" diodes is more difficult to achieve. However, parallel-connected chips have been successfully demonstrated.

Fig. 15 shows four chips connected in parallel in a large-size varactor package. A total power of 300 W was measured at a fre-

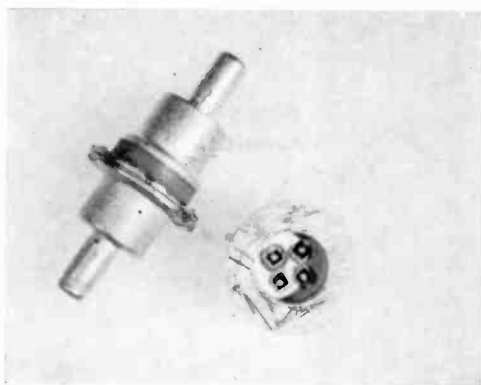


Fig. 15—Four parallel-connected diode chips in a large varactor package.

quency of 1.57 GHz and a total current of 16 A. The chips used were mesa structures. The power output of individual chips from the wafer was about 100 W at a 4 A current level. One possible reason for the lower power output obtained with paralleled diodes may be that the lower impedance is difficult for the circuit to match. It appears, however, that with care, a combination of series- and parallel-connected diodes may be used to achieve much higher power level while maintaining a suitable operating impedance level.

Microstrip Circuit

Series operation of the high-efficiency avalanche-diode oscillators has also been achieved on microstrip circuits.¹⁰ The circuit operates on the same principle as the coaxial circuit described above. A schematic diagram of the circuit with a " π " type low-pass-filter tuning section is shown in Fig. 16. The capacitance tuning elements are thin gold-plated steel plates that are held in position by magnetic bars placed underneath the substrate. Details of the circuit are given in Ref. [10].

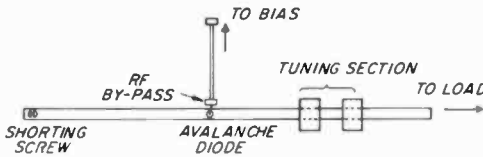


Fig. 16—Schematic diagram of microstrip high-efficiency avalanche-diode oscillator circuit with a “ π ” tuning section.

The circuit has been modified slightly for mounting more than one diode. Details of two series-connected diodes on the microstrip line are shown in Fig. 17. Each diode chip was first mounted in a pillbox, then connected in series with a gold strip. Diode chips have also been soldered directly onto the line.

Fig. 18 shows results obtained with two series-connected diodes and three series-connected diodes on the microstrip circuit. Power and efficiency are 330 W at 20.2% and 440 W at 23.4%, for the two and three series-connected diodes, respectively. Recently, four series-connected diodes have produced 540 W. The third and fourth diodes were located on top of one of the other diodes.

A comparison has been made between the performance of the microstrip circuit and the coaxial circuit. Power output from the same two series-connected diodes was measured on both circuits. The results are plotted in Fig. 19. It shows that at a current level of 7.5 A, the microstrip circuit performs as well as the coaxial-line circuit. However, the power output becomes jittery and difficult to tune beyond this current level on the microstrip circuit, while the power is still increasing in the coaxial circuit. This may be because fine tuning, such as varying the position of the short-circuit and/or the value of capacitor, is more difficult on the microstrip circuit.

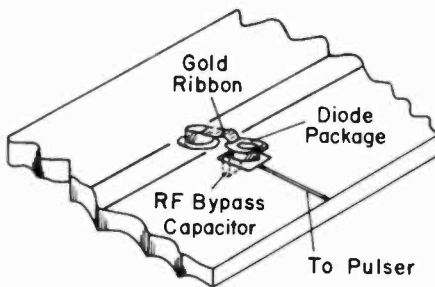


Fig. 17—Details of two series-connected diodes on microstrip circuit.

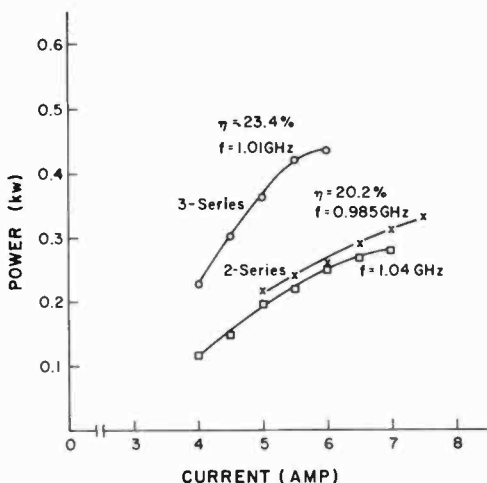


Fig. 18—Power output versus current of series-connected diodes operating on microstrip circuit.

Conclusions

A reliable fabrication process has been developed for high-power high-efficiency avalanche diode oscillators by deep diffusion of boron into high-resistivity n-type epitaxial materials. The large-size deeply diffused diodes have been shown to be consistently free from micro-

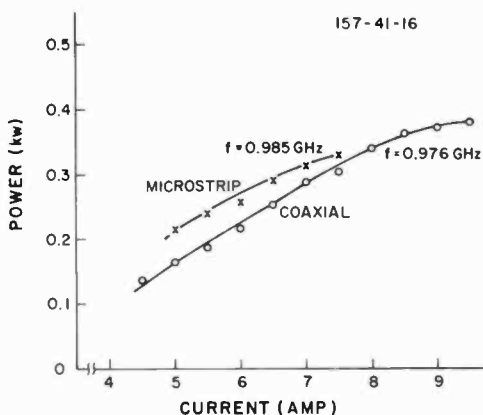


Fig. 19—Comparison of power output of two series-connected diodes on coaxial and microstrip circuits. The coaxial circuit was not retuned for optimum power below 8 A.

plasma effects and capable of handling high currents. Diodes are made in disk shape for convenience in flip-chip mounting for improved heat sinking.

Using these diodes we have demonstrated the feasibility of extending the power output from high-efficiency avalanche-diode oscillators to the kilowatt range. Power outputs up to 1.2 kW at 1.11 GHz with an efficiency of 25.6% has been obtained from five series-connected diodes in a multiple-stacked configuration. Best duty cycle achieved at the kilowatt level is 0.1%; with improved packaging and heat sinking techniques, 1% duty cycle at this power level should be feasible. Experiments have also demonstrated combined power output from parallel-connected diodes and from series-connected diodes on a microstrip circuit up to the 500 W level.

Acknowledgment

The authors wish to thank K. K. N. Chang for his constant encouragement, and L. S. Nergaard for critical reading of the manuscript.

References

- ¹ H. J. Prager, K. K. N. Chang, and S. Weisbrod, "High-Power High-Efficiency Silicon Avalanche Diodes at Ultra High Frequencies," *Proc. IEEE*, Vol. 55, p. 586 (1967).
- ² W. T. Read, "A Proposed High-Frequency Negative-Resistance Diode," *Bell System Tech. Jour.*, Vol. 37, p. 401 (1958).
- ³ S. G. Liu and J. J. Risko, "High-Power Punch-Through Avalanche Diode Microwave Oscillators," Presented at the ISSCC in Philadelphia, Feb. 1968; S. G. Liu, *IEEE Jour. Solid State Circuits*, Vol. SC-3, p. 213 (1968).
- ⁴ R. L. Johnston, D. L. Scharfetter, and D. J. Bartelink, "High-Efficiency Oscillations in Germanium Avalanche Diodes Below the Transit-Time Frequency," *Proc. IEEE*, Vol. 56, p. 1611 (1968).
- ⁵ C. P. Snapp, L. A. Stark, and B. Hoefflinger, "Performance and Theory of Avalanche Resonance Pumped Impatt Oscillators," presented at the Inter. Elec. Device Meeting, Washington, D. C., Oct. 1968.
- ⁶ D. E. Iglesias and W. J. Evans, "High-Efficiency CW Impatt Operation," *Proc. IEEE*, Vol. 56, p. 1610 (1968).
- ⁷ A. S. Clorfeine, R. J. Ikola, and L. S. Napoli, "A Theory for the High-Efficiency Mode of Oscillation in Avalanche Diodes," *RCA Review*, Vol. 30, p. 397 (1969).
- ⁸ S. G. Liu, "Stacked High-Power Avalanche-Diode Oscillators," *Proc. IEEE*, Vol. 57, p. 707 (April, 1969).
- ⁹ P. A. Levine and S. G. Liu, "Tunable L-Band High-Power Avalanche-Diode Oscillator," *Digest Tech. Papers, ISSCC*, Vol. XII, p. 84 (Feb. 1969).
- ¹⁰ S. G. Liu, "Microstrip High-Power L-Band Avalanche-Diode Oscillators," *IEEE-MTT Symposium Digest*, p. 261, May 1969, Dallas, Texas. Also *IEEE Trans. MTT*, Vol. MTT-17 (Dec. 1969).
- ¹¹ D. D. Tang, "High Power Varactor Package for Multichip Application," *Proc. IEEE*, Vol. 57, p. 799 (May, 1969).

High-Power L- and S-Band Transferred-Electron Oscillators*

B. E. Berson, R. E. Enstrom†, and J. F. Reynolds

RCA Electronic Components, Princeton, N. J.

Abstract—High-power high-efficiency transferred-electron oscillators have been developed for both L- and S-band. Development of these devices has required a comprehensive technology involving GaAs materials, fabrication techniques, and circuit requirements. The material parameters for optimum device performance are derived from finished device results. The effect of process variables such as purity of the starting gases, composition of the reactor tube, and As/Ga ratio on carrier concentration and mobility are described. Careful control of these variables has led to the reproducible growth of high-quality GaAs layers. A technology for the fabrication of single and multi-chip high power oscillators has been developed. This has led to devices with power outputs of over 200 watts and efficiencies of over 32%. This is the highest efficiency ever reported for a transferred-electron oscillator. An investigation of circuit requirements has led to the development of a coaxial circuit that allows for high-efficiency operation by providing for both fundamental and harmonic tuning. Finally, the stability of the transferred-electron oscillators with respect to variations in temperature and duty cycle has shown these devices to be suitable for application in many microwave systems.

Introduction

The potential of transferred-electron devices for microwave systems applications is well established.¹⁻³ Devices fabricated from bulk GaAs have given kilowatts of power at frequencies ranging from L- to X-band, although with efficiencies less than 10%. Devices fabricated from epitaxial GaAs have given hundreds of watts with higher efficiencies in the same frequency range. While such results have been obtained in the laboratory, these devices have not been fully utilized in

* This work was supported by the U.S. Air Force Avionics Laboratory under Contract No. F33615-67-C-1981.

† RCA Laboratories, Princeton, N. J.

systems applications because of problems in materials technology. Since bulk material is heavily compensated and has a negative temperature coefficient of resistance, devices fabricated from this material are limited to very-low-duty-cycle pulsed operation. Epitaxial material has a positive temperature coefficient of resistance and thus can be operated at high duty cycles, or even continuously. As a result, most applications utilize epitaxial devices. The growth of high-quality epitaxial material in a reproducible manner can, however, be a problem.

This paper describes research aimed at producing high-power high-efficiency L- and S-band transferred-electron oscillators (TEO's). Present research efforts are directed toward developing the materials technology for the reproducible growth of epitaxial GaAs wafers. In addition, we have developed a device fabrication technology and microwave circuit technology to properly utilize these devices. These studies have resulted in output powers of 200 watts or more and efficiencies greater than 29% in both L- and S-bands. These conversion efficiencies are the highest reported to date for TEO's.

Epitaxial Gallium Arsenide Growth Technology

The basic TEO structures are grown in the form of n^+nn^+ epitaxial GaAs wafer sandwiches⁴ by the arsine vapor-growth process.⁵ The n^+ layers form the ohmic contacts to the active n layer, and, in turn, good metallic contact can be made to these n^+ layers. The use of an n^+nn^+ structure was desirable to eliminate problems in contacting the n layer. The entire structure is grown in a single operation without removing the sample from the apparatus. The initial objective for the carrier concentration of the n layer was approximately $5 \times 10^{14} \text{cm}^{-3}$ in order to obtain an nL product in the range predicted by computer studies.⁶ In addition, growth conditions that resulted in a controlled and reproducible growth rate were desired.

The principles of the growth method can be outlined briefly with the help of Fig. 1. At one end of a 1-inch-diameter quartz tube, high-purity HCl reacts with 99.9999% pure Ga to form GaCl. The GaCl is carried by high-purity, palladium-diffused hydrogen to the deposition zone at the other end of the tube, which contains the substrate. Simultaneously, semiconductor-grade AsH_3 flows into the tube and dissociates into H_2 and arsenic vapor, which reacts with GaCl in the deposition zone. The GaAs thus formed grows epitaxially on the GaAs substrate. The n^+ layer is prepared by doping during growth with gaseous selenium (from H_2Se) to about 3×10^{18} electrons cm^{-3} .

The $n^{+}nn^{+}$ multilayer structure is grown on a chemically polished $\langle 100 \rangle$ oriented, high-conductivity GaAs substrate having a carrier concentration of about 1×10^{18} electrons cm^{-3} . This substrate must be of high quality and is typically about 3 cm^2 in area. The active n layer is grown about 100 microns thick to achieve operation at 1 GHz.

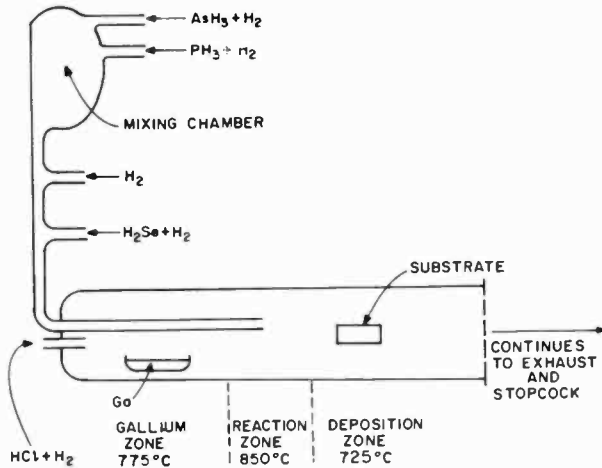


Fig. 1—Schematic representation of vapor-deposition apparatus.

An active n layer of very high purity is desirable for high-power TEO's so that high-resistivity material with the proper nL product ($\sim 5 \times 10^{12} \text{ cm}^{-2}$) and with a positive temperature coefficient of resistivity can be attained without sacrificing electron mobility. A reduced mobility can increase the threshold voltage (V_{TH}) and thus lead to decreased efficiency. The positive temperature coefficient of resistivity is a necessity for high-ambient-temperature and high-duty-cycle operation of devices. The required purity level must also be attained in a reproducible manner. This can be difficult, since the impurity concentration is on the order of 10 parts per billion ($5 \times 10^{14} \text{ cm}^{-3}$).

The initial step taken toward attaining higher purity levels was to eliminate subtle sources of contamination coming either from the source gases or the reactor chamber itself. Semiconductor-grade reagents (AsH_3 , PH_3 , Ga and palladium-diffused H_2) were used exclusively. The main contamination suspect was the HCl , which is only 99.99% pure. By careful selection of the best cylinders of HCl from three different manufacturers, the carrier level has been reproducibly

reduced by an order of magnitude to $n = 3.5 \times 10^{14} \text{ cm}^{-3}$. This corresponds to a resistivity of about 2 ohm-cm and a mobility of up to 6800 $\text{cm}^2/\text{V-sec}$ at 300°K and up to 64,000 $\text{cm}^2/\text{V-sec}$ at 77°K. The mobility at 77°K is a sensitive measure of the purity of the material, as it increases with increased purity. The close agreement in the carrier levels and mobility values for 2 of the 3 tanks, shown in Table I, demonstrates that increased control of HCl purity has been achieved. High-purity GaAs can now be attained on a more reproducible basis than was previously possible.⁴

Table I—Characteristics of GaAs Prepared from HCl from three Different Manufacturers.

Run	T (°K)	n (cm^{-3})	mobility ($\text{cm}^2/\text{V-sec}$)
A) 230-II*	300	4.8×10^{14}	6,100
	77	4.5×10^{14}	46,500
B) 238-II†	300	3×10^{14}	6,800
	77	3×10^{14}	64,000
C) 278-I‡	300	5.4×10^{14}	6,450
	77	5.0×10^{14}	62,500

* Frontier Chemical.

† Air Products and Chemicals.

‡ Pittsburgh Materials and Chemicals Corp.

The purity of the AsH_3 gas has also been investigated, and it has been found that the lower the impurity content in the AsH_3 , the lower the impurity content in the GaAs. Beyond a point, however, the purity of the AsH_3 can only be inferred from electrical measurements of the GaAs, because of the lower limit of detectability by standard gas-analysis methods.

To further purify the AsH_3 and thereby obtain higher purity GaAs, the AsH_3 was allowed to react with the liquid Ga sources, which are known to be efficient getters of impurities. Reaction of the AsH_3 with the liquid Ga forms a GaAs skin on the surface of the Ga. The GaAs is then transported downstream by means of gaseous HCl which usually passes over the Ga. Normally, the AsH_3 enters the reaction tube downstream from the Ga boat and thus does not react with the Ga. The results of eight runs are shown in Table II. The room-temperature mobility of run 240-I is seen to be higher than those shown in Table I and the value of 8775 $\text{cm}^2/\text{V-sec}$ represents the highest value we have obtained to date. The mobility at 77°K is similar to the values shown in Table I, however. Unfortunately the growth rate is low and erratic,

Table II—Characteristics of GaAs Prepared by Reacting AsH₃ with Ga to Form GaAs on the Surface of the Ga Reservoir.

Run	T (°K)	n (cm ⁻³)	mobility (cm ² /V-sec)	Growth Rate micron/hour
233-I	Sample too thin for Hall measurement			14
235-I	Sample too thin for Hall measurement			9
240-I	300	1.7 × 10 ¹⁴	8,775	19
	77	1.4 × 10 ¹⁴	62,000	
240-I	300	2 × 10 ¹⁴	7,850	19
(duplicate)	77		65,700	
243-I	Sample too thin for Hall measurement			14
248-I	Sample too thin for Hall Measurement			11
250-I	300	1 × 10 ¹⁵	6,300	
	77		56,000	
253-I	300	7 × 10 ¹⁴	5,775	14
	77		48,000	

and this, in combination with the erratic electrical properties, makes this technique unsuitable for the preparation of TEO devices, which require accurately controlled carrier concentrations and thicknesses.

The purity of vapor-grown GaAs can also be influenced by the As/Ga ratio present in the gaseous ambient during growth.⁷ Table III shows that a reduction from the high As/Ga ratio normally employed can lead to mobility values as high as 7900 cm²/V-sec at 300°K and 82,000 cm²/V-sec at 77°K, and also to higher net carrier concentrations ($N_D - N_A$). This suggests that the higher net carrier concentration is

Table III—Characteristics of GaAs Prepared with Various As/Ga Ratios.

Run	T (°K)	n (cm ⁻³)	mobility (cm ² /V-sec)	As/Ga ratio*
238-II	300	3 × 10 ¹⁴	6,800	3.5/1
	77	3 × 10 ¹⁴	64,000	
288-II	300	2.7 × 10 ¹⁴	5,500	3.5/1
	77	2.6 × 10 ¹⁴	55,000	
307-II	300	8.8 × 10 ¹⁴	7,350	0.7/1
	77	8.0 × 10 ¹⁴	64,500	
	300	6.5 × 10 ¹⁴	5,325	
	77	5.7 × 10 ¹⁴	58,250	
309-II	300	8.3 × 10 ¹⁴	7,925	0.2/1
	77	7.2 × 10 ¹⁴	82,000	
	300	1 × 10 ¹⁵	6,900	
	77	9 × 10 ¹⁴	72,500	

* As/Ga ratio is calculated from the ratio of the flow rate of AsH₃ to the flow rate of HCl.

achieved by a decrease in N_A , rather than an increase in N_D , and indicates that these samples have a lower degree of compensation.

In addition, point-contact, reverse-bias measurements on 3° angle-lapped wafers indicate that the lower-than-normal As/Ga ratio samples may have a more homogeneous carrier concentration because of the lower degree of compensation. Both Si- and Te-doped substrates have been used at the low As/Ga ratios, and no evidence for significant autodoping of the n-layer by the Te from the substrate, as can occur in the AsCl_3 method,⁷ has been observed. Moderately good microwave properties have been obtained with this approach, but the low growth rate and the higher carrier concentrations limit the usefulness of using low As/Ga ratios.

Table IV—Characteristics of GaAs Prepared in a Synthetic Quartz Tube.

Run	T (°K)	n (cm^{-3})	mobility ($\text{cm}^2/\text{V}\cdot\text{sec}$)	Comment
258-I	300	1.3×10^{15}	6,100	First run in tube
	77	9.9×10^{14}	28,900	
260-I	300	2.4×10^{14}	6,000	Second run; tube HCl cleaned
	77		52,750	
262-I	300	1.9×10^{14}	4,150	Third run; tube HCl cleaned
	77		49,000	
262-I	300		3,820	One substrate
Duplicate	77		46,800	washed with EDTA

The type of reaction tube used for the growth of the GaAs also may affect the purity attained. To investigate this, high-purity synthetic quartz, and a carbon-coated natural quartz tube have been used, in addition to the usual natural quartz. It was thought that synthetic quartz with its low metallic impurity level, as compared to natural quartz, might lead to higher purity GaAs. As shown in Table IV, this does not occur and, in fact, even with the best run, 260-I, somewhat lower mobility values compared to natural quartz (see Table I) are observed. This may be caused by the higher water content of synthetic quartz.

To reduce silicon contamination, the growth of GaAs n layers in a carbon-coated quartz tube (prepared by the pyrolysis of high-purity acetone vapor), along with a vitreous carbon boat to contain the Ga, was examined and the results shown in Table V. It may be seen that the results obtained are similar to the values for natural quartz, except for the value of $7725 \text{ cm}^2/\text{V}\cdot\text{sec}$ in run 289-I. This is somewhat higher than the other values but it is not reproducible. It may be seen further

that HCl vapor cleaning and aqua-regia liquid cleaning of the tube are equally effective in obtaining high-purity layers.

The nature of the nn^+ interface is also important in device operation, and capacitance-versus-voltage measurements on Schottky barrier diodes have been made to derive the carrier concentration profile at these interfaces for several conditions of growth sequence. This $n+n$ layer interface should be free from spurious high-resistance layers, which lower efficiency and cause premature breakdown. The exact nature of the interface for optimum device performance is not yet known, and therefore, we have investigated two different growth pro-

Table V—Characteristics of GaAs Prepared in a Carbon-Coated Tube.

Run	T (°K)	n (cm^{-3})	mobility ($\text{cm}^2/\text{V}\cdot\text{sec}$)	Comment
286-I	300	1.4×10^{14}	5,200	Carbon-coated tube #1
	77	1.3×10^{14}	42,000	
289-I	300	5×10^{14}	7,725	Carbon-coated tube #2
	77	4.4×10^{14}	68,000	
297-I	300	6×10^{14}	6,450	Carbon-coated tube #2; HCl vapor cleaned
	77	5.2×10^{14}	70,000	
302-I	300	7×10^{13}	6,200	Carbon-coated tube #2; Aqua regia liquid cleaned
	77	7.3×10^{13}	70,250	

cedures to determine their effect on the carrier-concentration profile and on the device performance. This involved the growth of 15-micron-thick n layers for Schottky barrier measurements and 100-micron-thick n layers for oscillator diodes. In method A, the n layers were deposited directly on the n^+ substrate (Device run 230-I); in method B, an initial vapor-grown n^+ layer was deposited on the n^+ substrate, followed by a vapor-grown n layer (run 220-I). The carrier-concentration profiles for these two methods are shown in Figs. 2 and 3, respectively. The detailed measurements show that method A leads to the lowest average carrier levels in the n layer, presumably because no residual Se dopant remained in the gas stream from the prior n^+ -layer growth as it can in method B. These results corroborate those found earlier for 10-GHz oscillators, which showed that devices prepared according to method A have a higher resistivity than those prepared by method B.⁴ Method A has been used to prepare most of the L-band oscillators for this program. The importance of the substrate interaction with the n layer can

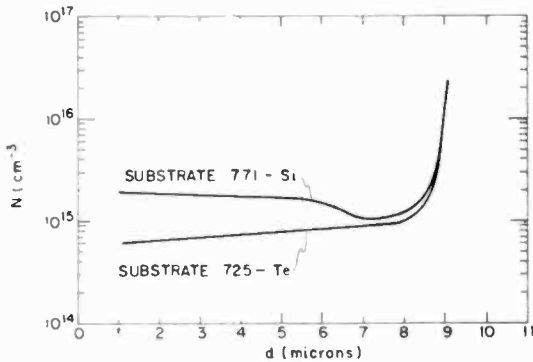


Fig. 2—Carrier concentration (N) as a function of depth (d) for n layer deposited directly on Te and Si-doped substrate during simultaneous growth (Run 316).

be seen in Fig. 2, where curves for the Si-doped and the Te-doped substrates are shown. In the case of the Si-doped sample, a high-resistance layer is formed at the n^+n interface, in agreement with results found by others.⁸ Fig. 3 shows that this high-resistance layer can be eliminated by the growth of an initial n^+ layer that serves as a barrier to diffusion of acceptor impurities from the substrate. The use of this method can thus lessen the dependence on the quality of the substrate. The carrier concentration in the vapor-grown layers is seen to change from the 10^{15} to 10^{18} cm^{-3} range within a distance of 1 to 3 microns for both methods, which indicates that we have been

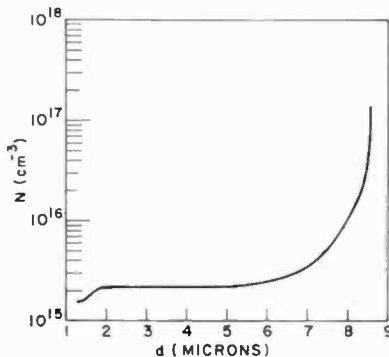


Fig. 3—Carrier concentration (N) as a function of depth (d) for a vapor grown n^+ layer followed immediately by a vapor grown n layer. Profile is the same for deposition on Te-doped (725) and Si-doped (771) substrate during simultaneous growth (Run 322).

successful in achieving rather abrupt transitions. As expected, this transition region is somewhat smaller for method A than for method B. It will be shown that good devices can be fabricated from wafers grown by both methods (see Fig. 9, runs 230 and 220).

Generally the top n^+ contact is made in just the reverse manner, in that the H_2Se dopant is turned on after the growth of the n layer. To examine this vapor-grown nn^+ interface, a thick n layer was first grown onto a p^+ substrate, followed by the customary vapor-grown n^+ layer. The substrate has to be removed so that Schottky-barrier gold diodes can be deposited on the first-grown n layer surface in order to study the top (last-grown) nn^+ interface of the oscillator structure. To accomplish this, a p^+ substrate instead of an n^+ substrate is used in conjunction with an electrochemical etch that removes p^+ material until the p - n junction is reached, i.e., the first-grown n layer surface. The carrier profile for the top nn^+ interface is shown in Fig. 4. Comparison with Fig. 3 (method B) shows the grading at both the top and the bottom nn^+ interfaces to be similar.

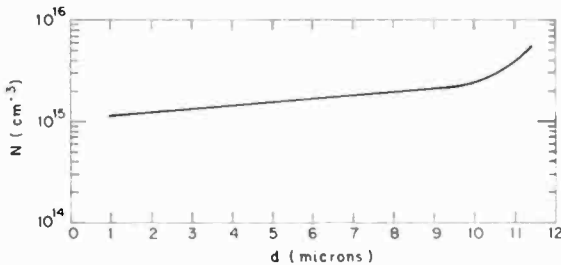


Fig. 4—Carrier concentration (N) as a function of depth (d) for top-vapor-grown nn^+ interface (Run 353).

Although the Hall-effect measurements and the capacitance-voltage measurements give a picture of the quality of our material and the effect of process variables on the carrier concentration, carrier profile, and mobility, they can not indicate *a priori* which wafers will yield high-power devices. The best test of the material devised to date is the microwave evaluation of completed devices. This indicates that subtle differences that do not show up in the other measurements are responsible for variations in device performance. The main effort has focused therefore on the preparation of n^+nn^+ wafers, under a wide variety of experimental growth conditions, and testing of these samples as devices. The results to date suggest that wafers yielding high-

efficiency devices can be grown only when good AsH_3 , good HCl , good substrates, and good growth conditions are used simultaneously. In this way we were able to achieve devices with efficiencies greater than 15% in seven out of 10 growth runs.

Device Fabrication Technology

To produce high-power transferred-electron devices capable of operating at high duty cycles, it is necessary to mount large chips of GaAs on good heat sinks. This process must be reproducible, have good yield, and provide a low thermal resistance from device to heat sink. The device fabrication technology developed satisfies these requirements and provides for the fabrication of multichip oscillators for high-power, high-ambient-temperature operation.

The multichip approach has several distinct advantages over the use of one large-area device. The most important of these advantages is yield. If enough extra chips are incorporated in a package to allow for failures, the final packaged device yield can be 100%. Second, the multichip approach offers heat-sink advantages by spreading the thermal dissipation over a larger area. This feature is extremely important in high power applications.

In device fabrication, the n^+ substrate is first lapped to the desired thickness. Silver is then deposited on the top n^+ epitaxial layer and the wafer is wire sawed into chips of the desired size. The chips are cleaned and then alloyed into a specially prepared V5000 varactor package. Gold straps are thermo-compression bonded onto the devices and the package flange. Fig. 5 illustrates a four-chip TEO at this stage in the process. Finally, the device is carefully cleaned and the surface is passivated.

RF Circuit Studies

A compact cavity has been developed for the efficient operation of high-power devices. The main objective was to obtain a compact L-band cavity that would optimally match the TEO devices into a 50-ohm load. Since the dc-rf conversion efficiency depends to a large extent on the harmonic as well as the fundamental loading for TEO's, as for all nonlinear devices, the design also provided independent tuning at the second harmonic. This makes possible tuning for optimum current and voltage waveforms and, thus, gives high efficiency.

The cavity consists of a re-entrant coaxial cavity. The device is mounted at the end of the shorted line of the cavity, as shown in Fig. 6.

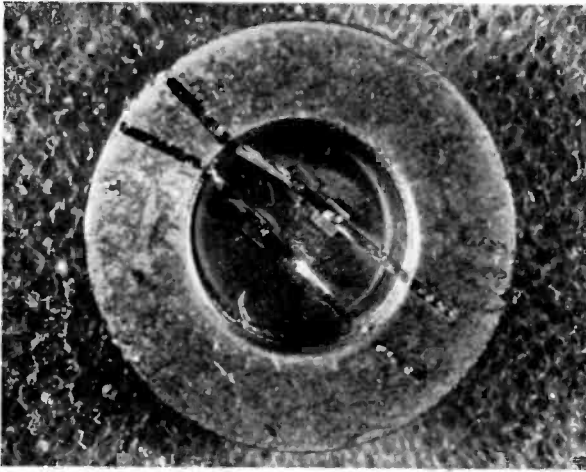


Fig. 5—Photograph of multichip TEO.

The output is loop coupled. A high- Q variable capacitor and tuning screw in the output circuit provide the necessary tuning to match the device directly into a 50-ohm load.

The design criterion employed involves resonating the device capacitance with the inductance of the shorted coaxial line of the cavity at the desired operating frequency. This is accomplished for a range of devices through the use of a replaceable inner conductor in the cavity. By simply changing the dimension of this inner conductor, the cavity can be made to resonate at the desired frequency for a range of device impedances. The output circuit is then tuned to optimize the coupling to the 50-ohm load to obtain maximum power output. Devices with fundamental impedances ranging from $50 + j65$ (20 watts) to $10 + j28$ (110 watts) have been successfully operated in this circuit.

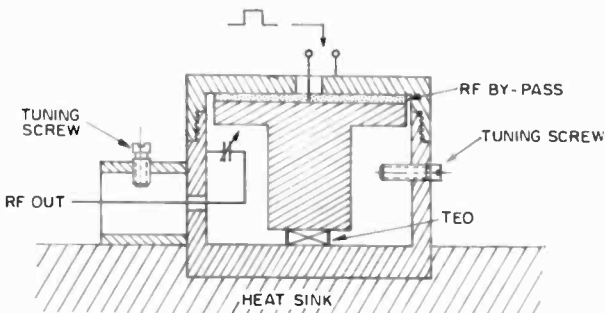


Fig. 6—Schematic of cavity design.

The additional tuning screw incorporated in the cavity design provides fine frequency adjustment once the basic geometry is set. The tuning screw also provides tuning at the second harmonic, which, as stated previously, makes it possible to optimize the current and voltage waveforms for maximum efficiency.

When the device is tuned for maximum power output, impedance measurements have shown that the loading at the second harmonic is purely inductive. For a 70-watt device operating at 10.3% efficiency, the fundamental impedance presented by the cavity was $6.5 + j25$, while the second-harmonic impedance was $j75$. This second-harmonic impedance could be changed from $-j200$ to $+j90$ with the tuning screw without changing the fundamental impedance. The output power would vary by as much as 10 dB for this type of change.

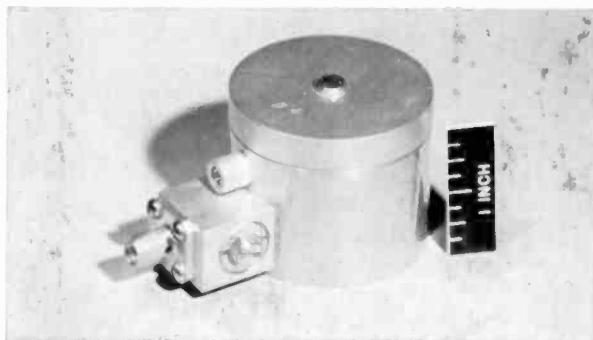


Fig. 7—Photograph of cavity design.

A photograph of a finished L-band cavity is shown in Fig. 7. The overall height is $1\frac{1}{4}$ inches and the diameter is $1\frac{1}{2}$ inches, with the additional side arm extending another $\frac{1}{2}$ inch.

Oscillator Characteristics and Performance

There are several device and operating parameters that are important in achieving high efficiency and, thus, high-power operation of TEO's. The main device parameter is the product of the sample doping density (n) and active layer length (L). This product will affect both the domain growth dynamics and maximum domain size which, in turn, affect the current waveform of the device. In Fig. 8 we have plotted the efficiency versus nL for a large sample of devices fabricated from several different wafers. As can be seen, the nL product for highest

various modes. As can be seen, the data clusters in a very definite part of the plane, the part where the delayed domain and hybrid modes of operation are possible. In particular, it appears that the high-efficiency devices from run 360 are operating in the delayed-domain mode. However, there is enough uncertainty in the boundaries, particularly when bias voltages are accounted for, that it is difficult to distinguish whether many of the devices are in the delayed-domain, transit-time, or hybrid mode.

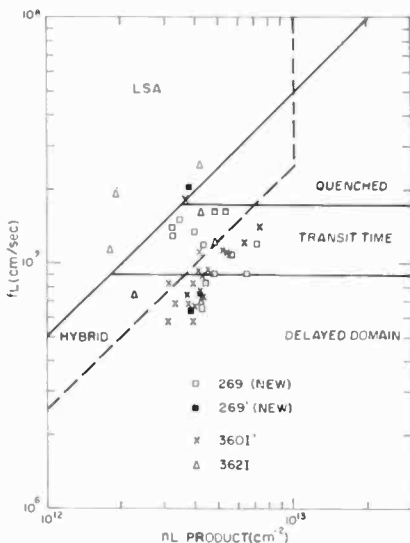


Fig. 10— jL product versus nL product (efficiencies over 10%).

As discussed in the previous section, high-power devices are made by paralleling many chips in one varactor package. This operation has been successful for paralleling as many as five chips at one time. These multichip oscillators are indistinguishable from single-chip oscillators in terms of rf performance. That the rf spectrum is as clean as that obtained from a single oscillator indicates that all oscillators are locked together. The power spectrum obtained from these devices usually follows the $\sin^2 X/X^2$ relationship expected for pulsed operation. Normal operation is with 0.5-microsecond-wide pulses at duty cycles up to 1%. Considerably longer pulse lengths and higher duty cycles have been demonstrated, as well as operation in pulse bursts.

The yield of high-quality GaAs wafers has now reached the point where devices with power outputs of 100 watts are readily fabricated.⁹

The dc-to-rf conversion efficiencies of these devices generally range from 10 to 15%. A more recent wafer had a 50% yield of devices with efficiencies between 15% and 20%. Three devices fabricated from this wafer had efficiencies in excess of 30%, the highest being 32.2% for a single chip device that produced 117 watts at 1090 MHz.¹⁰ This value represents, to the best of our knowledge, the highest efficiency reported for any TEO. These results indicate that, as material properties improve, efficiencies of the order of 30% will be regularly possible.

Table VI—Results Obtained for Single- and Multichip Oscillators in L- and S-Band.

Number of Chips in Device	Power (watts)	Frequency (GHz)	Efficiency (%)
1	117	1.09	32.2
1	160	1.06	30.9
1	120	1.00	30.0
1	200	3.05	29
1	55	1.50	27.7
3	220	1.09	23.2
4	180	1.00	25
3	120	1.10	20.6
2	120	1.10	20
2	100	3.1	27

Table VI gives a summary of some results for both single and multichip oscillators in L- and S-band. The highest power obtained thus far is 220 watts with 23.2% from a device with three chips in parallel. Although the work on S-band TEO's has been far less extensive than that on L-band devices, output powers as high as 200 watts and an efficiency of 29% have been achieved. The results in this table indicated that high-power devices are readily fabricated by simply paralleling smaller chips.

Stability and Life Tests

In many practical microwave applications, the question of environmental stability is an important one. Our epitaxial GaAs is particularly suited to operation over a wide temperature range because it possesses a positive temperature coefficient of resistance. Thus, devices fabricated from this material are not subject to thermal runaway, as they merely

turn off if the ambient temperature or internal heating becomes too high. Pulsed devices have been operated at ambient temperatures as high as $+180^{\circ}\text{C}$ and as low as -200°C (i.e., immersed in liquid nitrogen). The electron mobility increases and the threshold voltage decreases with decreasing temperature. The operating efficiency is therefore higher at liquid-nitrogen temperature than at room temperature.

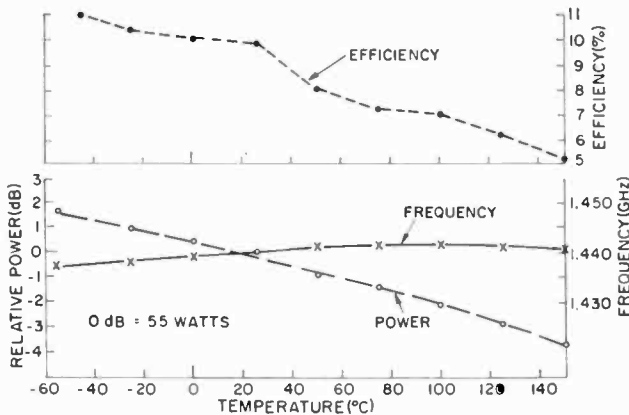


Fig. 11—Temperature characteristics of multichip TEO.

Fig. 11 shows the operating characteristics of a multichip TEO over the ambient temperature range from -55°C to $+150^{\circ}\text{C}$. The device was mounted in a V7000 varactor package and tuned in a re-entrant cavity. The power output was 50 watts at 1.440 GHz with 9.8% efficiency. The over-all power change was 5.5 dB (+1.5 to -4 dB), the frequency shift was less than 5 MHz (-3 MHz to $+1.5$ MHz), and the efficiency varied from 11 to 5.2%.

To determine the effect of internal heating, duty-cycle tests were again run on a 55-watt TEO. The device used was permanently mounted by direct alloying to a V5000 varactor package. The larger package and direct alloying provide a good heat sink for the device. The results of the test are shown in Fig. 12. The power drops by only 1.6 dB over a duty-cycle range from 0.01% to 1% and the frequency changes by only 2.5 MHz. The change in power is accompanied by a drop in efficiency from 18.3% to 13.4%. Even better results should be possible as further improvements are made in heat-sink technology.

Preliminary life tests have shown no evidence of either rapid or

slow degradation. Several pulsed L-band devices have been operated for 5000 hours with stable output and a cw X-band device has been operated for over 13,000 hours with stable output.*

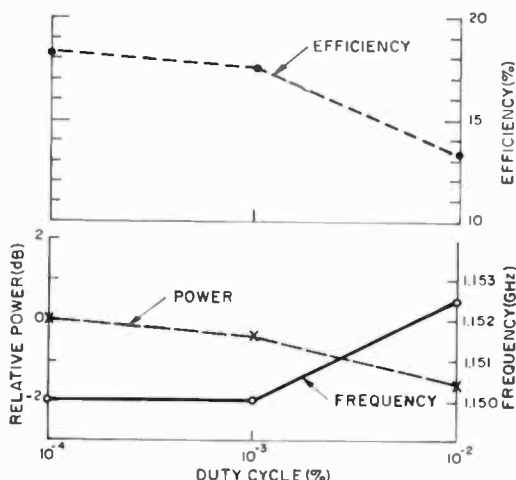


Fig. 12—Duty cycle characteristics of multichip TEO.

Conclusion

To date, peak-power levels up to 220 watts and efficiencies up to 32% have been successfully achieved from GaAs transferred-electron oscillators. These results have been achieved through a series of material and device technology improvements. The devices have also demonstrated long life plus stable operation over a wide range of temperature and duty cycle. These characteristics have proven that TEO's are already highly useful devices. The performance levels described in this paper are already more than adequate to replace tubes in IFF transponder systems, phased-array radar systems, and military and commercial communication systems in general. In addition, they have made possible new, lightweight, portable versions of such systems. As new performance levels are reached, these devices will become applicable in many other high-power microwave systems.

* S. Y. Narayon, private communication.

Acknowledgments

The authors would like to thank J. Appert for assistance in preparing the epitaxial material, P. Gwozdz for assistance in the $C-V$ measurements, and S. Dolochycki, V. Lawson, and E. C. McDermott for assistance in the preparation and testing of devices. Finally, they would like to thank F. Sterzer for many helpful and stimulating discussions.

References

- ¹ D. G. Dow, C. H. Mosher, and A. B. Vane, "High-Peak-Power Gallium Arsenide Oscillators," **IEEE Trans. Electron Devices**, Vol. ED—13, p. 105, Jan. 1966.
- ² S. Y. Narayan and B. E. Berson, "High Peak Power Epitaxial GaAs Oscillators," **IEEE Trans. Electron Devices**, Vol. ED—14, p. 610, Sept. 1967.
- ³ F. Sterzer, "Microwave Solid-State Power Sources," **Microwave Jour.**, Vol. II, p. 67, Feb. 1968.
- ⁴ R. E. Enstrom and C. C. Peterson, "Vapor Phase Growth and Properties of GaAs Gunn Devices," **Trans. Metall. Soc. AIME**, Vol. 239, p. 413, March 1967.
- ⁵ J. J. Tietjen and J. A. Amick, "The Preparation and Properties of Vapor-Deposited Epitaxial $\text{GaAs}_{1-x}\text{P}_x$ Using Arsine and Phosphine," **Jour. Electrochem. Soc.**, Vol. 113, p. 724, July 1966.
- ⁶ J. A. Copeland, "Theoretical Study of a Gunn Diode in a Resonant Circuit," **IEEE Trans. Electron Devices**, Vol. ED—14, p. 55, Feb. 1967.
- ⁷ D. W. Shaw, R. W. Conrad, E. W. Mehal, and O. W. Wilson, "Gallium Arsenide Epitaxial Technology," **Gallium Arsenide**, The Inst. Physics and the Phys. Soc., London, p. 10, 1967.
- ⁸ C. M. Wolfe, A. G. Foyt, and W. T. Lindley, "Epitaxial Gallium Arsenide for High-Efficiency Gunn Oscillators," **Electrochem. Tech.**, Vol. 6, p. 208, May-June 1968.
- ⁹ B. E. Berson, R. E. Enstrom, and J. F. Reynolds, "100 Watt L-Band Transferred Electron Oscillators for Transponder Applications," **NEREM Record**, Vol. 10, p. 94, 1968.
- ¹⁰ J. F. Reynolds, B. E. Berson, and R. E. Enstrom, "High Efficiency Operation of Transferred Electron Oscillators." **Proc. IEEE**, Vol. 57, p. 1692, 1969.

Sonic Film Memory* †

R. Shahbender, P. Herkart, K. Karstad, H. Kurlansik,
and L. Onyshkevych

RCA Laboratories, Princeton, N. J.

Abstract—The sonic film memory utilizes propagating strain pulses and thin uniaxial magnetic films to realize an all-electronic block-oriented random-access memory with microsecond latency time and megabit transfer rates. Such a memory could be used as a peripheral store in data processing equipment similar to the presently used digital-drum systems. Factors affecting the selection of geometrical parameters to optimize memory-device performance are discussed for devices using either shear or longitudinal strain. Experimental data are presented showing increase in strain sensitivity of films doped with manganese. These films are usually inverted. The performance of ceramic and thin-film piezoelectric transducers is discussed, and data are presented showing ceramic transducer performance compatible with 100 bpi operation. Experimental device performance data at densities in the range of 25 to 100 bpi is presented.

Memory Description

The sonic film memory¹ is an all-electronic, block-oriented, random-access, nonvolatile memory. Information is stored in blocks, and random-access to the blocks is accomplished at electronic speed. From an overall point of view, this memory is similar to a digital magnetic drum utilizing one head per track, having a latency time of approximately 1 microsecond, and using no mechanical moving parts.

A memory block consists of a fused silica substrate with deposited uniaxial magnetic films in the form of continuous strips. Associated with each strip is an overlaying conductor that is used for both digitizing and sensing. An ultrasonic transducer and an ultrasonic

* The work described in this paper was partially supported by the United States Army Electronics Command, Fort Monmouth, New Jersey under Contract Number DAAB07-68-C-0030.

† This paper was presented at the 1969 Intermag Conf., Amsterdam, Holland.

absorbing termination are attached to the ends of the substrate, as shown schematically in Fig. 1. To enter information serially into a block, a strain pulse is launched along the substrate. Pulses of current (digit field) applied to the overlaying conductors cause reversal of the magnetization only in the strained regions of the magnetic film strips. Nondestructive serial retrieval of the stored information is effected by propagating the strain pulse in the substrate. This induces sense-signal voltages in the overlaying conductors.

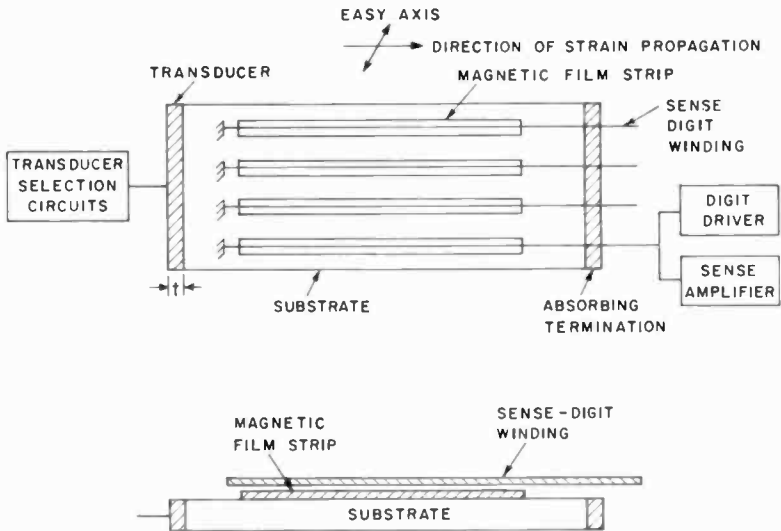


Fig. 1—Sonic-film memory block.

Writing requires the coincidence of the strain pulse and the digit field pulse at a bit location. The strain pulse produces both a rotation of the magnetization and a reduction in effective anisotropy field, and is equivalent to the word field in a conventional random-access thin-film memory. Non-destructive read-out (NDRO) sense signals are obtained because the magnetization is rotated reversibly by the strain pulse.

To realize a mass memory, a number of blocks are assembled into a stack and connected to drive and sense electronics. The access time to the leading bits of a block (essentially given by the time it takes to electronically select and energize a transducer) is expected to be 1 microsecond or less. The bit transfer rate is the product of the bit density and the velocity of sound in the substrate.

For device operation, two types of ultrasonic pulses may be used:

longitudinal pulses with a velocity of 5760 m/sec or shear pulses with a velocity of 3760 m/sec. For longitudinal pulses, the particle motion is in the direction of pulse propagation, and subjects the magnetic films to tension and compression. For shear pulses, the particle motion is orthogonal to the direction of pulse propagation and parallel to the film plane. This mode subjects the films to shearing stresses that are equivalent to tension-compression stresses inclined at 45° to the direction of pulse propagation.

The memory structure shown in Fig. 1 represents the simplest and most attractive realization for a memory block. Alternatively, discrete magnetic film spots arranged in rows on a substrate with separate digit-sense windings may be utilized. Such an arrangement requires precise clocking of the digit pulses to coincide with the arrival of the strain pulse at each discrete location. The velocity of sound in fused silica varies by 75 ppm/ $^\circ\text{C}$. Thus, the clocking must track temperature variations for writing. This difficulty is not present with continuous-film strips.

The most important parameter influencing the technical and economic performance of the memory is the bit density that may be realized. For densities under 200 bits per inch (bpi), the wave shape of the ultrasonic strain pulse launched into the substrate is a limiting factor. For densities greater than 200 bpi, magnetostatic interactions between adjacent bits as well as the wave shape of the strain pulse play an important role. For densities under 200 bpi, two classes of devices may be constructed, depending on the technique used for generating the strain pulses. In the first class are devices using ceramic transducers such as PZT for generating strain pulses. These transducers are readily available with resonance frequencies up to 5 MHz and have been further developed, as described in this paper, to yield resonance frequencies up to 20 MHz. Corresponding to these resonance frequencies are bit densities in the range of 25 to 100 bpi. In the second class, are devices utilizing evaporated layer transducers such as cadmium sulfide with resonance frequencies in the range of 50 to 100 MHz, and corresponding densities in the range of 100 to 200 bpi.

The usable substrate length is determined by the attenuation of ultrasonic pulses in fused silica. This, in turn, is determined by the highest frequency components of the strain pulse, and is on the order of 10 inches for densities of 200 bpi, and 20 inches for densities of 100 bpi. The width of the substrate influences the impedance presented by the transducer to the electronic drive circuitry. As the transducer area increases, its effective impedance decreases and the required peak pulse

power increases. For PZT transducers a width of 2 inches is acceptable in terms of impedance levels. The thickness of the substrate influences the propagation characteristics of the strain pulses as discussed later. It also affects the impedance of the digit windings (strip lines). Thicknesses in the range of 20 to 40 mils represent an optimum trade-off for the various important parameters.

Mathematical Analysis of Element Operation²

Analytical expressions have been derived in the literature³ for the magnetization rotation and change in the anisotropy field of uniaxial films as functions of strain. These expressions may be used to determine the dependence of the digit field, strain amplitude, and NDRO sense-signal amplitude on the relative orientation of the easy axis of the magnetic films with respect to the direction of propagation of strain pulses, and for operation with either shear or longitudinal modes.

The pertinent expressions to be used in the mathematical analysis of element operation are

$$\tan 2\theta_r = K \frac{\sin 2\phi}{1 + K \cos 2\phi},$$

$$h_k = H_k/H_k^o = (1 + K^2 + 2K \cos 2\phi)^{1/2},$$

$$K = \frac{3 \lambda \sigma}{2 K_u} = \frac{\sin 2\theta_r}{\sin 2(\phi - \theta_r)},$$

where ϕ = angle between the strain axis and the unstrained easy axis,

θ_r = the angle through which the strain rotates the easy axis (referred to the unstrained easy axis),

H_k^o = the strain-free anisotropy field,

H_k = the effective anisotropy field in the strained film,

h_k = normalized anisotropy field,

λ = magnetostriction constant,

σ = stress,

K_u = uniaxial anisotropy constant.

Since the dimensionless parameter K occurs frequently, stress is normalized to the value $\sigma_0 = (2/3)(K_u/\lambda)$ so that $K = \sigma/\sigma_0$. The stress σ_0 can be used as a figure of merit for memory device operation; the

lower this value, the more sensitive the film. Similarly, sense-signal amplitudes are normalized by dividing by $2M$ the maximum possible change in flux linkage.

Figure 2a shows the geometrical relations involved in the analysis of memory-element operation with shear-mode strain. The easy axis of the magnetic film element is assumed oriented at an angle θ with respect to the direction of propagation of a strain pulse. The particle motion in the strain pulse is at right angles to the direction

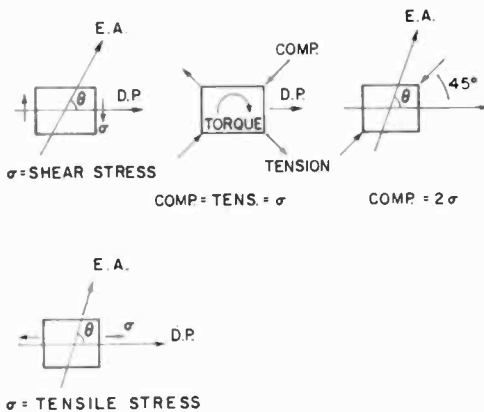


Fig. 2—Geometrical relations (a) for shear stress, and (b) for longitudinal stress.

of propagation, subjecting a small element of area to shearing stresses of amplitude σ as indicated in the figure. The shear stress may be replaced by tensile and compressive stresses, oriented at 45° to the direction of propagation, and a torque that rotates the element of area. The amplitude of the tensile (or compressive stress) is numerically equal to σ , the assumed shear stress. From the form of the expressions given above, the tensile component of stress may be combined with the compressive component of stress as far as the effect on the magnetism of uniaxial films is concerned. Thus, we assume that the element of area is subjected to a compressive stress of 2σ oriented at 45° to the direction of propagation. The effect of the torque is to rotate the element of area by a small amount. This rotation (of the order of 1 milliradian) has very small influence on the magnitude of digit field required or on the sense-signal amplitude and may, therefore, be neglected in the analysis of element operation.

Computationally, we assume a value of θ and a value of stress amplitude. The changes in anisotropy field and magnetization direction are computed from the equations given above. The ratio R of digit field to switch a strained element to that required to switch an unstrained element as functions of both θ and σ are next computed. Additionally, the change in flux linking the sense-digit winding is computed. The sense signal is proportional to the rate of change of this flux linkage; for a first-order approximation, the rotations are assumed to take place in equal times, so that the sense signal is taken as proportional to the change in flux linkage. Sense signals are normalized to the maximum possible change in linkage.

At each value of θ , the value of stress σ (or equivalently strain) that minimizes the quantity R is found. The minimum value R_M and the corresponding normalized values of stress and sense signal are shown plotted in Fig. 3a. The existence of a minimum value for R may be intuitively understood from the following argument. A small amount of strain rotates the magnetization and/or reduces the anisotropy (the size of the astroid) to result in a lower value of switching field; but a very large amount of strain "pins" the magnetization, making it more difficult to switch.

Inspection of Fig. 3a shows that for an easy axis angle of 45° , the value of R_M is zero for a normalized stress of 1. This corresponds physically to no rotation of M with linear reduction of H_k to zero. Unfortunately, such an orientation cannot be used in the memory device, because the sense signals are small due to lack of rotation for a given amount of strain. The discontinuity in sense output at 45° occurs because for easy-axis angles less than 45° , M rotates clockwise; for angles greater than 45° , M rotates counterclockwise. From the figure, it is seen that angles in the vicinity of 60° or 30° represent points at which reasonable trade-offs among R_M , signal amplitude, and required strain amplitudes may be made. For these computed results, neither shape anisotropy nor magnetostatic interactions between adjacent film elements are considered. For memory devices employing continuous-film strips, it is expected that shape-anisotropy effects will be more marked as the easy-axis angle becomes shallower with respect to the long dimension of a film strip. Thus, it is expected that easy-axis angles around 60° represent an optimum choice for device operation.

The computations from which the data of Fig. 3a are extracted give the values of R and sense signal as functions of θ and stress amplitude. By inspecting the computed results at angles θ in the vicinity of 60° , we can determine the effect of tolerances on memory

device operation.² If, for example, we allow a tolerance of $\pm 15\%$ in the parameter K and choose an operating point at which $R = 0.8$ and the required normalized stress is 0.7, then an easy-axis orientation within the range $50\text{--}60^\circ$ (nominally 55°) will permit coincident writing to be accomplished while the sense-signal amplitude varies, at most, by $\pm 40\%$. The $\pm 15\%$ tolerance on K implies parameter changes in λ , σ , and K_u with a cumulative effect of $\pm 15\%$. The chosen operating point requires a digit field of $0.4H_K$.

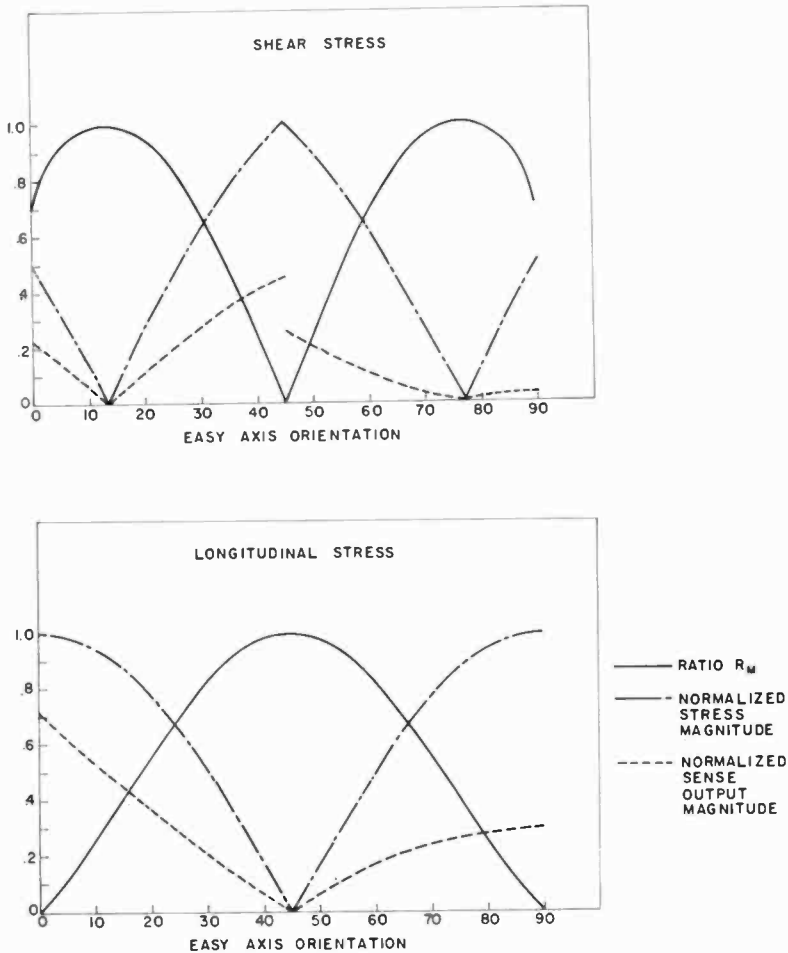


Fig. 3—Operating parameters (a) for shear stress, and (b) for longitudinal stress.

Fig. 3b represents the results of similar computations for operation with longitudinal strain pulse (Fig. 2b shows the geometrical relations). For this case, the particle motion is in the direction of pulse propagation subjecting the film element to either tensile or compressive stresses. For easy-axis orientations between 0 and 45°, and for positive magnetostriction films, the required stress is compressive; for angles between 45° and 90°, the required stress is tensile. At 45°, the best ratio R obtainable is 1. Since any amount of strain will raise the switching threshold, the optimum amount of strain is zero, with zero sense output. Shape-anisotropy considerations again imply that an easy-axis orientation of around 75° is optimum for operation with longitudinal mode strain. If a $\pm 15\%$ tolerance is allowed on the parameter K , the easy axis may be within the range of 70 to 80° to permit operation of the memory element. The sense-signal amplitude varies at most by $\pm 30\%$.

Magnetic Films

The amplitude of strain pulse required for memory operation is inversely proportional to the strain sensitivity σ_0 of the magnetic films. Increasing the strain sensitivity of the films reduces the difficulties associated with generation of the required strain pulses. Otherwise, the films should have square easy-axis hysteresis loops, good orientation, low dispersion, long-term stability, and reasonably low values of H_c and H_k to maintain low digit power.

For a fixed geometry device, i.e., where the width of a film strip and overlaying conductor are fixed, the digit power is proportional to H_k . Reducing H_k reduces the drive-current amplitude. On the other hand, the minimum film width that may be used, as well as the realizable bit density, depends on the value of H_k . Thus, a trade-off must be made between track density, bit density, and digit power.

To reduce the effects of digit disturbs on element operation, it is desirable to have H_c comparable in value to H_k . Under these conditions, element switching should occur by rotation rather than wall motion.

Empirical materials work revealed two types of alloys suited for this application: Ni-Fe-Co alloys and Ni-Fe-Mn alloys. Both are prepared by vacuum evaporation in an orienting magnetic field of 50 Oe onto substrates heated to 300°C. The cobalt films are evaporated from melts containing ~60% Ni, 25% Fe, 15% Co, while the manganese films are fabricated from melts containing ~58% Ni, 37% Fe, 5% Mn. The film composition differs slightly from the melt composition. Evapo-

ration is accomplished by induction heating of the melt in an alumina crucible with the substrates located 30 inches from the source. Patterns are obtained by masking. The evaporation rate is from 1 to 20 Å per second. Both types of films exhibit single-phase (face-centered cubic) crystal structure and have shown no changes in their characteristics for periods up to a year in room ambient.

Of the two compositions, the Mn films are the more strain-sensitive. Figs. 4 and 5 show a comparison of the strain-dependent characteristics of typical Co and typical Mn films as well as those of an NiFe film having the approximate composition of 60:40. Fig. 4 shows rotation of the easy axis as a function of applied static strain and Fig. 5 shows the corresponding changes of anisotropy field H_k .

The data presented in Figs. 4 and 5 are obtained by measuring the magnetic parameters of film samples subjected to static strains in an hysteresis loop tester described previously.¹ The tester permits the application of a uniaxial static stress at any predetermined angle with respect to the easy axis of a film sample, while at the same time measuring the hysteresis loop in an arbitrary direction. Thus, hard-axis or easy-axis loops of stressed films may be measured.

The data in Figs. 4 and 5 may be used to compute the magnetostriction constant λ and the operational figure of merit σ_0 . The value of λ is

$$\lambda = \frac{MH_k \sin 2\theta_r}{3\sigma \sin 2(\phi - \theta_r)}$$

For the three film compositions, we assume that

$$4\pi M = 10^4 \text{ gauss}$$

$$E = \frac{\text{Stress } \sigma}{\text{Strain } \epsilon} = \text{Young's Modulus} = 16 \times 10^{11} \text{ dynes/cm}^2.$$

The figure of merit σ_0 may also be expressed as an equivalent strain ϵ_0 . Table I lists the computed values of λ , σ_0 , and ϵ_0 .

The best Mn-Ni-Fe films have H_k and H_c values of approximately 2 to 4 Oe, with H_c normally greater than H_k . These films show rotational switching and seem to be well suited for use in the memory. The Co-Ni-Fe films have been described previously.⁴

The most important consideration in the fabrication of these highly strain-sensitive films is the question of pre-stresses. If the substrate

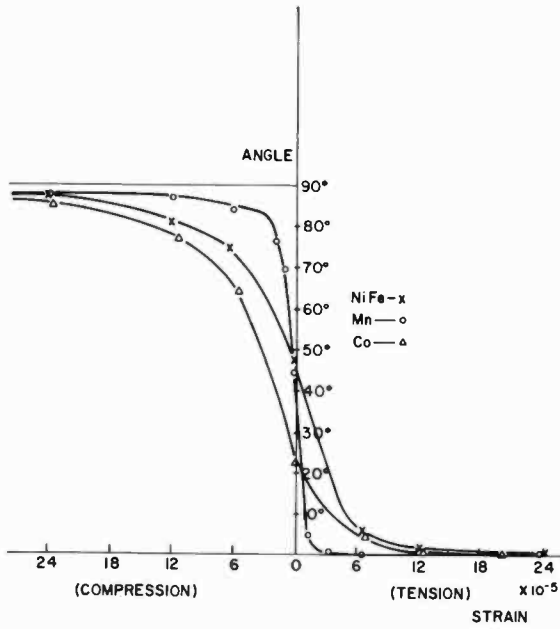


Fig. 4—Rotation of the easy axis versus static strain.

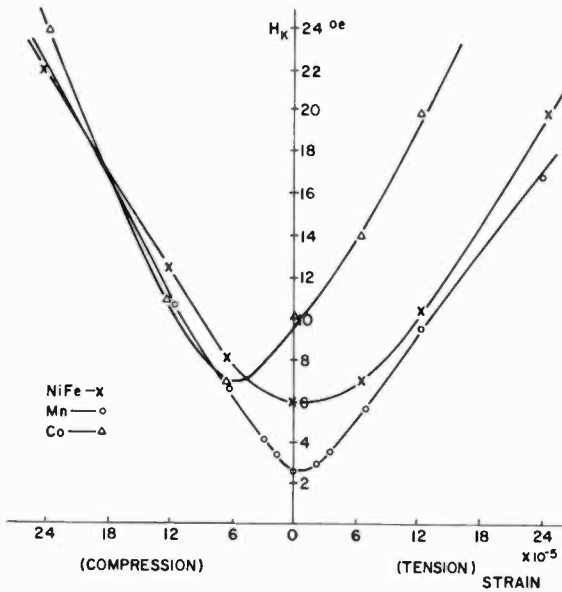


Fig. 5—Anisotropy field versus static strain.

temperature distribution during evaporation is not very tightly controlled (within 1%), thermally induced nonisotropic built-in strains will appear in the films. Such strains can easily reach 1×10^{-5} to 5×10^{-5} values and thus cause skew, dispersion, and other parameter deterioration. Uniformity and reproducibility will thus depend very heavily on the ability to heat the substrate uniformly.

Table I—Magnetostriction Properties of the Thin Films Shown in Figs. 4 and 5.

	Ni-Fe	Ni-Fe-Co	Ni-Fe-Mn
<i>Measured Values</i>			
H_k^0 (Oe)	6	10	2.5
ϕ (degrees)	48	22	45
θ_r (degrees)	23	12	30
Strain	3×10^{-5}	4×10^{-5}	1×10^{-5}
<i>Computed Values</i>			
λ	30×10^{-6}	48×10^{-6}	69×10^{-6}
σ_0 (dynes/cm ²)	51×10^6	54×10^6	9.2×10^6
ϵ_0	32×10^{-6}	33×10^{-6}	5.8×10^{-6}

Generation and Propagation of Ultrasonic Strain Pulses

The most practical method for generating strain pulses is by means of piezoelectric transducers. For narrow pulses, high-frequency broadband transducers are required; therefore we have examined thin transducers whose acoustic impedance is matched to the substrate for maximum damping.

A transducer bonded to a fused silica plate substrate, as shown schematically in Fig. 1, is equivalent to a network with pass bands around the fundamental and odd harmonics of the transducer resonance frequency. For a ceramic transducer, such as PZT, with a fundamental resonance frequency of 20 MHz, the third-harmonic resonance is at 60 MHz. The response of the transducer to excitation at this or higher frequencies is extremely low. The equivalent network is thus a band-pass filter with a center frequency at the transducer fundamental resonance.

Similarly, for a plate with a CdS transducer having a fundamental

resonance frequency of 100 MHz, the third-harmonic band pass is centered around 300 MHz. The attenuation in fused silica substrates is proportional to the square of the frequency, which, coupled with the drop in ultrasonic power output of a transducer operated at a harmonic of its resonance frequency (power output is proportional to $1/N^2$, where N is the order of the harmonic), shows that in this case, as with the PZT, we have a network with a single pass band centered around the transducer resonance frequency. The bandwidth, therefore, is determined by the transducer material and the characteristics of the bond, assuming that the load is always fused silica and has a relative value of the order of 1 for well-bonded transducers.

The network performance is most easily determined by monitoring the echo signal reflected from the far end of a plate. The resonance frequency of the transducer is inversely proportional to the thickness t shown in Fig. 1. For ceramic transducers, as t becomes very small, on the order of the dimension of several grains, the response of the transducer becomes dependent on the number of grains in a given area and the poling direction of the individual grains. For evaporated-layer CdS transducers, as t is increased, greater misalignment of the piezoelectric axis of the film is experienced, resulting in reduced output.

Table II—Memory Characteristics

Transducer Resonance Frequency (MHz)	Shear Strain					Longitudinal Strain		
	100	15	6	3	1.5	100	50	30
Linear Bit Density (bpi)	670	100	40	20	10	450	225	135
Bit Transfer Rate (Mbps)	100	15	6	3	1.5	100	50	30
Substrate Thickness Zero Order Mode (mils)	0.5	4	10	20	40	1	2	4

Table II gives the relationship between transducer resonance frequency and bit density for both longitudinal- and shear-strain operation. For a relative bandwidth of 1, the optimum strain-pulse duration is approximately $1/f_r$, where f_r is the transducer resonance frequency. The density at which regions of reversed magnetization may be created by coincident writing and a sense signal generated by the same strain pulse as used for writing, is f_r/v , where v is the relevant strain-pulse velocity. A signal is generated at each magnetization transition.

A coding system in which the magnetization of a region corresponds

to a bit yields a bit density equal to f_r/v and a bit rate of f_r . A system in which a single magnetization transition corresponds to a bit yields a double density and bit rate. The data given in Table I is for the former case.

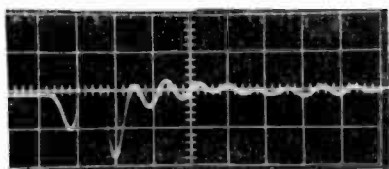
Mathematical expressions are derived in the literature⁹ for the propagation of shear waves in plate geometries. A shear pulse (with particle motion parallel to the major surface of the memory substrate, as shown in Fig. 1) can be decomposed into Fourier components. If the thickness of the substrate is chosen to be less than half the wavelength of the highest frequency component present, then the propagation of the shear pulse in the substrate is nondispersive. This critical thickness is given in Table II. For this condition, the zero-order mode is the only one that can propagate. All higher-order modes are below their cutoff frequencies. The zero-order mode, in the ideal case, propagates nondispersively. In a substrate with finite dimensions and with magnetic-film strips deposited on it, dispersive effects occur as a result of the minor surfaces of the substrate and the presence of the magnetic-film strips.

A similar situation holds for the propagation of longitudinal-mode pulses. The first-order longitudinal mode displays reasonably low dispersive propagation for a limited bandwidth. This bandwidth is below the cutoff frequency of the second longitudinal mode but does include some flexural modes. Beyond this bandwidth, the first-order longitudinal mode displays a linear delay characteristic that has been utilized in the construction of dispersive delay lines. Table II lists the substrate thicknesses needed for the longitudinal case. For high bit densities, the required substrate thickness for nondispersive propagation is too thin. Considerable deviation from this condition for shear type pulses is feasible as shown experimentally below.

Fig. 6 shows the echo response for a PZT ceramic transducer bonded to the end of a $3 \times 1 \times 0.04$ inch fused-silica slide. The transducer thickness is approximately 2 mils with a corresponding resonance frequency of 20 MHz. For a 40-mil thick slide, the first-order shear-mode cutoff frequency is 1.9 MHz, i.e., for frequencies below 1.9 MHz, the only mode that can propagate in the substrate is the zero-order mode, which is nondispersive. The transducer is excited with a trapezoidal input voltage pulse having a rise time and a fall time of 20 ns and a width at the base of 50 ns, from a 50-ohm source. By comparing the first round-trip echo with the second round-trip echo, the effect of dispersion for a 6-inch travel can be determined. For the tested device, the echoes are quite similar, showing that propagation is nondispersive

for all practical purposes. Inspection of the echo shown in Fig. 6 shows that it is reasonably symmetric with very little spurious noise.

For ceramics, a thickness of two mils represents a lower practical limit for strip transducers. Below this thickness, in addition to problems of lapping a porous material, the possibility of partial depoling is present, as well as the possibility of generating a dispersive shear mode in which particle motion is normal to the major surface of the slide (referred to as shear vertical in the literature). This shear mode is generated as a result of misorientation of the poling axis of individual grains in a thin transducer.



50 ns/cm

100 mv/cm

INPUT TO TRANSDUCER: 5 V PULSE

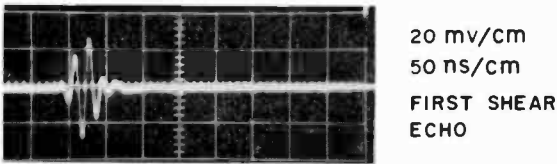
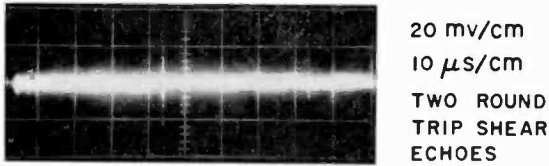
Fig. 6—Echo response of high-frequency ceramic transducer.

The transducer performance shown in Fig. 6 is adequate for 100 bpi density. For higher densities it is necessary to utilize evaporated layer transducers, such as CdS or zinc oxide.

Cadmium sulfide is nearly ideal for generating strain pulses in quartz slides because of its acoustic match to quartz. The transducers are made by vacuum deposition of high-resistivity, polycrystalline, oriented layers onto the metalized ends of the substrates. For longitudinal-strain transducers the piezoelectric axis is normal to the slide end, whereas for shear strain the piezoelectric axis is oriented at approximately 39° to the substrate normal⁶.

Fig. 7 shows the echo response from a shear-strain CdS transducer formed on the end of a $3 \times 1 \times 0.08$ inch fused-quartz substrate. Echoes from two complete round trips are shown. The piezoelectric axis orientation is optimum, giving no evidence of longitudinal components. The transducer resonant frequency is approximately 50 MHz. However, the strain-generating capability of the transducer is about an order of magnitude below expectations. This is determined from the ratio of

the echo signal to the exciting voltage. For longitudinal-mode transducers, the strain-generating capability is near expected values, but the problem of propagating such pulses in a nondispersive fashion presents a fundamental difficulty. Reflection of a longitudinal pulse from the major slide surface generates shear as well as longitudinal strain. The shear propagates across the slide width and generates pulses that trail the main longitudinal pulse. These trailing pulses interfere with memory operation.



INPUT TO TRANSDUCER
12 V. PULSE

Fig. 7—Echo response of evaporated-layer CdS shear transducer.

Experimental Device Performance

Dynamic writing and nondestructive retrieval of random patterns of information were accomplished with devices using discrete film elements and with devices using continuous-film strips.

The device shown schematically in Fig. 8 consist of a fused-quartz slide with discrete magnetic film patches on 40-mil centers, corresponding to 25 bpi. A large, 200-mil diameter, patch is also deposited on the slide to permit *B-H* loop testing. A digit drive winding along the hard axis overlays the magnetic bits. A zig-zag sense winding to pick up the flux in the hard direction is superimposed on the magnetic bits as shown in Fig. 8. The two windings are on opposite surfaces of a Mylar sheet that is superimposed on the glass slide. Figure 9 shows the expanded sense signals corresponding to seven adjacent bit locations for

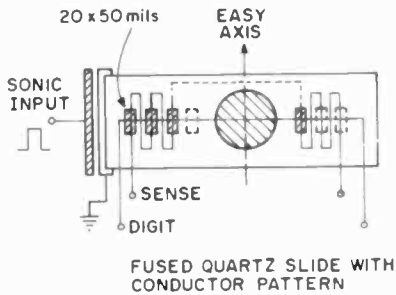


Fig. 8—Memory-test device with discrete film spots.

different information patterns. For this device, the transducer resonance frequency is 3 MHz and the substrate thickness is chosen to permit only the zero-order shear mode to propagate. The transducer resonance frequency is somewhat on the low side for the equivalent bit density resulting in "1-0" discrimination ratio that is marginal for memory operation. The bit transfer rate corresponds to the transducer resonance frequency and is 3 megabits per second per track. For this device, sense signals induced along a digit winding (parallel to the hard direction) are approximately an order of magnitude lower than those shown in Fig. 9. This is to be expected from the geometrical relationships involved in flux linkages.

If the magnetization rotates reversibly an angle θ , due to the strain pulse, the amplitude of the sense signal generated in the zig-zag winding would be proportional to $\sin\theta_r$, and that generated in the digit winding would be proportional to $(1 - \cos\theta_r)$. For small angles, these signals are proportional to θ_r and θ_r^2 , respectively. The small sense signal generated in the digit winding is also to be expected from the plot of Fig. 3a.

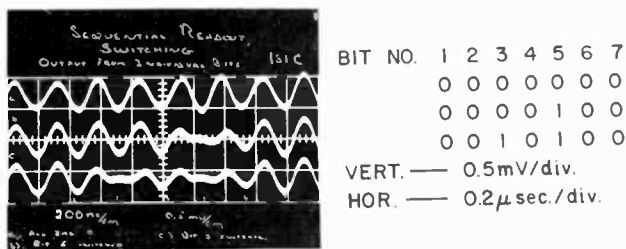


Fig. 9—Sense signals from device of Fig. 7.

For devices using continuous strips, information has been successfully written and retrieved at various bit densities. Writing has been accomplished at 100 magnetization transitions per inch (100 bpi if a single transition per bit is used) using shear pulses propagating in substrates whose thickness deviates considerably from the condition for zero-mode propagation. Figure 10 is a Kerr optic photograph of a film strip in which the magnetization transitions are at a density of 100/inch. For this strip, the easy axis is inclined at 60° to the direc-

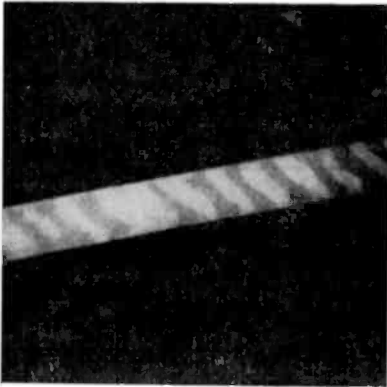


Fig. 10—Kerr-optic photograph of magnetization transition in a continuous strip at a density of 100 per inch.

tion of propagation, and H_c and H_k are approximately 10 Oe. The information stored is stable and is not disturbed by 2000 digit disturbs or by strain pulses numbering in excess of 10^7 . For the tested device, the digit lines are 20 mils wide and require a digit current of approximately 400 mA. Line widths from 10 to 50 mils have also been tested and have shown no qualitative differences in behavior.

Electrical signals obtained on sense windings (along the direction of strain-pulse propagation) with high-bit-density devices do not display sufficient discrimination between "1" and "0" because of the minor strain ripples following the major strain peak as generated by test transducers. This discrimination problem has limited the ability to retrieve information to low densities. Fig. 11 shows the sense output (detected with an amplifier having a bandwidth of 100 MHz) and the corresponding magnetization pattern in a strip of film. Assuming that data is recorded with a single magnetization transition per bit, the pattern of Fig. 10 is equivalent to a density of 50 bpi. The signals from the individual bits are overlapped, rendering detection difficult. Improvements in transducer performance as shown by the echo re-

generated by the strain pulse propagating down the substrate (positive signals) and also by the echo pulse (negative signals). As can be seen, they are uniform in amplitude and wave shape.

For all the devices tested, the film thickness is in the range of 800 to 1200 Å. These test devices utilized Ni-Fe, or Ni-Fe-Co films. The highest transducer excitation utilized in any of the test work is 150 V, with many of the tested devices operating at lower exciting voltages. In all cases, the exciting pulse rise time and duration are adjusted to maximize the strain generated in the substrate and to minimize strain ripples following the main strain-pulse peak, as determined from the echo-signal wave shape.

Cost Performance Characteristics

Preliminary estimates indicate that the memory-bit costs are intermediate between those of a mass-core store and those of electro-mechanical devices such as drums or disks. Figure 13 is a plot showing

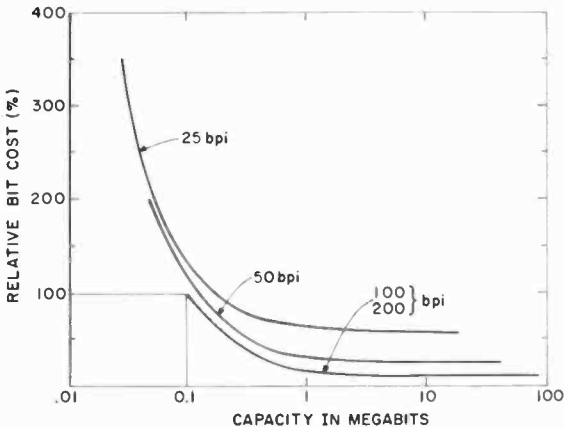


Fig. 13—Normalized bit cost for sonic-film memory.

normalized bit costs as a function of memory capacity and packing density. For the purposes of this estimate, we assume a track density of 25 per inch with 50 tracks per substrate. The substrate length is limited to 20 inches for densities of 25, 50, and 100 bpi, and is 10 inches for a density of 200 bpi to compensate for the increase in the attenuation of strain pulses. The reduction in the overall length of the substrate reduces the total number of bits per substrate and thus tends to

result in a leveling off in bit costs, as shown in Fig. 13. Each substrate is assumed to have a transducer for generating a strain pulse and a set of digit-sense windings overlaying the film strips. The sense digit windings on different substrates may be serially interconnected for a maximum of 10 substrates to reduce the complexity of the electronics package for large-capacity systems. Further, we assume that 10 tracks are simultaneously operated for write or read modes. Thus, sufficient electronics are provided to permit the operation of 10 tracks in parallel.

As the capacity of the memory increases, it is possible to share the drive and sense electronics resulting in a reduction in bit costs, as shown in the figure. For capacities on the order of 1 megabit and above, the bit cost essentially levels off, since no further sharing of electronic circuitry is possible.

From a performance point of view, the high bit densities result in high-bit-transfer rates and smaller physical size for the memory. For a fixed block length, the time required to transfer an entire block is reduced as the bit density is increased. Since the actual time required to energize a transducer is of the order of 1 microsecond, the transfer time of a block is inversely proportional to the bit transfer rate.

An additional feature of the sonic film memory is the possibility of multiport operation. The cost estimates as presented in Fig. 13 include an appreciable amount of electronic circuitry that will not be increased drastically for multiport operation. Thus, higher performance, in terms of bit transfer rates, or block transfer rates, or multiport capability, may be realized without a significant increase in bit costs.

Conclusions

The sonic film memory offers cost-performance advantages for data-processing applications when compared to a mass core memory or electromechanical storage devices. Briefly, the advantages are short latency time, high bit-transfer rate, and a reasonably low bit cost. The main disadvantage of the memory is the fixed block length imposed by the substrate dimensions. The maximum block length, as determined by physical limitations,¹ is on the order of 2000 bytes.

Acknowledgments

The authors wish to acknowledge the continued interest of J. A. Rajchman, Staff Vice-President, Information Sciences, RCA Laboratories, Princeton, New Jersey. D. Leibowitz greatly assisted in the

fabrication of CdS evaporated layer transducers; A. Monsen and T. Ward were instrumental in many phases of this work and were primarily responsible for device and sample preparations.

References

- ¹ H. Weinstein, L. Onyshkevych, K. Karstad, and R. Shahbender, "Sonic Film Memory," **Proc. Fall Joint Comp. Conf.**, 1966, p. 333; also **RCA Review**, Vol. 28, p. 317, June 1967.
- ² R. Shahbender, P. Herkart, K. Karstad, H. Kurlansik, and L. Onyshkevych, Final Report, Contract No. DAAB07-68-C-0030, U. S. Army Electronics Command, Fort Monmouth, N. J., "Magneto Sonic Techniques for BORAM," Oct. 1968.
- ³ T. S. Crowther, "Angular and Magnitude Dispersion of the Anisotropy in Magnetic Films," **J. Appl. Phys.**, Vol. 34, p. 580, 1963.
- ⁴ L. S. Onyshkevych, "Strain-Sensitive Thin Magnetic Films," **J. Appl. Phys.**, Vol. 39, p. 1211, Feb. 1968.
- ⁵ W. P. Mason, ed., **Physical Acoustics**, Vol. I, Part A, Academic Press, New York, 1964.
- ⁶ N. Foster, G. Coquin, G. Rozgoni, and F. Vannatta, "Cadmium Sulphide and Zinc Oxide Thin-Film Transducers," **IEEE Trans. on Sonics and Ultrasonics**, Vol. SU-15, p. 28, Jan. 1968.

Electron Optics and Signal Read-Out of High-Definition Return-Beam Vidicon Cameras

Otto H. Schade, Sr., RCA Electronic Components, Harrison, N. J.

Abstract—Resolving powers of 100 line pairs/mm, or 10000 lines, are obtained with television cameras containing a high-resolution sensor and advanced electron optics designed to provide uniform definition in a 50-by-50-mm format. It is shown that five critical camera components must have modulation-transfer factors of 66% or higher at 100 line pairs/mm to obtain this definition. The theory and design for minimum aberrations in the electron optic are treated in some detail and illustrated by numerical calculations.

This evaluation is followed by a discussion of the operational characteristics and performance of high-resolution television cameras. Aside from slow-scan read-outs for recording purposes, a flicker-free display of constant brightness with a bandwidth-limited resolution of 4000 lines can be obtained, without a storage converter, for direct visual observation from a single exposure by a multiple-frame fast-scan read-out. Constant signal output and exceptionally low noise are achieved with a 100-MHz video pass band during a display time of 20 seconds by automatic read-out controls and by noise integration in the long-persistence phosphor of a high-definition cathode-ray-tube monitor.

Electron Optics and Modulation-Transfer Functions

The Signal-Read-Out System

Photosensitive charge-storage surfaces comparable to high-resolution aerial film have been known for some time, although refinements have been necessary for adaptation to large-image formats. ASOS (antimony trisulfide oxysulfide) photoconductors can store electron densities more than 20 times higher than the maximum grain density of the best high-resolution film, and their basic quantum efficiency exceeds that of photographic emulsions by two orders of magnitude. The full use of the quantum efficiency, however, is limited by the dielectric characteristics and the electron-acceptance factor of the photoconductor in the signal-read-out process by an electron beam. The development of a read-out system for a 50-by-50-mm format that yields

resolving powers of 80 to 100 line pairs/mm for observation in the final image has presented many problems. The nature of these problems is best understood by reference to the diagram of the read-out electron optic shown in Fig. 1.

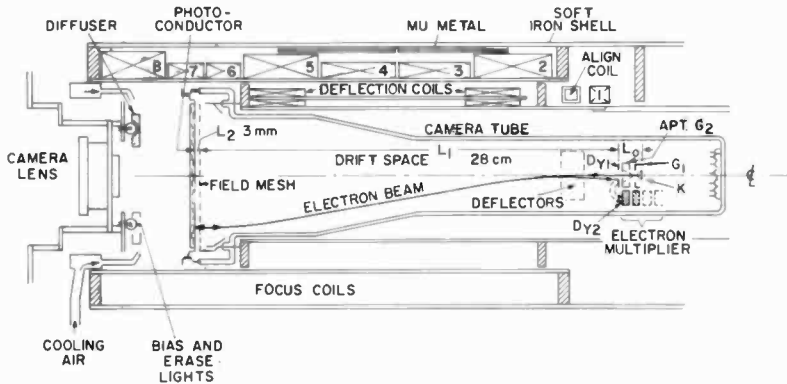


Fig. 1—Electron optic of 4½-inch return-beam vidicon.

The camera tube is immersed in an axial magnetic field. Most of the space in the tube is needed for the read-out system. The space L_0 is occupied by an electron gun in which electrons from a thermionic cathode are accelerated to a high velocity. The gun contains an electron lens that projects a magnified image of the emitting-cathode area onto the exit electrode (g_2). This electrode contains a small aperture, 17 to 25 μm in diameter, that defines the diameter of the electron source at potential V and, in combination with magnification in the gun, limits the energy spread of the electrons that emerge from the defining aperture.

The large space L_1 between this electron source and the storage surface is a field-free drift space at potential V terminated by a field mesh. The length (28 cm) of the space L_1 is needed to deflect the electron beam over a 50×50 mm format with low aberration and reasonable power by transverse magnetic fields generated by an external coil system.

The space L_2 between the field mesh and the storage surface is a short (0.3 cm) decelerating space that minimizes aberrations by a high electric field when the electrons are slowed down so that they land with near zero velocity on the small charge potentials of the storage surface.

The spaces L_1 and L_2 , together with the externally generated

magnetic fields, constitute the read-out electron optic that images the electron source (gun aperture) on the storage surface. The magnification (M_o) of the read-out optic should be smaller than unity to demagnify the image of the gun aperture. The strength of the axial magnetic field (B_z) is that required to focus the beam at the storage surface. The absorption of beam electrons at the storage surface is a function of the charge potential. Video-signal currents appear in the target lead and as a modulation of the reading beam, which returns through the electron optic and retraces its principal path to the gun aperture. Before the return beam reaches the gun aperture, it is deflected slightly by a weak transverse electric field between two deflector electrodes to land on the surface of dynode No. 1 in front of the aperture plate, where it generates secondary electrons that are pulled into an electron multiplier for further amplification.

Modulation Transfer in an n-Component System

The modulation transfer function (MTF) of the camera is the product of the MTF's of seven spread functions, as follows: camera lens, photoconductor, read-out electron optic, field mesh, geometric aperture image, electron multiplier, and video amplifier. The electron multiplier and video amplifier functions can be eliminated by a complementary design that results in a constant MTF over a pass-band of 100 MHz. The remaining 5 components must have high MTF's because, for equal distribution of losses, the response factor \bar{r} in an n -component system is the n th root of the system response. The response factor may be expressed as

$$\bar{r} = (\bar{r}_{\text{yst}})^{1/n}. \quad [1]$$

This function is shown graphically in Fig. 2. The response required for observation of the resolving power f_r of a system that includes a display device (i.e., for $n = 6$ components) is in the order of 8%. The response factor of all components, therefore, must have a value \bar{r} of 0.66 at the resolving-power frequency. The design objective is a resolving-power frequency f_r of 100 cycles per millimeter. The MTF of the camera alone should be $r_{\text{yst}} = 0.125$ (read on the curve $n = 5$ for $r = 0.66$), and the camera without lens ($n = 4$) must have a response of 19% at 100 cycles/mm. It may not be possible to obtain a response of 66% for all system components because of conflicting requirements; some components, therefore, must have higher MTF's to maintain the same product. This requirement is most difficult to fulfill for the

optical camera lens and the read-out electron optic, which must cover the entire image space.

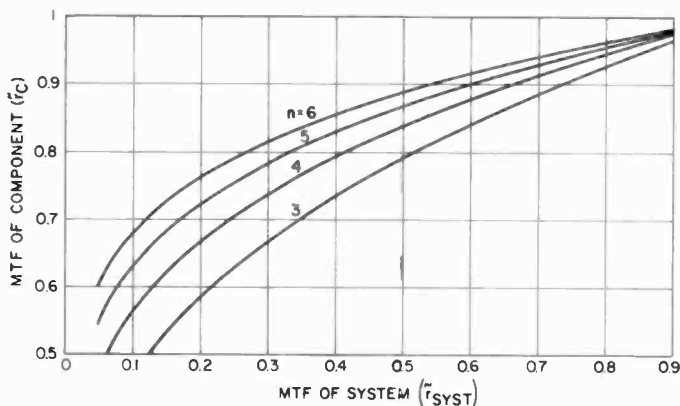


Fig. 2—Response factor (\bar{r}_c) of components in an n -component system as function of system response (\bar{r}_{SYSTEM}).

Modulation Transfer Functions of Camera Components

Camera Lens

Fig. 3 shows curves for a set of MTF's for perfect diffraction-limited lenses of different relative aperture (F/N_o), computed from the following equations:

$$\bar{r}_L = \frac{1}{\pi} (2\beta - \sin 2\beta),$$

$$\beta = \cos^{-1} (f/f_c), \quad [2]$$

$$f_c = 1000/\lambda (F/N_o) \text{ cycles/mm,}$$

$$\lambda = 0.55 \mu\text{m (green light).}$$

A response of 66%, at $f = 100$ cycles/mm, requires a perfect $f:4.9$ lens. MTF's in the order of 60% at 100 cycles/mm are close to the best obtainable at the present state of the art with $f:2.8$ or $f:3$ lenses designed for a narrow spectral response. A nearly ideal lens performance is highly desirable for camera tests and can be obtained with low-cost lenses as follows.

The MTF of a well-corrected $f:5.6$ lens can be made substantially

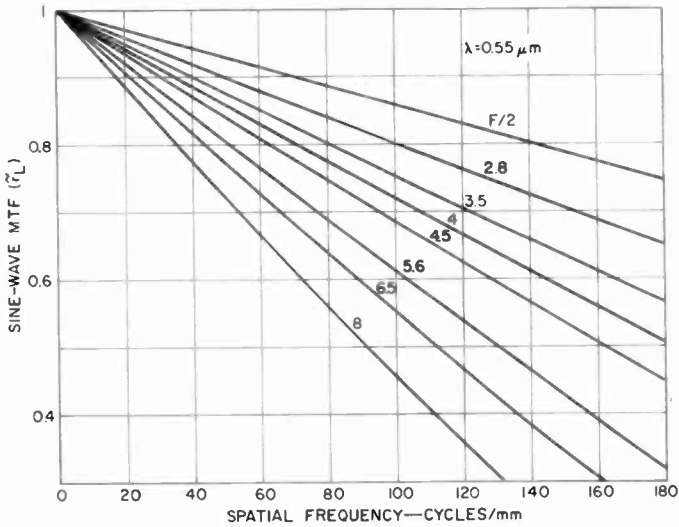


Fig. 3—Modulation transfer functions of perfect diffraction-limited lenses.

uniform within a large frequency range by illumination of a test-object transparency with coherent light from a small source, imaged by a (preferably achromatic) condenser in the plane of the camera lens stop, as indicated in Fig. 4. The light becomes coherent for spatial frequencies

$$f > d_i / \lambda F, \quad [3]$$

where d_i is the diameter of the light-source image at the lens stop and F is the focal distance of the camera lens.

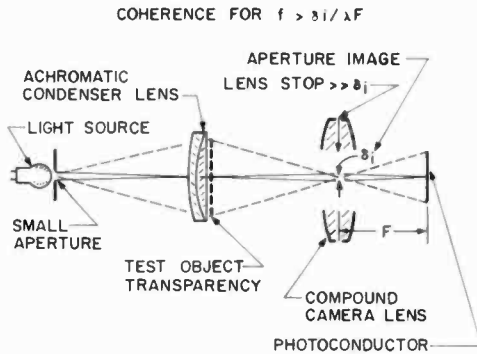


Fig. 4—"Point" source illumination of test object transparency.

The MTF of a 63-mm FAX-EL NIKKOR lens, measured on a sine-wave lens bench with noncoherent and coherent white-light illumination, is shown in Fig. 5.

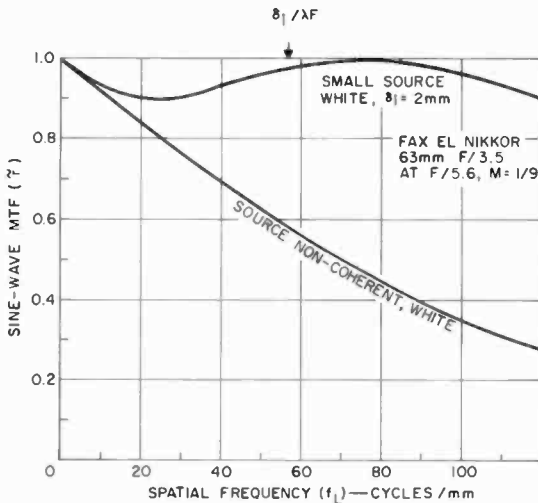


Fig. 5—MTF's of FAX-EL-NIKKOR lens measured with noncoherent and coherent illumination at $f:5.6$.

Photoconductor

The point-spread function of a photoconductor is determined by the potential spread on its vacuum side caused by a point illumination. The MTF of the potential spread caused by a point charge is¹

$$\bar{r}_{ph} = (1 - e^{-x})/x, \quad [4]$$

where $x = 4\pi fd \times 10^{-3}$, d is the thickness in μm , and f is the frequency in cycles/mm.

This function, shown graphically in Fig. 6, applies to the first scan of a storage surface after exposure. The exact MTF of actual photoconductors is not known, and may depart from this estimate because of a nonuniform dielectric. The MTF is, in principle, inversely proportional to the thickness of the photoconductor, which is of the order of $1 \mu\text{m}$ for present ASOS surfaces. The effective thickness of a nonuniform dielectric is uncertain. A response factor of 66%, therefore, may require a photoconductor thickness of $0.7 \mu\text{m}$.

Electron Source and Beam Diameter

The source diameter of the scanning beam is defined by the limiting aperture of the electron gun. The aperture is imaged by the read-out electron optic on the storage surface with a magnification $M_o < 1$, which results in an effective beam diameter D_{be}

$$D_{be} = D_a M_o, \quad [5]$$

where D_a is the aperture diameter

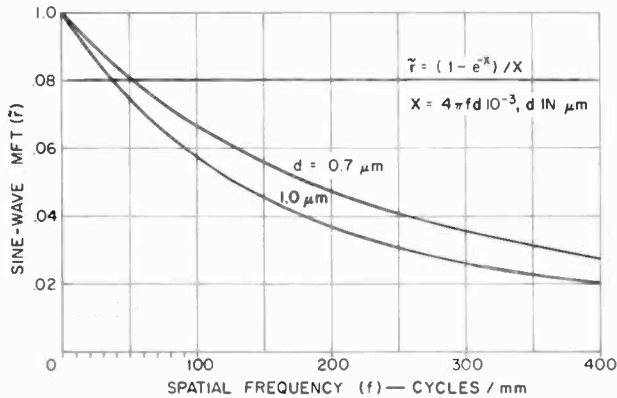


Fig. 6—MTF of photoconductor having a perfect dielectric.

The MTF of the geometric aperture image depends on the current distribution in the gun aperture, which theoretically is substantially uniform for small apertures. The actual current distribution in apertures that have diameters of $25 \mu\text{m}$ or less approaches a cosine shape because of electron interception by the relatively thick aperture walls. Furthermore, the diameter of the effective aperture image at the storage surface may be smaller than the geometric image because of the “self sharpening” effect in low-velocity electron beams, which occurs when the electron density in the beam is larger than required for neutralization of the image charges. In this case, the current distribution in the effective beam diameter becomes \cos^2 , and the beam diameter tends to be smaller than the value given by Eq. [5] because low-velocity electrons do not land on the storage surface. Fig. 7 shows the normalized MTF's for these current distributions. The high-resolution read-out electron optic has a magnification M_o of 0.52, which is computed by

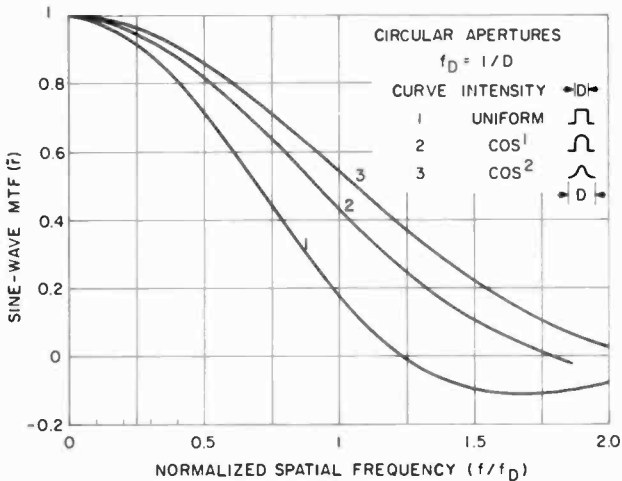


Fig. 7—Normalized MTF's of the geometric aperture image for three current distributions.

tracing electron trajectories from the edge of the gun aperture to the target, as shown by Fig. 8.

A response factor \bar{r} of 0.66 can be obtained with a cos^2 intensity distribution in the aperture image at $f/f_D = 0.8$, as shown in Fig. 7. For $f = 100$ cycles/mm, the effective beam diameter at the target is

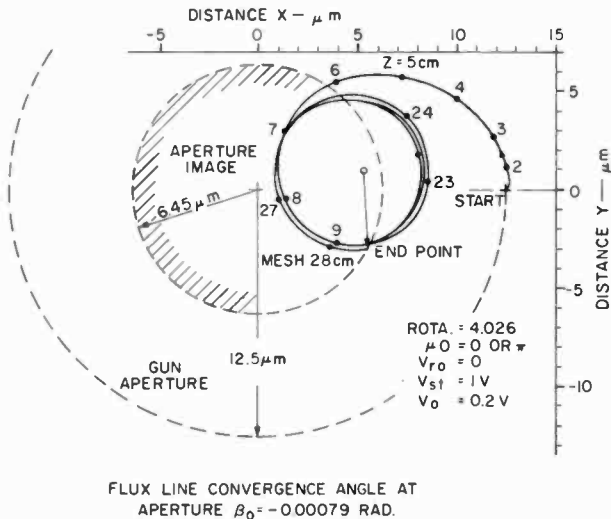


Fig. 8—Computer-calculated electron trajectory from aperture edge, determining the magnification $M_s = 0.52$ of the electron optic.

$D_{be} = 1/f_D = 0.8/f = 0.008 \text{ mm} = 8 \mu\text{m}$ and for $M_o = 0.52$, Eq. [5] yields the aperture diameter $D_a = 15.4 \mu\text{m}$. Although smaller apertures have been made, it must be considered that the choice of aperture size depends on the required aperture current, which may be limited by the current density available from the cathode of the electron gun.

The aperture current is given by

$$I_a = I_S / \alpha \tau_m, \quad [6]$$

where I_S is the beam current that lands on the storage surface, α is the electron acceptance factor at the storage surface, and τ_m is the field-mesh transmission.

The peak current density in small apertures is approximately twice the average current density. The peak current density at the cathode is then

$$I_{K(1)} = 2I_a M_g^2 / \pi \rho_a^2 \quad \text{A/cm}^2, \quad [7]$$

where M_g is the linear magnification in the electron gun determined by the focal length of the control-grid lens and the aperture distance and $\rho_a = D_a/2$ is the radius of the defining aperture in cm.

The magnification M_g must have a value larger than unity to obtain a good electron-energy distribution, as will be explained later. With typical values, $\alpha = 0.25$, $\tau_m = 0.5$, $\rho_a = 0.77 \times 10^{-3} \text{ cm}$, and $M_g = 1.33$, the above equations show that a moderate target signal current of $0.1 \mu\text{A}$ requires an aperture current I_a of $0.8 \mu\text{A}$ and a peak cathode current density $I_{K(1)}$ of 1.52 A/cm^2 , which is quite high for thermionic cathodes. The choice of gun-aperture diameter and resultant MTF depends, therefore, on the required signal current, which has values less than $0.1 \mu\text{A}$ for slow-scan operation, but higher values for a fast-scan signal read-out.

The Read-Out Electron Optic

The performance of the camera tube depends, in large measure, on the read-out electron optic, which images the electron source (defining aperture of the electron gun) on the photoconductor with a magnification of approximately one half. It is relatively simple to obtain good imaging on the axis, because the chromatic aberration introduced by the spread of electron energies in a point source at the gun aperture is independent of the detailed shape of the axial magnetic field, and can be made small by use of a high electric field in the decelerating space, L_2 . The landing pattern of point-source electrons at the low-potential photo-

conductor depends on the axial- and radial-energy spread of the electrons at the gun aperture and the magnification in the electron optic, as shown subsequently (by Eq. [12]) in the section on *Landing-Point Distribution*. The electron density in the landing pattern is determined by the angular current distribution at the gun aperture, which is a gun characteristic, and must be known to compute the point-spread functions of the electron optic, and finally their transforms, the sine-wave modulation transfer function. Point spread and MTF are functions of focus, as in an optical lens. Numerical evaluations demonstrate that focus for a minimum spread diameter results in a much lower MTF than focus for a high energy concentration near the center of the point image. It is shown subsequently that response factors of 66% are easily obtained and exceeded with a variety of operating conditions and field-mesh spacings.

Good images for off-axis points are far more difficult to obtain because new aberrations, such as coma, astigmatism, image distortion, and a curved field of focus, which are analogous to the aberrations for oblique light rays in optical lenses, can be introduced by deflection of the electron beam. As a consequence, the electrons lose axial energy, and many of them may not be able to land on the low-potential storage surface. Shading or a complete loss of the image at the edges or corners may then result. The major design effort for wide-field optics is the correction of these aberrations which, in electron optics, depend very strongly on the axial magnetic field function $B_z(Z)$ and its radial components $B_r(Z)$ that are added to the transverse deflection field $B_T(Z)$. The simultaneous solution that meets all conditions for minimum or zero aberrations over the entire field cannot be given in closed form and requires electron "ray tracing" by computer, or analog solutions in an experimental camera. The "nulling" of deflection aberrations to obtain a landing-point spread very nearly equal to the chromatic aberration on the axis (a few μm) in the entire 50-by-50-mm field requires a precise balance of radial components in the entrance and exit regions of the deflection field and a specific field function $B_z(Z)$ in the focus coil. It should be apparent that a high-resolution $4\frac{1}{2}$ -inch return-beam vidicon cannot provide good off-axis performance when used in the commercial focus coil of a tube of similar size designed for operation with much larger spread functions.

Chromatic Aberration and MTF's of the Axial Point Image

The point-spread function for paraxial electron beams is independent of the axial magnetic field and is determined entirely by "chromatic

aberration", i.e., by the axial velocity spread of the electrons, which results in variations of the focal length. It is desirable to use a magnification $M_o < 1$ in the electron optic to reduce the diameter of the geometric aperture image. This advantage is exchanged for a loss of axial electron velocity.

The radial electron energies are increased to

$$V_r = V_{ro}/M_o^2, \quad [8]$$

and the axial energies are reduced to

$$V_z = (V_{zo} + V_{ro}) - V_{ro}/M_o^2. \quad [9]$$

The magnification of the electron optic for 4½-inch return-beam vidicons is 0.52. With this value and the typical value $V_o = (V_{ro} + V_{zo}) = 0.2$ V, the axial electron energy is negative for values of V_{ro} greater than 0.54 V. The target potential V_T therefore, must be made positive to allow all electrons to land on the target, i.e.,

$$V_T \geq \frac{V_o}{M_o^2} - V_o. \quad [10]$$

In the continuous-exposure mode, the potential of the target increases automatically to this equilibrium value with minimum critical beam current, and to a somewhat smaller value when the beam current is larger than the value needed for charge neutralization. In the latter case, the slower electrons approaching radial energies V_o/M_o^2 do not land, and an effective velocity spread V_o smaller than 0.2 V results.

Similar conditions exist in the single-exposure read-out mode, in which the target read-out bias V_T can be adjusted to any desired value by a control voltage. Under actual read-out conditions, all electrons from point sources in the leading portion of the beam land on positive potentials, whereas slow electrons from point sources in the trailing portion of the electron beam are rejected, because the target potential has been reduced under the beam. This behavior is referred to as self-sharpening of the beam.

Landing-Point Distribution

For simplification of mathematical relationships, it is assumed that all electrons have the same total energy of emission (eV_o) and must land

on the target. The chromatic aberration caused by transit-time differences² of point-source electrons in the drift space L_1 and in the decelerating space L_2 are additive and result in a landing-point spread ($r = \Delta r_1 + \Delta r_2$) around the axial point ($r = 0$ for focused electrons).

The radial distance r is determined by

$$r = \frac{0.5L_1}{(M_o^2V)^{3/2}} V_{ro}^{1/2}(V_{ro,f} - V_{ro}) + \frac{2L_2}{(M_o^2V)^{3/2}} \left[\left(V_o + V_T - \frac{V_{ro}}{M_o^2} \right)^{1/2} - \left(V_o + V_T - \frac{V_{ro,f}}{M_o^2} \right)^{1/2} \right], \quad [11]$$

where r is the radial distance of the landing point from the axis ($r = 0$), L_1 is the gun-to-mesh distance (drift-space length) in cm, L_2 is the mesh-to-target distance (decelerating-field length) in cm, V is the drift-space potential in volts, V_{ro} is the radial emission energy of an electron, $V_{ro,f}$ is the radial emission energy of a focused electron, V_o is the total emission energy in volts of all electrons under consideration, V_T is the target potential in volts, and M_o is the magnification of the electron optic.

The second term of Eq. [11] can be simplified for numerical evaluation by introduction of the landing requirement stated by Eq. [10] to obtain

$$r = \frac{0.5L_1}{(M_o^2V)^{3/2}} V_{ro}^{1/2}(V_{ro,f} - V_{ro}) + \frac{2L_2}{M_o^2V} V_{ro}^{1/2} [(V_o - V_{ro})^{1/2} - (V_o - V_{ro,f})^{1/2}]. \quad [12]$$

It is evident that the chromatic aberration for paraxial electrons is independent of the magnetic field (B). High axial resolving powers of the electron optic, therefore, can be obtained with any simple focus coil, although such coils will not provide low aberrations off the axis; i.e., for deflected electron beams.

The maximum energy of emission (V_o) is determined by the magnification in the electron gun, which is dependent upon the focal length

of the electric-lens field in the control-grid region, as illustrated by the electron trajectories shown in Fig. 9. The cone of electrons emerging from a point in the gun aperture located at a distance of 120 mils beyond the g_2 entrance aperture has a solid angle $2\theta_{\text{MAX}}$ related to the radial electron energies as follows:

$$V_{r0} = V \sin^2\theta \quad [13]$$

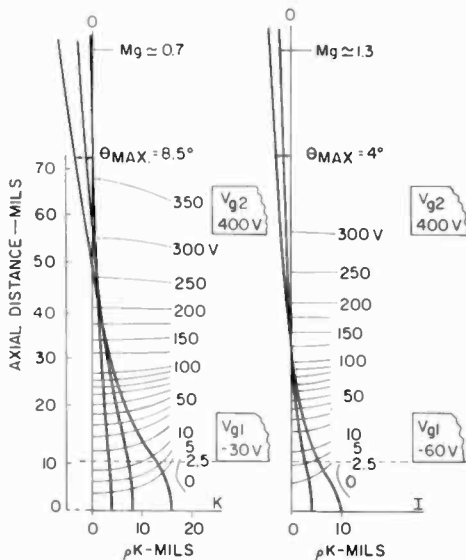


Fig. 9—Potential fields and electron trajectories in standard electron guns.

The angular distribution of current per unit solid angle from a point in the aperture is well approximated for small apertures by

$$i/i_0 \approx \exp\left(-\frac{eV}{KT} M_g^2 \sin^2\theta\right), \quad [14]$$

where $e/KT = 10$ for a cathode temperature T of 1160°K , $M_g = \rho_g/\rho_k$ = linear magnification in the electron gun, and θ = angle of the electron path to the Z -axis at potential V .

For a drift-space potential V of 400 V and a gun magnification M_g of 1.33, the relative-current ratio i/i_0 decreases to 0.029 for an angle θ of 0.0223 radian, which according to Eq. [13] corresponds to a voltage

V_{ro} of 0.2 V. The small value of the angle θ permits the simplification $V_{ro} = (\theta/\theta_{\max})^2 V_{r_{\text{omax}}}$ to calculate V_{ro} as a function of the angular distribution at the point source for zones of equal angular increments, as shown by columns 1 and 2 in Table I, in which radial energies larger than $V_{r_{\text{omax}}} = V_o = 0.2$ V are neglected.

The landing-point spreads Δr_1 and Δr_2 , computed by the two terms of Eq. [12] for a 4 $\frac{1}{2}$ -inch return-beam vidicon operated with a drift-space potential of 700 V are shown in Figs. 10(a) and 10(b). These spreads demonstrate that the aberration Δr_1 in the long (28-cm) drift space L_1 is smaller than the aberration in the short (0.3-cm) decelerat-

Table I—Computation of Aberrations Δr_1 and Δr_2 for $V = 700$ volts, $V_o = 0.2$ volt, $V_r = 0.54$ volt $M_o = 0.52$, $L_1 = 28$ cm, $L_2 = 0.3$ cm for five focus conditions ($V_{r_{o,f}}$).

θ/θ_{\max}	V_{ro}	Radial Aberration Δr_1 for 5 Focus Conditions $V_{r_{o,f}}$ (μm)				
		$V_{r_{o,f}} = 0.0$	$0.3V_o$	$0.5V_o$	$0.75V_o$	V_o
0.1	0.002	-0.0048	0.14	0.237	0.357	0.477
0.2	0.008	-0.0385	0.251	0.444	0.684	0.926
0.3	0.018	-0.13	0.306	0.592	0.954	1.315
0.4	0.032	-0.309	0.27	0.662	1.135	1.62
0.5	0.050	-0.603	0.123	0.604	1.205	1.81
0.6	0.072	-1.035	-0.173	0.405	1.115	1.85
0.7	0.098	-1.655	-0.641	0.0337	0.875	1.72
0.8	0.128	-2.46	-1.32	-0.539	0.422	1.39
0.9	0.162	-3.51	-2.21	-1.34	-0.39	0.825
1.0	0.20	-4.82	-3.37	-2.41	-1.20	0.0
		Radial Aberration Δr_2 for 5 Focus Conditions $V_{r_{o,f}}$ (μm)				
0.1	0.002	-0.00426	0.101	0.182	0.314	0.632
0.2	0.008	-0.0284	0.182	0.344	0.606	1.28
0.3	0.018	-0.0935	0.221	0.464	0.856	1.81
0.4	0.032	-0.216	0.204	0.528	1.06	2.325
0.5	0.050	-0.426	0.099	0.505	1.165	2.75
0.6	0.072	-0.765	-0.136	0.348	1.14	3.04
0.7	0.098	-1.27	-0.525	0.013	0.953	3.17
0.8	0.128	-2.04	-1.20	-0.555	0.50	3.04
0.9	0.162	-3.22	-2.38	-1.555	-0.39	2.48
1.0	0.20	-6.35	-5.30	-4.5	-3.18	0
		Total Landing-Point Spread, $r = \Delta r_1 + \Delta r_2$ (μm)				
θ/θ_{\max}	$V_{r_{o,f}} = 0$					
0.1	-0.0091	0.24	0.419	0.671	1.109	
0.2	-0.0669	0.433	0.788	1.290	2.206	
0.3	-0.2235	0.527	1.056	1.81	3.125	
0.4	-0.525	0.474	1.19	2.195	3.945	
0.5	-1.029	0.233	1.109	2.37	4.56	
0.6	-1.80	-0.309	0.753	2.255	4.89	
0.7	-2.925	-1.166	0.163	1.828	4.89	
0.8	-4.50	-2.520	-1.094	0.922	4.43	
0.9	-6.73	-4.59	-2.9	-0.78	3.305	
1.0	-11.17	-8.67	-6.91	-4.38	0.0	

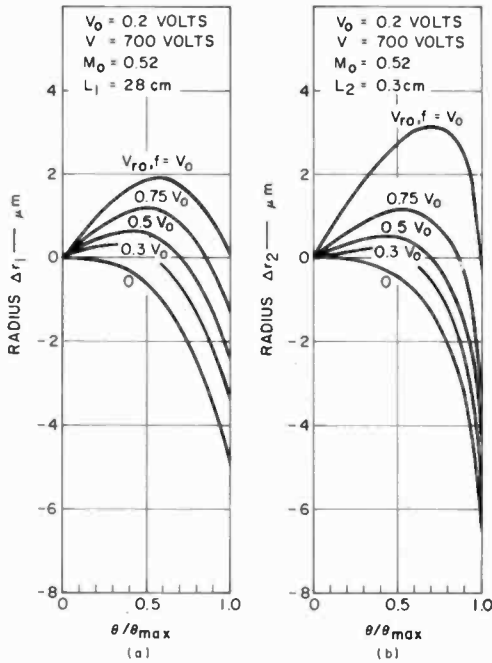


Fig. 10—Landing point spread (a) caused by chromatic aberration in the drift space L_1 , Δr_1 ($\theta/\theta_{\text{max}}$), (b) caused by chromatic aberration in the decelerating space L_2 , Δr_2 ($\theta/\theta_{\text{max}}$).

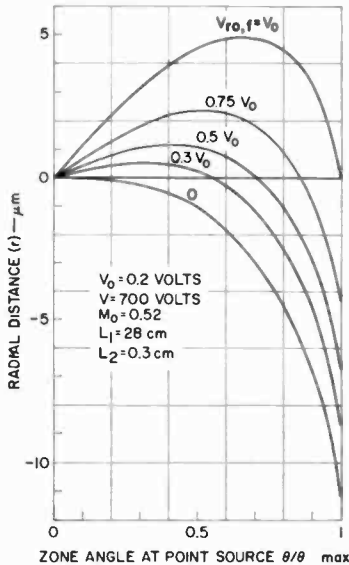


Fig. 11—Total landing point spread $r(\theta/\theta_{\text{max}})$ at target.

ing space L_2 between field mesh and target. The total aberration ($r = \Delta r_1 + \Delta r_2$) is shown in Fig. 11. The functions demonstrate that the focus condition for which $V_{r0,f} = 0.75V_0$ results in a minimum spread diameter, whereas the focus conditions for which $V_{r0,f} < V_0$ produce a larger maximum spread, but concentrate a large percentage of the electron energy near the axis (small r values).

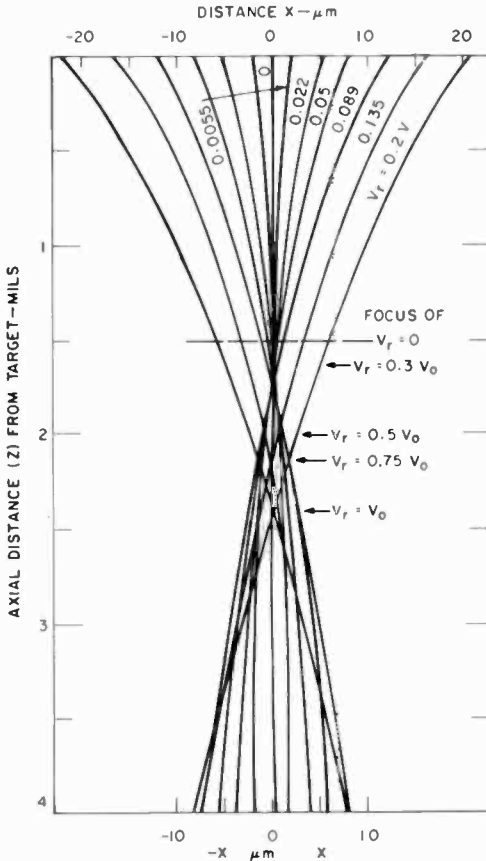


Fig. 12—Electron trajectories in axial point beam showing chromatic aberration for an out-of-focus condition.

The energy concentration as a function of $V_{r0,f}$ is demonstrated in Fig. 12 by the computer-calculated electron trajectories of a point-source beam from the gun aperture focused in front of the target operated at a potential of one volt. The crossover of electron trajectories at their focal points explains the change in sign of the r values.

The focus condition $V_{r_o,f} = V_o$ produces a nearly uniform density of electrons and can be used as a reference value. Fig. 11 shows that the maximum radius occurs at $\theta/\theta_{\max} = 0.66$, which corresponds to $V_{r_o} = 0.435V_o$. With this value substituted into Eq. [12], the diameter ($D_o = 2r_{\max}$) of the circle of confusion is given by

$$D_o = 0.373L_1(V_o/M_o^2V)^{3/2} + 1.99L_2V_o/M_o^2V. \quad [15]$$

The diameter D_o can be used as a reference to determine the scalar value of the r -functions for different operating potentials and the effect of these values on the spread function and modulation-transfer function (MTF), as discussed later.

Point-Spread Function

The intensity distribution $i(r, V_{r_o,f})$ of the point-spread function, at the source and landing area of the point-source beam, is given by

$$i(r, V_{r_o,f}) = (i/i_o)F_rF_w, \quad [16]$$

where $i/i_o(\theta/\theta_{\max})$ is the current distribution at the point source, as defined by Eq. [14]; $F_r = (\theta/\theta_{\max})/r$ is the ratio of the zone radii; and $F_w = \Delta(\theta/\theta_{\max})/\Delta r$ is the ratio of the zone widths.

The following form is used for numerical evaluation:

$$i(r, V_{r_o,f}) = \frac{(i/i_o)(\theta/\theta_{\max})}{rdr/d(\theta/\theta_{\max})}. \quad [17]$$

Calculation of the spread functions for $V_{r_o,f} = 0$ and $V_{r_o,f} = 0.3V_o$ is illustrated by Table II. The current distribution, for $M_g = 1.33$ and with V_{r_o} defined as in Eq. [13], is $i/i_o = \exp(-17.9V_{r_o})$, as listed in column 4 of Table II. The functions $i(r)$ have infinity points where the radius or the derivative $dr/d(\theta/\theta_{\max})$ passes through zero. The r -functions for the focus conditions $V_{r_o,f} > 0$ have a second zero point because of the crossover of electron trajectories. Summation of currents for coincident r values in the branches r_o to r_{\max} , r_{\max} to r_o , and r_o to $-r_{\max}$ is, therefore, required. (Columns 6 and 7 in Table II show the summation). All current values are positive (disregard signs).

The spread functions for five focus conditions are shown in Fig. 13. The currents are in correct proportion; i.e., the volume of the point images is constant. It is now evident that the focus condition $V_{r_o,f} = V_o$

produces a large circular disk of substantially uniform intensity, whereas the focus condition $V_{r_o,f} < V_o$ reduces the disk radius, increases the current density near the axis, but adds a larger spread diameter of low current density that cannot be neglected in calculations of the MTF.

Table II—Calculation of Spread Function $i(r, V_{r_o,f})$

θ/θ_o	r	$dr/d\theta$	i/i_o	$i(r)$		
$V_{r_o,f} = 0.0$						
0.0	0.0	0.3	1.0	∞		
0.1	0.0091	0.334	0.96	31.7		
0.2	0.0669	1.072	0.87	2.42		
0.3	0.2235	2.29	0.725	0.425		
0.4	0.525	4.04	0.57	0.108		
0.5	1.029	6.37	0.415	0.0316		
0.6	1.8	9.47	0.29	0.0102		
0.7	2.925	13.5	0.175	0.0031		
0.8	4.5	17.05	0.10	0.00093		
0.9	6.73	33.5	0.06	0.00024		
1.0	11.17	62.5	0.028	0.00004		
$V_{r_o,f} = 0.3 V_o$					r	Σi
0.0	0.0	2.4	1.0	0.17	0	∞
0.05	0.12	2.39	0.99	0.172	0.02	2.18
0.1	0.24	2.25	0.965	0.178	0.05	1.47
0.15	0.34	2.0	0.923	0.204	0.10	0.88
0.2	0.433	1.60	0.87	0.25	0.20	0.555
0.25	0.50	0.94	0.80	0.425	0.30	0.50
0.30	0.527	0.20	0.725	2.06	0.40	0.56
0.31	0.5271	0	0.72	∞	0.50	1.04
0.35	0.52	-0.52	0.644	0.834	0.53	∞ and 0.039
0.4	0.474	-1.5	0.57	0.32	0.60	0.030
0.45	0.37	-2.43	0.484	0.24	0.65	0.026
0.5	0.233	-3.8	0.415	0.234	1.166	0.0093
0.55	0.0	-5.4	0.341	∞	1.78	0.00417
0.6	-0.309	-6.9	0.29	0.0819	2.52	0.00193
0.65	-0.65	-8.58	0.223	0.026	3.42	0.00092
0.7	-1.166	-11.3	0.175	0.0093	4.59	0.000418
0.75	-1.78	-13.64	0.135	0.00417	6.23	0.000154
0.8	-2.52	-16.4	0.10	0.00193	8.64	0.000053
0.85	-3.42	-20.6	0.076	0.00092		
0.9	-4.59	-28.1	0.060	0.000418		
0.95	-6.23	-40.5	0.041	0.000154		
1.0	-8.64	-61	0.028	0.000053		

Modulation-Transfer Functions (MTF) of the Electron Optic

The MTF of a complex spread function can be computed as follows: The spread function is subdivided into a number of cylindrical sections or disks; the current in these sections is proportional to the volume of

the sections ($r^2\Delta I$), which is normalized as a percentage of the total flux, as shown in Table III for two focus conditions.

Each of the sections has an MTF given by

$$r = 2j_1(X)/X \quad [18]$$

where $X = \pi f/f_D$ and $j_1(X)$ is a Bessel function.

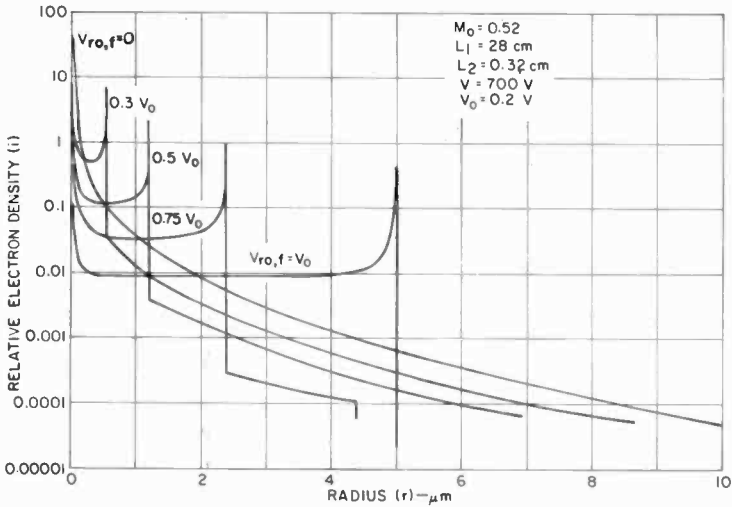


Fig. 13—Point-spread functions of the electron optic for five focus conditions ($V_{ro,f}$).

The index f_D for the frequency scale is equal to $1/(2r)$, and the amplitude at zero frequency is the normalized flux in the section. The total MTF of the spread function is the sum of the MTF's of the cylindrical components, as illustrated in Fig. 14 for $V_{ro,f} = 0$. Fine detail in the spread functions (e.g., narrow peaks) can generally be disregarded when making the subdivision, because of their low flux content. The subdivision of some spread functions requires negative cylindrical components, which then have negative MTF's (as indicated in Table III and Fig. 15).

The MTF's for five focus conditions are shown in Fig. 16. It is evident from a comparison of these curves with those in Fig. 11 that the focus condition $V_{ro,f} = 0.3V_0$ yields the optimum MTF. The amplitude response is approximately 89% at 100 cycles/mm. The electron optic, therefore, is far better than the best camera lens because its

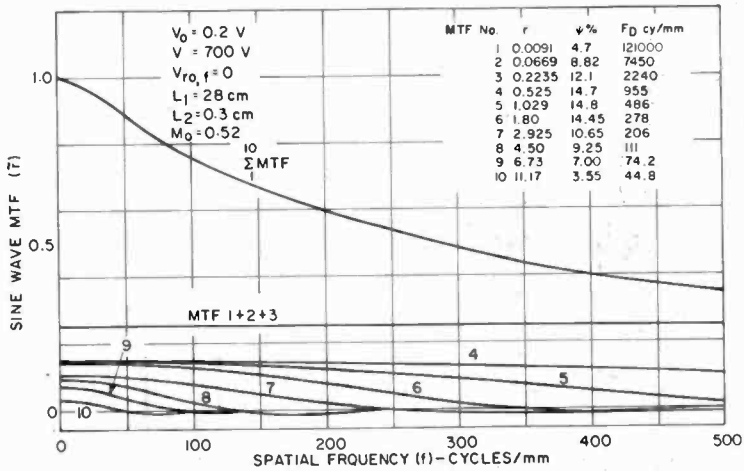


Fig. 14—MTF of point image as sum of component MTF's.

MTF is 62% at 500 cycles/mm, which is approximately that of a "perfect" diffraction-limited $f:1.0$ camera lens at a wavelength of $0.55 \mu\text{m}$.

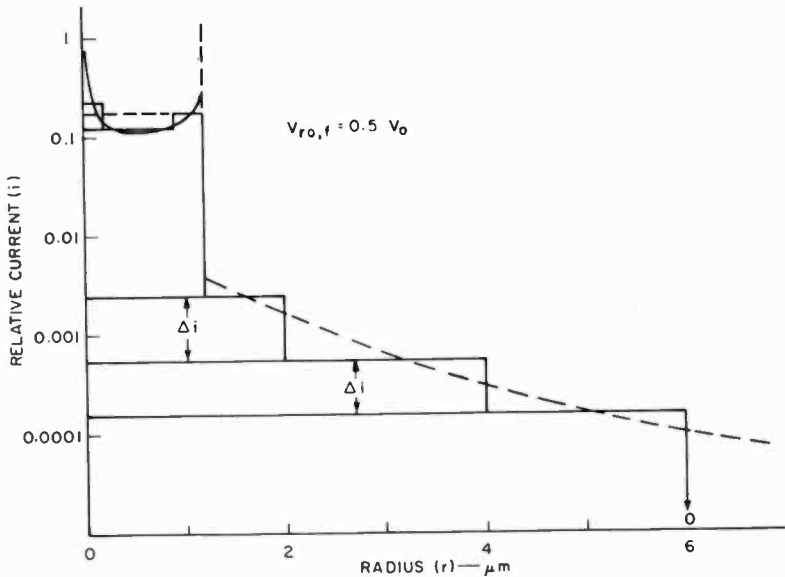


Fig. 15—Subdivision of point-spread function for $V_{r_o,f} = 0.5 V_0$.

Table III—Calculation of MTF Components for Two Focus Conditions

r (μm) $V_{r_o,f} = 0.3 V_o$	i	Δi	$r^2 \Delta i$	ϕ (%)	$f_D = 1/(2r)$ cycles/mm
0.05	2.0	1.1	0.0075	2.8	10000
0.15	0.9	0.35	0.0080	3.0	3330
0.45	0.55	-0.50	0.101	-38.0	1110
0.53	1.05	1.04	0.292	110.0	935
1.80	0.01	0.008	0.026	9.8	278
3.20	0.002	0.0016	0.0164	6.18	156
5.60	0.0004	0.0003	0.0094	3.54	89.4
8.40	0.0001	0.0001	0.0070	2.64	59.5
<hr/>					
$V_{r_o,f} = V_o$					
5.0	0.040	0.04	1.00	313.0	100
4.7	0.0085	-0.0315	0.68	-213.0	106.2

Note: The near axial current spike contains negligible flux and is neglected.

MTF of the Electron Optic as Function of the Potential and Field-Mesh Spacing

The frequency scale of the MTF's shown in Fig. 16 is determined by the constants V , V_o and the distances L_1 and L_2 . A scale factor for different potentials V or mesh spacings L_2 can be computed from the following ratio:

$$f/f_r = D_{o(700)}/D_o \quad [19]$$

where $D_{o(700)}$ is the reference diameter computed for the reference

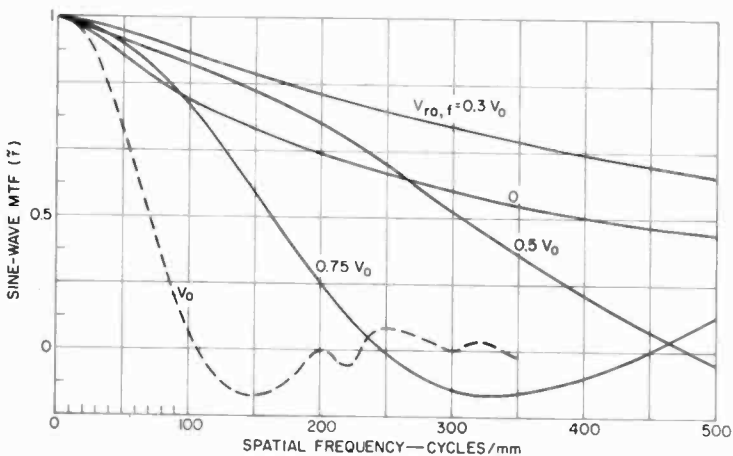


Fig. 16—MTF of the electron optic as a function of focus ($V_{r_o,f}$).

constants given in Fig. 14 and D_o is the diameter computed from Eq. [15] for potentials other than 700 V, or for different mesh spacing.

Scale factors (f/f_r) computed for three mesh-to-target spacings are shown in Fig. 17 as function of the drift-space potential of the 4½-inch return-beam vidicon. The MTF of the electron optic is a nearly linear function of the drift-space potential V , which in turn is proportional to the excitation power of the focusing field and the deflection power.

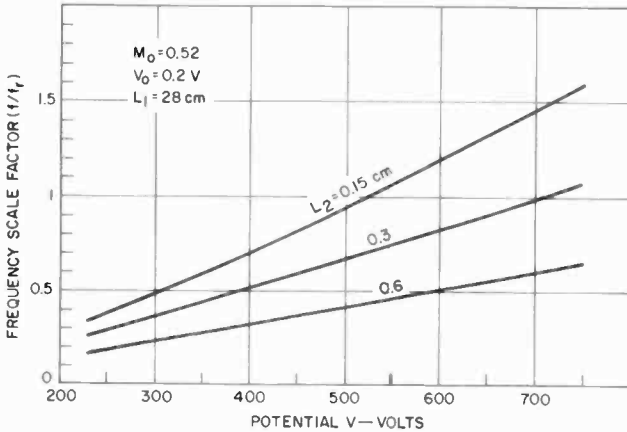


Fig. 17—Frequency scale factor f/f_r of MTF of the electron optic as a function of potential (V) and mesh spacing (L_2).

Reduced mesh spacings result in a substantial saving in power because the same performance can be obtained at lower potentials. It should be noted, however, that reduced mesh spacings require a finer mesh pitch to prevent mesh visibility.

The modulation transfer factors (\bar{r}) at three spatial frequencies are shown in Fig. 18 as functions of the voltage for the standard values of the distances L_1 and L_2 and the focus condition $V_{r_o, f} = 0.3V_o$. It is apparent that a response greater than 66% at 100 cycles/mm is readily obtainable for image points near the axis.

Correction of Aberrations and MTF for Off-Axis Points

The design of an electron optic that minimizes the point-spread function when the beam is deflected over a large format is a principal problem in the development of a high-resolution camera. The analysis is complex, and the solution cannot be stated in closed form. The landing-point spread can become much larger than computed for the

chromatic aberration on the axis. An electron may acquire additive or subtractive radial energy at any point of its trajectory when it encounters a region of flux line curvature, because the incremental deflection angle of the flux line is added vectorially to its normal θ angle. This condition occurs particularly in the entrance and exit regions of the deflection space in which the magnetic flux lines have strong curvatures, as shown by curves 1 and 2 in Fig. 19 for a de-

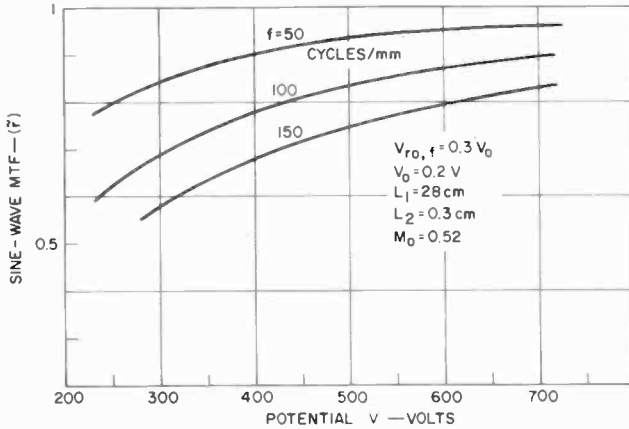


Fig. 18—MTF's of the electron optic as a function of potential (V) for three spatial frequencies.

flexion in the X - Z plane. The principle of nulling the radial energy acquired in a curved field is well known^{3,4} and readily understood for constant- B fields warped by a transverse field to have regions of constant curvature and regions without curvature. Cancellation of aberrations requires that the lengths of these regions be integral multiples of the period of the circular-motion component of the electron. In this case, the derivative δ' of the flux line angle is constant, and its vectorial addition to θ_0 is nulled independently in entrance and exit curvatures after one complete rotation ($\mu = 2\pi$) of the electron, as illustrated by curves 4 to 6 in Fig. 19.

Further examination shows that a θ -error caused by a non-integral value (l/λ) in the entrance curvature can be cancelled by an equal error of opposite phase in the reversed curvature of the exit region of the deflection field. This cancellation arrangement requires that a nodal point be placed at the deflection center. It is evident that at least two loop lengths are required to null deflection aberrations completely.

The uniform flux density and constant radius of curvature of the

simple theoretical model are difficult to realize with practical small-diameter coil systems, and conditions are even more complex for a converging nonuniform axial field, which is required to provide a demagnification, i.e., an $M_o < 1$.

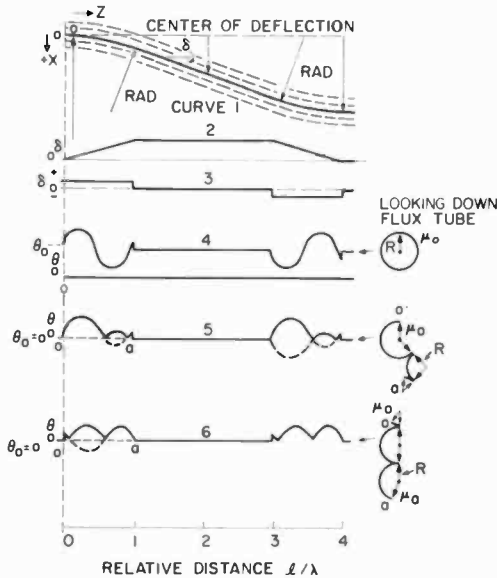


Fig. 19—Deflected flux lines, deflection angle (δ) and $\theta(Z)$ functions demonstrating the principle of nulling deflection aberrations.

There are, in principle, two methods for adjustment of the ratio of the axial to the transverse magnetic field strength, which controls the deflection angle δ and curvature of the flux lines. One method is to shape the transverse-field function of the deflection-coil system by mechanical adjustment of the axial wire lengths of the coils, which is difficult and invariable for any given winding configuration after assembly. In the second method, which is employed in the high-definition camera, the transverse field of the deflection coils is modified by addition of static radial components $\pm B_r(z, r)$ generated as derivatives of the axial-field function $B_z(z, r)$, which can be controlled by variation of the excitation of field-coil sections located at appropriate z values.

This method provides a continuous variation of radial components by electrical means and precise control of the flux-line curvature that can be made during operation of the camera by adjustment of the

excitation current in the coil sections with shunt rheostats.

The functions 1 and 2, shown in Fig. 20, are equivalent axial and transverse summation fields, $B_z(z)$ and $B_T(z)$, respectively, along a deflected flux line (the principal path of the electron) for a 1.9-cm deflection.* The central minimum in $B_z(z)$ of curve 2 is controlled by coil No. 4, and the minimum at the target is controlled by coils Nos. 6

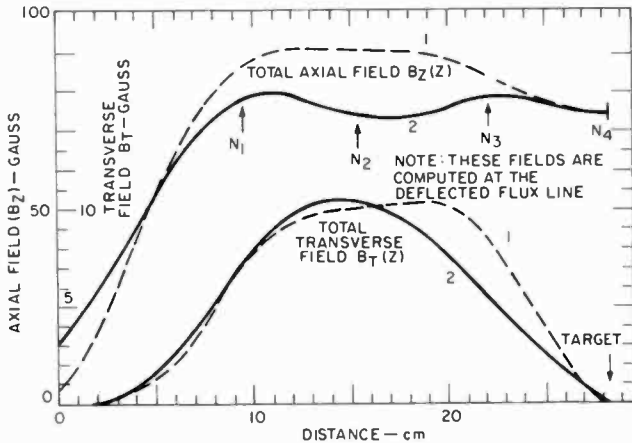


Fig. 20—Computer-calculated axial and transverse summation fields along a deflected flux line for a 1.9-cm deflection at the target.

and 7, which are nearly shorted out, and by coil No. 8 (Fig. 1 shows the locations of the coils.) Optimum multiplier operation and positioning of the first nodal point N_1 requires adjustment of the "bucking" coil No. 1. The curves of $B_T(z)$, shown in Fig. 20, illustrate the electrical control of the transverse-field function by the static radial components of the axial field. The control over the flux-line curvatures and deflection angle $\delta(z)$ is evident from the curves shown in Fig. 21.

Computer-calculated $\theta(z)$ functions for the field functions 1 and 2 of Fig. 20 are shown in Figs. 22 and 23, respectively. The field function without central minimum provides independent nulling of deflection aberrations, such as shown in Fig. 22, and a somewhat smaller residual θ error from the deflection exit region than the function 2, which, however, provides improved electron landing at the corners of the image and uniform signals with photoconductor polarizing poten-

* The functions are computer calculated from measured field data and contain equivalent B_r components caused by electric-lens fields.

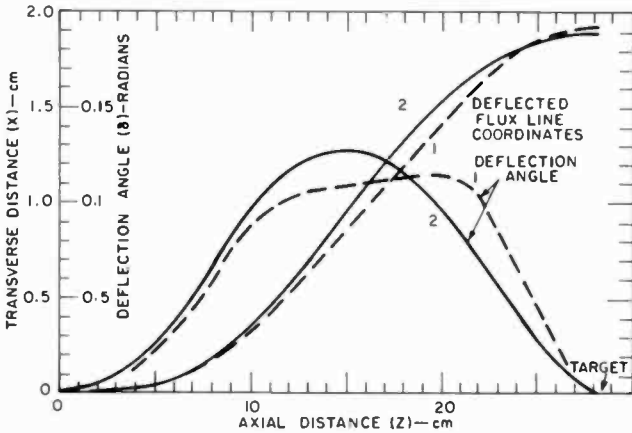


Fig. 21—Correction of flux-line curvature (curve 2) in the deflection exit region by static radial B -field components generated by modification of the focus-coil field (curve 2, Fig. 19).

tials as low as 0.5 V above beam cutoff. This behavior is not evident from the θ functions computed for the x-deflection. An exact agreement of computed functions with observed results is unlikely, because although calculations are made with the field data measured on the real camera adjusted for optimum operation, these input data contain cor-

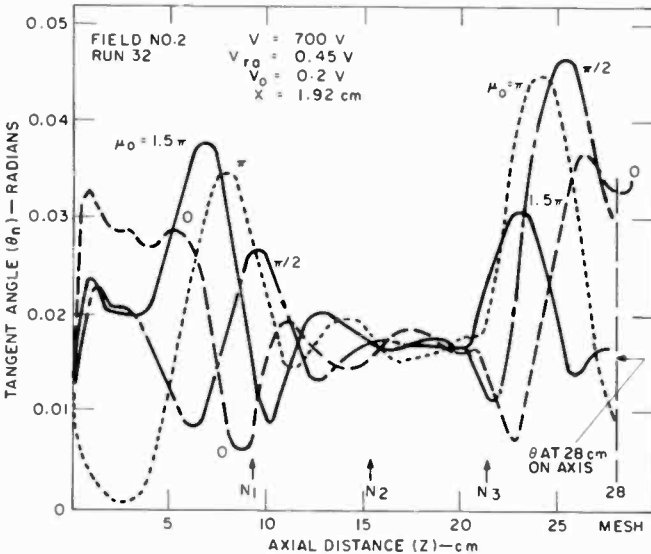


Fig. 22— $\theta(Z)$ -functions computed for an earlier solution (curve 1 in Fig. 19).

rections for incidental geometric distortions that occur in the camera and that cause deviations from optimum conditions in the geometrically accurate computer model.

Corrections by electrostatic-lens fields in the target region are held to a minimum to prevent astigmatism. It should be noted that a nodal point N_2 occurs at the deflection center.

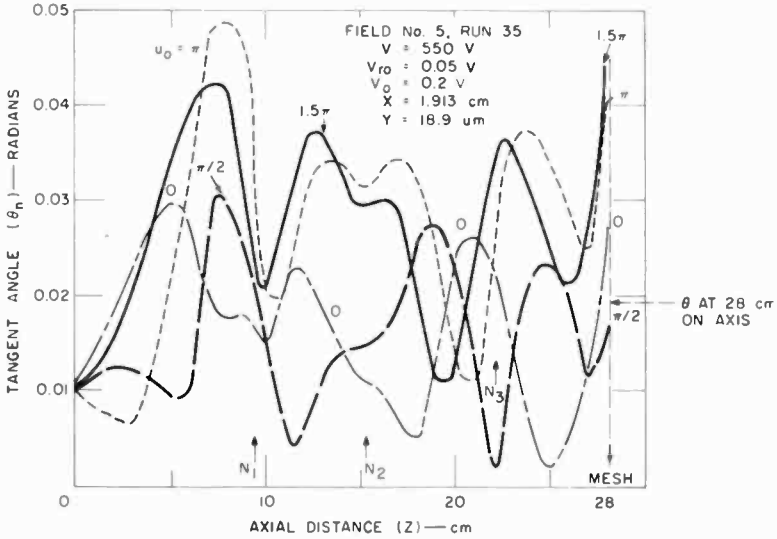


Fig. 23—Computer-calculated $\theta(Z)$ -functions of a high-resolution electron optic (curves 2 in Fig. 19).

The simple concept of an integral number of electron rotations that occur in mathematically uniform fields does not apply to real cameras, because of the additive variable radial-velocity components and the nonuniform B field along the principal electron path. The rotation computed for initial values, i.e., $\mu_0 = 0, \pi/2, \pi,$ and 1.5π at the gun aperture, is shown in Fig. 24 for a 1.9-cm deflection. The “circular” motion of these electrons is far from circular,[†] as shown in Fig. 25 by the coordinate deviations ΔX and ΔY of four electrons from their principal path, which is collapsed into a point $\Delta X, \Delta Y = 0$. The particular calculation is 0.17% out of focus, and the nodal point N_4 occurs in front of the target. The nodal points and loop wavelengths λ_1 to λ_4 are shown by the side view of the trajectories in Fig. 26. The out-of-

[†] The electron motion becomes more circular for large radial components.

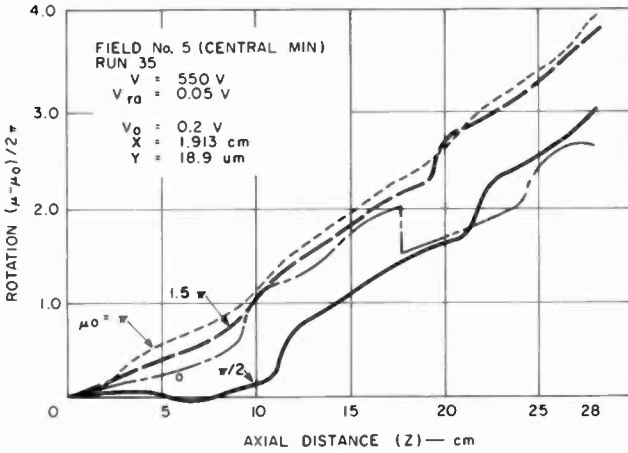


Fig. 24—Rotation of electrons in a deflected electron beam.

focus calculations of the computer illustrates the chromatic aberration on the axis at the fourth nodal point (shown in Fig. 12), which occurs approximately 1.7 mils in front of the target.

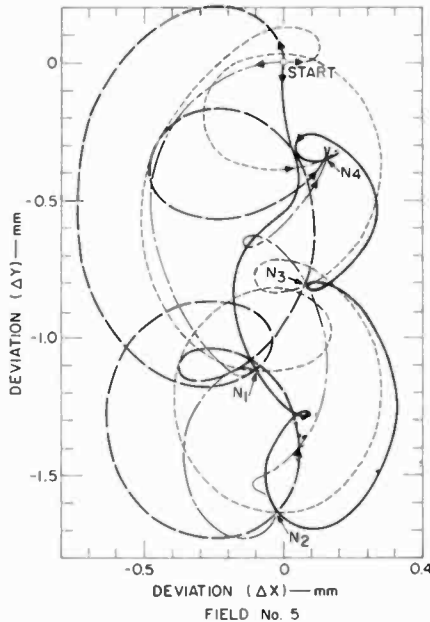


Fig. 25—Helical-motion component $(\Delta X, \Delta Y)$ of four electrons in a deflection field.

The cumulative numerical error in the computer calculations is proportional to V_r and is approximately $0.2 \mu\text{m}$ for $V_r = 0.2 \text{ V}$ and a 28-cm-long paraxial electron trajectory. The error in off-axis calculations is not known and could be larger because of the more complex electron trajectory, which is calculated in 564 incremental steps.

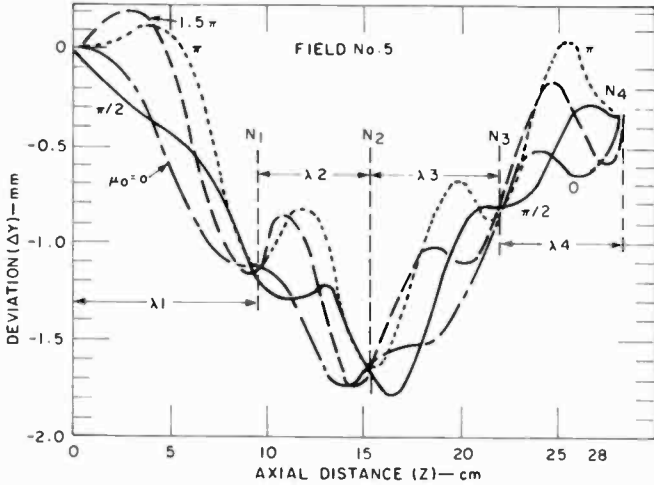


Fig. 26—Side view of electron trajectories in a deflected beam.

Computed calculations of landing-point distributions for deflected electron point beams show that point spread and focus are very sensitive to weak electric fields formed in the target region by potential differences between the field mesh g_5 and the drift space g_4 . Such fields can introduce astigmatism. Again, because of geometry errors in the actual tube, the calculations do not agree exactly with observations. Experimental tubes that have optically flat faceplates and precision glass envelopes provide a constant resolving power of 100 cycles/mm and a flat field of focus over the entire format area without dynamic corrections.

The focusing field must decrease at the target with radial distance from the axis (field dip in the deflection exit region) to provide a flat field of focus. Moreover, a general field symmetry with respect to the central nodal point is necessary to eliminate image rotation and S distortion. The simultaneous solution for a flat field of focus, minimum geometric distortion, uniform electron landing, and constant MTF's

within the image format requires four nodal points.* These characteristics are not obtained when the camera tube is operated in the focus-coil system of a commercial 4½-inch image-orthicon camera.

Field Mesh

The field-mesh wires intercept a certain percentage of the beam current, given by the mesh transmission factor τ_m , which is 50% for a mesh period of 40 cycles/mm (1000 per inch) and 40% for a 60-cycle/mm mesh. The field perturbations caused by the mesh cause aberrations of the electron trajectories, which can be described by the MTF of the field mesh. The MTF at the mesh frequency can be de-

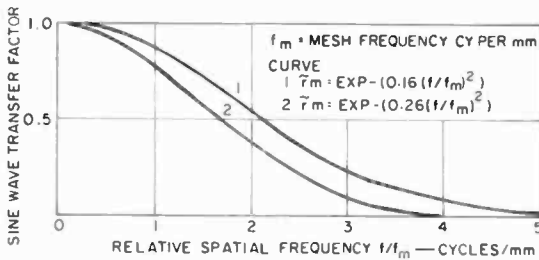


Fig. 27—Normalized MTF of field mesh.

termined by measurement of the modulation m_1 of the return beam when the beam is focused on the gun side of the mesh, and the modulation m_2 when the beam is diffused by passage through the mesh field, reflected by a negative target, diffused a second time in the mesh field, and focused on the target side of the mesh. This MTF can be approximated by

$$\bar{\tau} = c (m_2/m_1)^{1/2}, \quad [20]$$

where c is a constant between 1 and 1.25. The ratio m_2/m_1 , measured for a mesh spacing $L_2 = 0.3$ cm, is 0.6 and furnishes the response factors $\bar{\tau}_M = 0.775$ to 0.97 at the mesh frequency f_m . The MTF of the mesh is approximated by gaussian curves through these points, as shown in Fig. 27. The response of a 1000-per-inch mesh at $f = 100$ cycles/mm occurs on the normalized curves at $f/f_m = 2.54$ and is

* A reduction in the number of nodal points causes poor off-axis performance (shading) and an increase to 5 nodal points results in S distortion.

$\bar{r}_{100} = 20$ to 35%, which increases to 48 to 63% for a 1500-per-inch mesh. The increase is traded for a lower mesh transmission that requires increased beam-current density. The MTF is specified for the mesh spacing $L_2 = 0.3$ cm. Smaller spacings increase the MTF, but move the mesh closer to the beam focus which can cause mesh shadow or visible interference patterns.

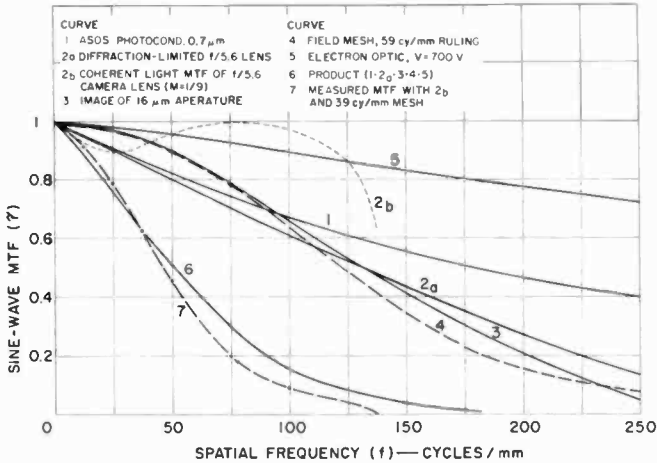


Fig. 28—Design objectives for MTF's of high-resolution camera (curves 1 through 6) and measured modulation-transfer function of high-resolution $4\frac{1}{2}$ -inch return-beam vidicon in camera, curve 7.

Overall Camera MTF's

The MTF's of the five significant camera components, which represent the design objective for a resolving power of 100 cycles/mm are shown in Fig. 28. It is evident that the read-out electron optic is the best component, and that the remaining components control the camera performance. Curve 6 in Fig. 28 is the computed product MTF of the camera. An actual modulation transfer function (without lens) is shown by curve 7. The MTF is smaller because a coarser field mesh (39.4 cycles/mm and an 18- μ m aperture are used in the particular tube. Oscillograms of the modulation transfer taken with this tube in the Y direction (vertical) by a sampling circuit are shown in Fig. 29. The Y sampling excludes the amplifier stages, and coherent illumination of the test slide eliminated the lens.

The photograph shown in Fig. 30, taken from a high-definition picture monitor, was obtained by scanning a 0.2 cm² area of the photo-

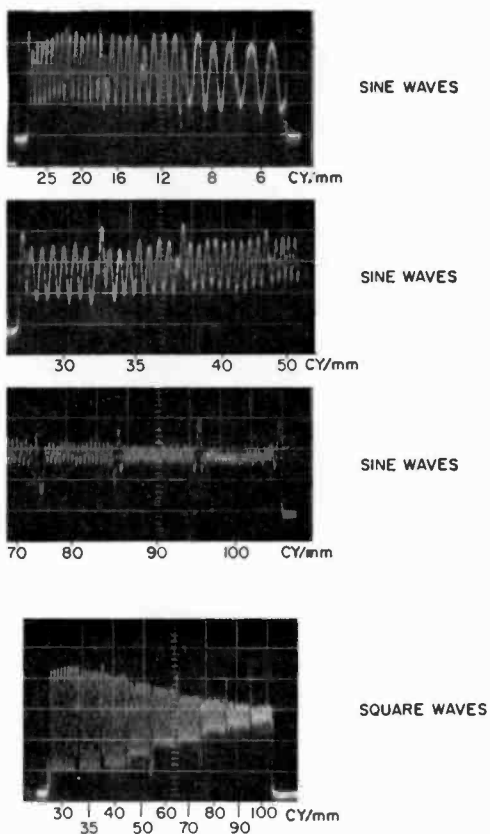


Fig. 29—Oscillograms of sampled response in the Y-direction.

conductor to show the 100 cycles/mm resolving power of the tube. The numbers in the circle are direct reading in cycles/mm. There is some interference from the 1000-cycles/inch field mesh, which should be finer. The field mesh can be imaged by focusing the reading beam on the mesh. A small section of the mesh image (1000-per-inch) seen on the picture monitor is reproduced in Fig. 31. The numerical example represents one combination of camera components. Different MTF's can obviously be obtained by variation of parameters such as the thickness (d) of the photoconductor, the mesh ruling, and the aperture diameter, depending upon the particular application.

Operational Characteristics of High-Definition Cameras

The technology required for a high-resolution television system differs substantially from that of commercial 500-line television systems. Al-

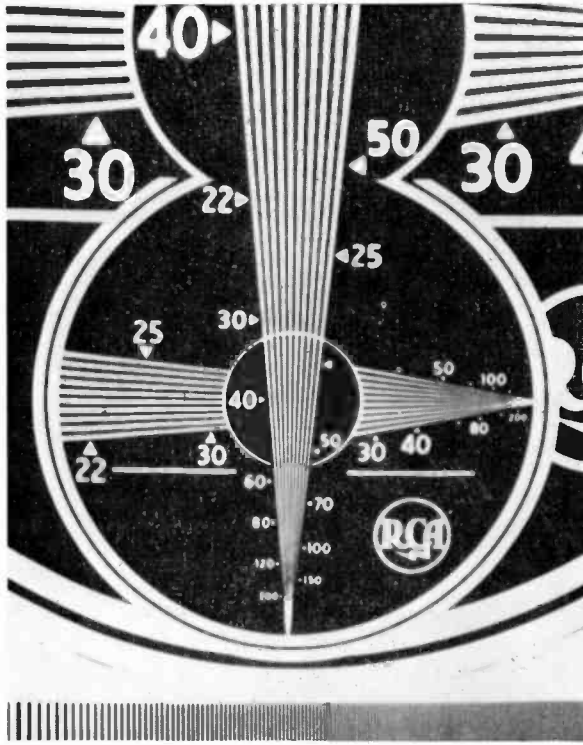


Fig. 30—Photograph showing 100-cycle/mm resolving power of experimental camera tube (incoherent light).

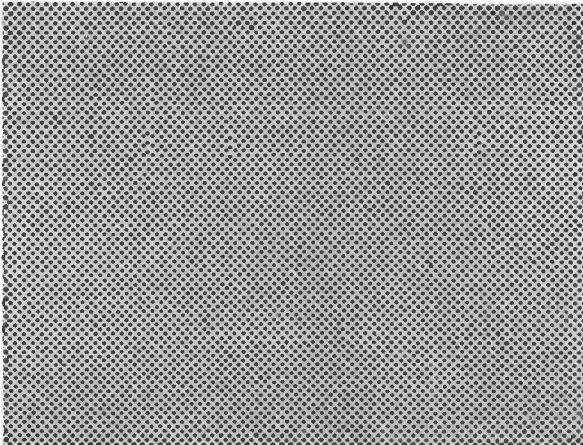


Fig. 31—Small section of 1000-line-per-inch field mesh reproduced by focusing the electron beam on the mesh.

though the basic principles of image sensing and video-signal development from stored charges are unchanged, second-order effects become first-order effects, and the simple theory is often inadequate when the number of elemental sampling areas is increased by more than 2 orders of magnitude; i.e., to 10^8 .

It follows immediately that adequate signal-to-noise ratios per element require an increase of the total storage capacitance of the sensor by a similar large factor. Substantial differences exist in the relations of scanning velocity, frame times, and the ratio t/C ; video pass bands for the read-out process may extend to 100 MHz. Uniformity of signals and MTF in the image format and freedom from blemishes demand smaller tolerances, a high precision of faceplates and other components in the electron optic, higher MTF's in the multiplier, and a far higher system stability than required for commercial cameras. The storage capacitance of the ASOS sensor, at present the best solution to operational requirements, is more than 600 times higher than that of a 1-inch vidicon, and the maximum beam current of high-resolution read guns having aperture diameters of 1 mil or less are much smaller than that obtainable from commercial electron guns. Signal potentials on the sensor surface are smaller, and residual signals and second-order effects become prominent and require special attention.

General System Characteristics

System stability—The small diameter of the reading beam and high target capacitance of the $4\frac{1}{2}$ -inch return-beam vidicon place special requirements on the system parameters. The beam diameter at the 2-by-2-inch storage surface is smaller than $1/2000$ of the image format. As a result, scanning rasters that contain fewer than 2000 lines leave unscanned interline charges on the storage surface. Such charges reduce the signal output and can cause picture shading or video-signal instabilities unless the raster-line spacing is very uniform and stable. These effects are not noticed when the beam is defocused by deflection "wobble" caused by noise. A 1000-line raster can, therefore, be used to test the stability of the vertical-deflection system. Instability in a 6,000- to 10,000-line raster can be detected only by its integrating effect on vertical resolution. The deflection current, therefore, should have a peak-to-peak signal to peak-to-peak noise ratio greater than 86 dB (100 dB has been realized). This requirement applies also to the line-deflection and timing circuits and to all power supplies involved, including the camera focusing system, and especially to isolation

against power-source variations or transients, which should be 0.001% or less. Camera and monitor must be shielded to prevent deflection modulation by power-line fields.

Detail Flicker—A second effect, seldom noticed in commercial television systems, is the presence of detail flicker in fast-scan visual displays on medium-persistence phosphor screens with interlaced fields, particularly for interlace ratios higher than 2 to 1 and field frequencies less than 60 Hz. Detail flicker occurs at frame-frequency rates and is caused by the high MTF of the camera, which develops high-amplitude signals at contours or other small detail contained within the width of one scanning line. The flicker disappears when the camera tube beam is large or defocused, but it cannot be suppressed by defocusing of the display tube. Detail flicker, therefore, is an indicator of sharp camera focus (optical and electrical). It can be eliminated by the use of long-persistence phosphors.

Frequency Range of Video System—The pass band of the video system is obviously a limiting factor in a direct visual display. It was increased twice during the development of the high-resolution system. The present video test system is completely solid state with a maximum pass band of 100 MHz. The preamplifier that follows the electron multiplier uses bipolar transistors in a cascode configuration and has an equivalent noise current of 79 nA and a noise factor of 0.1 dB for normal 10- μ A multiplier signals. The processing amplifier has a flat pass band to 120 MHz, and the single-stage cascode drive circuit for the display cathode-ray tube can deliver 40-volt signals and maintain constant beam modulation to 100 MHz. The video gain is continuously adjustable (to zero) by a differential stage in the preamplifier, which contains aperture correction circuits to compensate for the decreased multiplier gain of the camera tube at 100 MHz. Phase-corrected filters are provided to limit the pass band when desired. The 100-MHz video system is completely stable and free of interfering-signal pickup at the maximum over-all gain, which is 100 dB at 100 MHz.

Camera Operating Modes

Continuous Exposure Read-Out—The high-definition vidicon can be operated in the continuous-exposure read-out mode used in commercial television systems. This mode is feasible only for stationary subjects because the storage capacitance of the ASOS photoconductor is very high (0.4 μ F), partly because of the large format, which causes a very

long capacitive lag. The signal decay is longer than the value computed for a pure capacitance, and traces of image information remain after several minutes of continuous read-out following an exposure. Image charges can, however, be erased almost instantly by a uniform high-intensity light-flash exposure of the target (from small lamps between lens and target) which shorts out the photoconductor and raises the surface potential to the positive value of the external polarizing voltage E_T . Before a new exposure, the photoconductor is recharged to polarizing potential by scanning with the electron beam, which drives the surface down to cathode potential. This "prepare time" T_p is a function of the prepare current I_p , as explained later.

The continuous-exposure read-out mode with fast scanning rates is very useful for many purposes because it permits a direct observation of the image on a high-resolution cathode-ray-tube monitor. The resolving power of the camera can be observed by reading out a small section of the stored image by underscanning the photoconductor, as shown by Fig. 30. The effective conversion efficiency of this read-out mode is 100% because equilibrium requires that charge and discharge currents be equal. The frame time can be varied over a wide range with little effect on the MTF of the camera, as illustrated by the oscillograms shown in Fig. 32, provided the exposure does not exceed values that demand excessive beam currents.

Single-Exposure Read-Out—As in a photographic camera, exposure and signal read-out are two separate events in a high-definition television camera. The signal can be read out at either slow or fast scan rates. A slow-scan, single-frame read-out is used to reduce the bandwidth required for full definition in the format. A high-definition electron-beam or laser-beam recorder must then be used to record an image on photographic film. The resolution in fast-scan read-outs is limited by the available frequency channel.

Residual charges that remain after the read-out are removed by a high-intensity erase exposure. The discharged photoconductor is then repolarized in preparation for a new exposure. The insertion of an erase-prepare cycle permits control of potentials during signal read-out to achieve an optimum signal-development process.

Sensor Characteristics

Dielectric Transients in Photoconductors—The ASOS photoconductor used in high-definition return-beam vidicons has a nonuniform dielectric (in depth) which results in a dielectric delay during charge

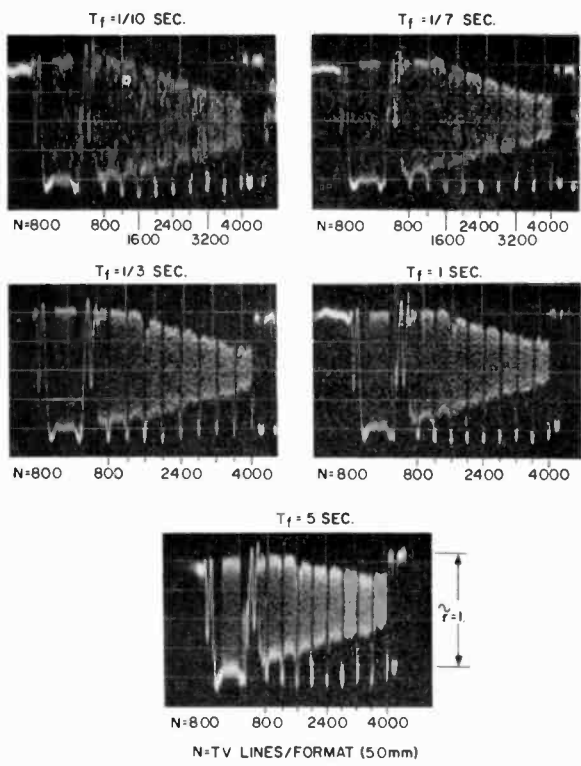


Fig. 32—Sampled square-wave “vertical” response of 4½-inch camera (full format) at various frame rates. Noncoherent illumination, f:8 lens; $I_s = 100$ nA; 19.0- μ m gun aperture; mesh, 72 by 16 cycles/mm.

from an external source. The external circuits that control polarization and read-out must be designed to compensate for the dielectric transients that occur in the photoconductor. Fig. 33 shows a simple model that represents the dielectric delay in a double-layer dielectric, of which one layer is a substantially perfect insulator and the other layer is semiconducting. The charge Q is stored in the nearly perfect dielectric C_1 , and the semiconducting layer C_2 is empty. Photoconduction caused by an exposure (simulated by the closing of switch S_1) reduces the charge in layer C_1 with a short (0.05-second) photoconductive delay. The change in potential ($\Delta V = \Delta Q / C_1$) is smaller than expected from a measurement of the total series capacitance C (for an ASOS photoconductor, $C_1 / C \approx 2$).

During the extremely short interval that the reading beam makes contact with an elemental capacitance, the effective capacitance is the

series capacitance C (the shunt resistances R_1 and R_2 are large). When a displacement current is drawn through the two dielectrics, charges are trapped in the previously empty dielectric (semiconducting layer C_2). These charges cause a polarization that inhibits a complete charge of layer C_1 during polarization, or read-out, even though the beam may have connected the vacuum side of the photoconductor to the cathode potential. After the beam has passed a photoconductive element, the trapped charges migrate back to layer C_1 , and the surface

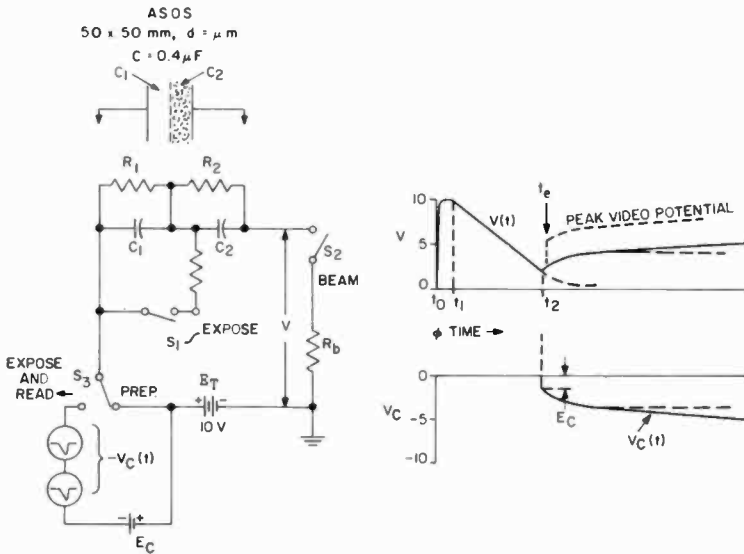


Fig. 33—Equivalent circuit for compensation of dielectric transients in photoconductors.

potential rises to a more positive value. This action can be simulated with respect to the surface potential by the equivalent circuit shown in Fig. 33. In this circuit, R_1 represents the dark resistance of the photoconductor, R_b represents the beam resistance, R_2C_2 is the dielectric time constant, and switch S_2 simulates the beam contact with the photoconductor.

The equivalent circuit illustrates the potential changes that occur during an erase-prepare-expose-read cycle. Switch S_1 is briefly closed to simulate the removal of residual charges in layer C_1 during erase exposure. Switch S_2 is closed at time t_2 , the start of the "prepare" interval, to polarize the photoconductor. Both C_1 and C_2 begin to charge in series through the beam resistance R_b , and the surface

potential V , which is initially equal to the polarizing voltage E_T , decreases at a constant rate. If it is assumed that the prepare interval terminates at time t_2 (at which time, the potential V has decreased to 2 volts), the potential across the capacitance C_1 may be 6 volts and, because of the lower shunt resistance R_2 , the potential across the capacitance C_2 may be 2 volts. The potential across capacitance C_2 decays to approximately zero in about 5 seconds,* and the surface potential V , resultingly, rises exponentially during this period to about 4 volts, as indicated by the solid-line curve in Fig. 33. If an image exposure occurs shortly after time t_2 , the curve of the peak video potential (dashed line) is superimposed on that of the black-level potential V (solid line). The potential V continues to rise slowly beyond the dielectric-delay interval because of the dark conductivity of C_1 . When read-out is started after an exposure, therefore, the black-level potential is too positive and drifts, unless some method of compensation is provided. This compensation is provided by a control voltage $-V_c(t)$ inserted (by switch S_3 in the equivalent-circuit model) in series with the target at time t_2 . The control voltage contains a dc component $-E_c$ and the outputs of two simple time-function (RC) generators that match the amplitudes and time constants of the photoconductor transients. The black level, therefore, remains constant and is independent of read-out delay and read-out time.

Polarizing Potential and Quantum Efficiency—The quantum efficiency ϵ of the photoconductor is a function of the polarizing potential V_p , as shown in Fig. 34. The polarizing potential before an exposure (V_{p0}) is determined by the charge introduced into the photoconductor by the prepare current I_p during the prepare interval t_p , which can be approximated as

$$t_p \approx C_1 V_{p0} / I_p, \quad [21]$$

where $C_1 \approx 2C$ is the effective storage capacitance of the photoconductor.

For the capacitance ($C_1 = 0.8 \mu\text{F}$) of a 50×50 -mm ASOS photoconductor and a mean prepare current I_p of $0.8 \mu\text{A}$, a polarizing potential V_p of 10 volts requires a charging time t_p of 10 seconds. Large currents are difficult to obtain from small reading-gun apertures be-

* Actually, the trapped charges are not dissipated, but instead, migrate back to layer C_1 .

cause of the limitation in current density. A separate large-diameter prepare source is the best solution to minimize the time t_p .

The polarizing voltage E_T should not exceed the potential V_{p0} by more than 2 volts because the residual potential difference ($V_r = E_T - V_{p0}$) is equivalent to a pre-exposure and determines the noise level in the prepared target.

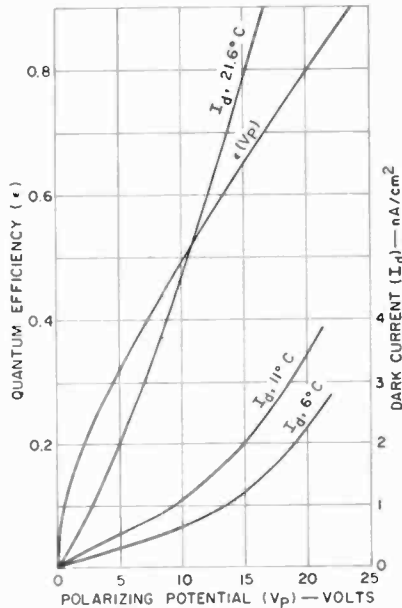


Fig. 34—Dark current and effective quantum efficiency of a 50-by-50-mm ASOS photoconductor.

The effective quantum efficiency of the photoconductor is a function of exposure because the potential change V_E that results from an exposure subtracts from the polarizing potential V_{p0} .

Dark Current—Peak target currents may vary from a few nA to 200 nA, depending upon the scanning velocity and exposure. The dark current of the photoconductor, therefore, should be very small to reduce dark-current charges and noise. Moderate cooling of the ASOS photoconductor is essential and very effective for this purpose, as shown in Fig. 34. Nevertheless, the dark-current charge of the photoconductor may be larger than the signal charge produced by low exposures. This condition requires an increase in beam current which, in turn, causes

an increase in the noise. The erase-prepare cycle, however, permits insertion of a read-out threshold potential V_o (by adjustment of the dc component $(-E_c)$ of the control voltage) in series with the photoconductor, as shown in Fig. 33. This threshold voltage permits read-out of only the video portion of the charge potential and blocks read-out of charges that result from residual potentials, dark current, and the haze of low-contrast images in the photoconductor. (These charges are removed by the erase exposure.) The use of the threshold potential restores a high image-signal contrast and minimizes the beam current, which is the predominant noise source.

Signal Read-Out Characteristics

Signal Read-Out by Electron Beams—The beam current accepted by a perfect collector is a function of collector potential and the electron energy spread in the beam. Theoretically, the slope of the voltage-current characteristics can be expressed, in terms of cathode or emitter temperature (in semilog coordinates), as follows:

$$\frac{d \log I_c}{dV} = \frac{5030}{T_k}, \quad [22]$$

where T_k is the emitter (or cathode) temperature in degrees Kelvin.

Photoconductors, or other storage surfaces are not perfect collectors, because electrons reflected at their surface at low potentials and secondary electrons generated in increasing numbers at higher potentials reduce the collector current. The two families of voltage-current functions shown in Fig. 35 are typical for a reflective target and practical electron guns that have apertures of 0.7 mil and 1 mil and a cathode temperature of 1100°K. The slope is considerably less than that of the theoretical characteristics shown for cathode temperatures T_k of 1000°K and 300°K (room temperature) in which a perfect collector and emitters that provide the required current density are assumed. A monochromatic beam source and a perfect collector are assumed for a fourth case in which the current rises with infinite slope at $V = 0$ to saturation values determined by a control in the electron gun.

In all cases, the charging current to a photoconductor element under beam contact is initially substantially constant until the element potential has decreased to the "knee" potential of the voltage-current characteristic. At potentials below the knee value, the current decreases

exponentially. The time functions computed for the four cases are shown in Fig. 36 and 37 by the normalized functions $V(t/C)$ and $I_e(t/C)$. The mean value of the current $I(V)$ read out by the beam is a function of target potential and the time-to-capacitance ratio t/C . This value is computed by integration of the current I_e within a selected interval t/C for different initial potentials with

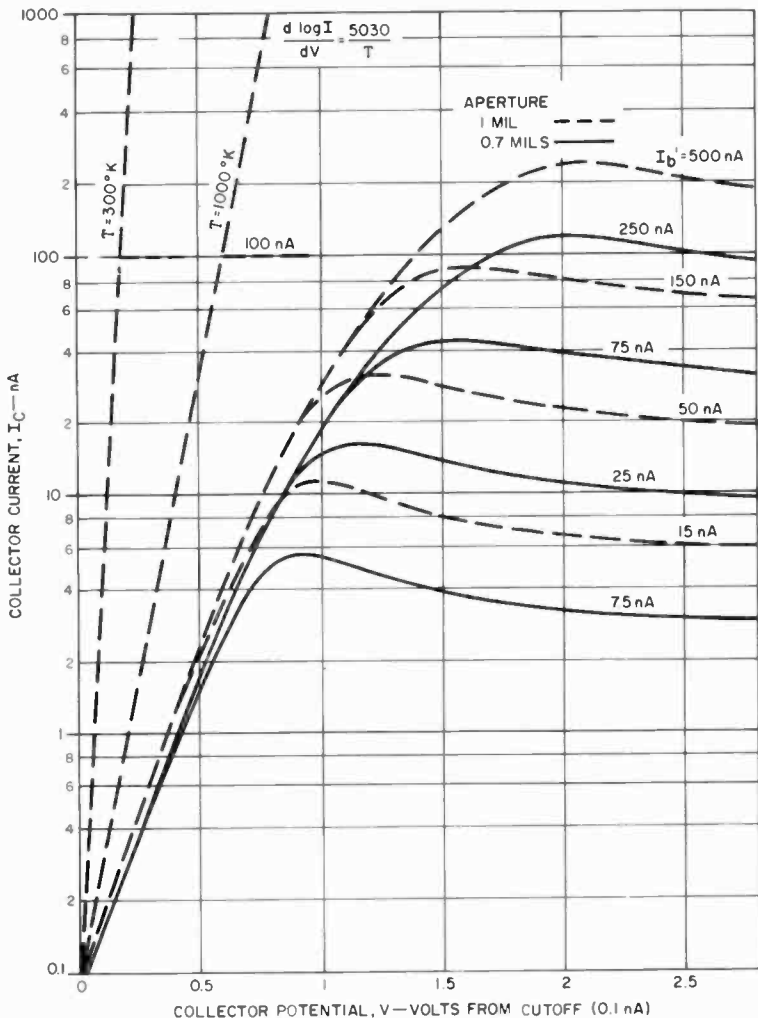


Fig. 35—Collector current as a function of collector potential for actual and theoretical electron beams.

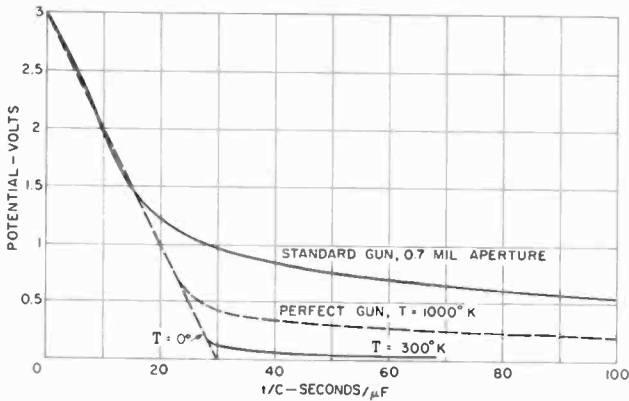


Fig. 36—Decay of surface potential under beam contact as function of the time-to-capacitance ratio t/C of a storage surface having no dielectric lag.

$$i = \Delta V / (t/C), \quad [23]$$

where ΔV is the potential drop ($V - V_t$) during the interval t/C .

The read-out characteristics are plotted in Fig. 38. The time-to-capacitance ratio is determined by the total target capacitance C and the total active read-out time t for one frame. Values for several types of camera tube and typical operating conditions are listed in Table IV.

The read-out characteristics, shown in Fig. 38, are "primary" char-

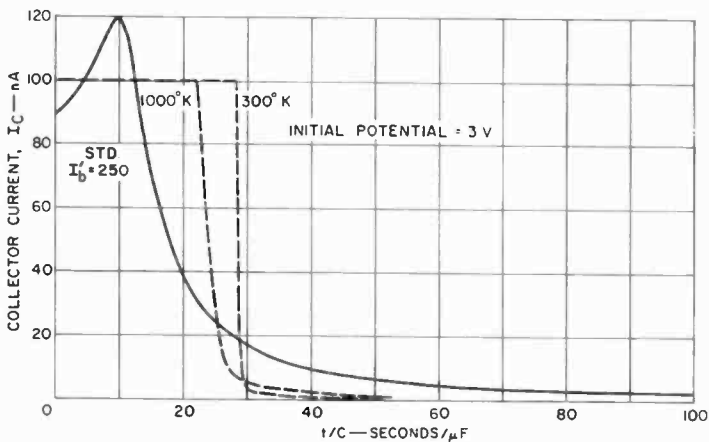


Fig. 37—Decay of current under beam contact as a function of the ratio t/C .

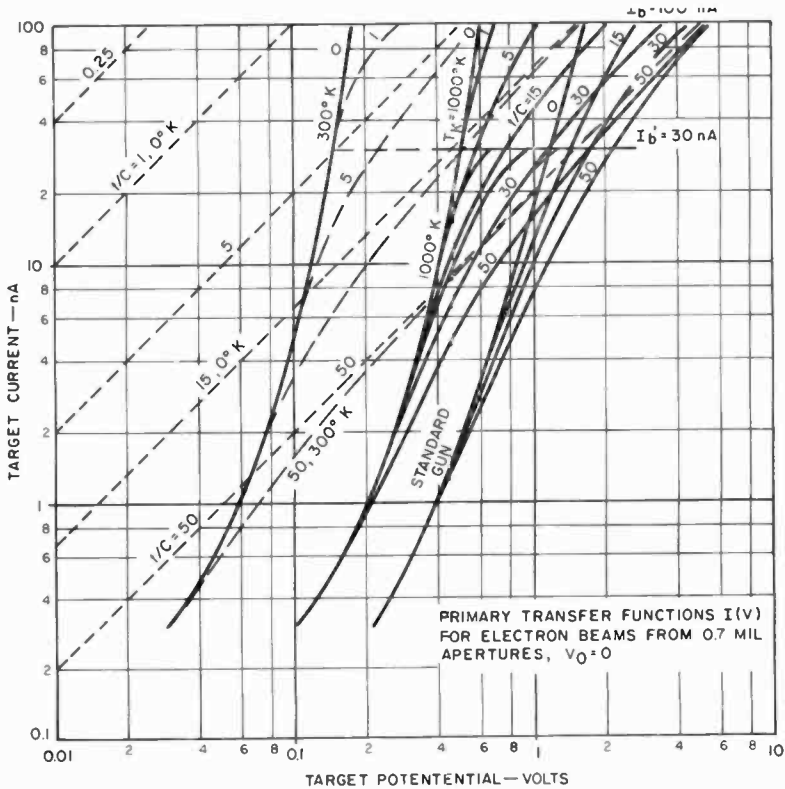


Fig. 38—Primary read-out functions $I(V)$ for actual and theoretical electron beams.

Table IV— t/C Values and Typical Operating Conditions for Several Types of Camera Tubes

Camera Tube	t (sec)	C	t/C (sec/ μf)	Read-out
3 inch image orthicon	1/30	275 pf	120	Std. TV
1 inch vidicon	1/30	1250 pf	26.7	Std. TV
High definition 2 inch return-beam vidicon	1/10	0.1 μf	1.0	fast scan
High definition 2 inch return-beam vidicon	5.	0.1 μf	50	slow scan
High-definition 4½ inch return-beam vidicon	1/10	0.4 μf	0.25	fast scan
High definition 4½ inch return-beam vidicon	6	0.4 μf	15	slow scan
High definition 4½ inch return-beam vidicon	10	0.4 μf	25	slow scan
Plumbicon	1/30	600 pf	56	Std. TV

acteristics for the total current read-out from the target potential V , which is measured from current cutoff. The current I , in general, may be expressed as

$$I = I_s + I_o, \quad [24]$$

where I_s is the video signal current and I_o is the current read out from the black-level bias potential V_o caused by the haze (V_{\min}) of low-contrast subjects, dark-current charges (V_d), residual potentials (V_r) from a prepare cycle, and a control potential $-V_c(t)$, which can be inserted in the single exposure-read-erase mode.

In the *continuous-exposure mode*, the black-level potential is given by

$$V_o = V_d + V_{\min}. \quad [25]$$

For high-contrast objects ($V_{\min} = 0$), the current I_o equals the steady dark-current value I_d . The equilibrium potential $V_o = V_d$ can be read on the appropriate t/C curve, shown in Fig. 38, for the current $I = I_d$. Similarly, the total target potential with an exposure is an equilibrium potential located on the t/C curve at the total current $I = I_s + I_d$.

It is evident from Fig. 38 that the four functions for $t/C = 50$ (typical for standard television camera-tube operation) converge towards a single curve for currents I greater than 100 nA. This condition indicates that the read-out efficiency of a *standard electron gun* is 100% for currents I greater than 100 nA and cannot be improved. The read-out efficiency of the normal electron beam decreases for smaller currents and potentials. It is determined by the ratio of the currents read out at a given potential with the standard gun to the current read out with the "ideal" gun ($T_k = 0^\circ\text{K}$), or by the ratio of the charge potentials required for a given current.

The read-out efficiency at low potentials can be improved substantially by addition of a positive-bias potential V_o (which can be generated by a dark current, a bias light, or by a control potential) to the standard-gun characteristic. The operating characteristic for $t/C = 50$ and a potential $V_o = +0.7$ V is shown in Fig. 39. This characteristic is constructed by subtraction of 0.7 V from the primary characteristic $I(V)$ at all current levels. This subtraction yields the function $I(V_s)$ and a current $I_o = 3.5$ nA. The signal current $I_s = I - I_o$ is shown by the function $I_s(V_s)$ obtained operationally by raising the clipping level in the black-level setter to subtract current I_o . The large gain in read-out efficiency is obvious from the close approach to the

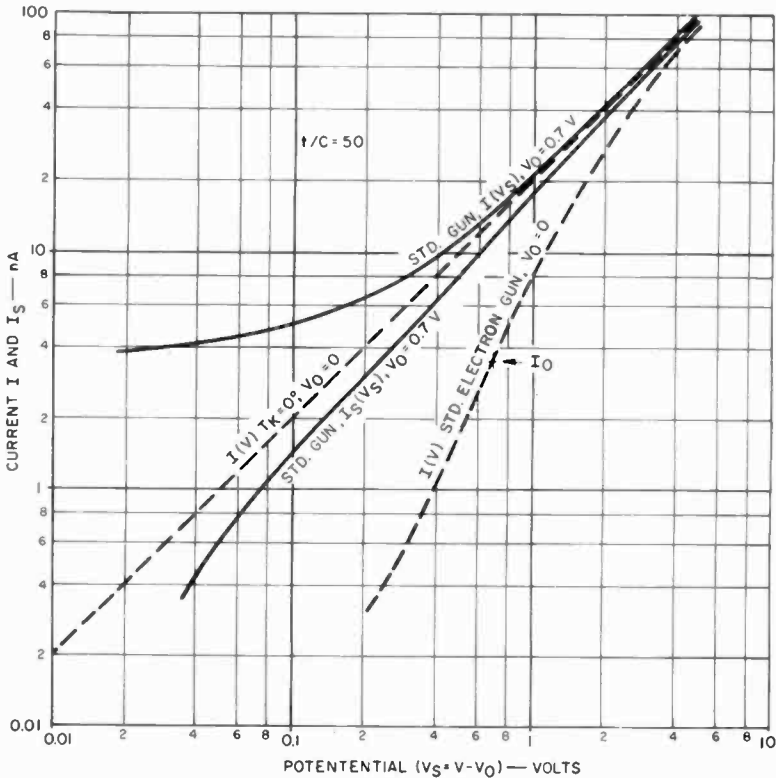


Fig. 39—Effect of read-out bias (V_0) on the read-out efficiency for the time-to-capacitance ratio $t/C = 50$ seconds/ μ F.

ideal function $I(V)$ for $T_k = 0^\circ\text{K}$, although signal-to-noise ratios are decreased at low currents by the factor $(I_s/I)^{1/2}$.

A read-out bias, however, cannot correct the very low read-out efficiency of a standard electron gun at low t/C ratios (i.e., high capacitance, fast scan), because the primary curves do not converge sufficiently at reasonable exposures, and progressively higher efficiencies are obtainable from the theoretical electron guns for fast-scan read-out of high-capacitance photoconductors as illustrated by Fig. 40. It should be noted that the potential is reduced to millivolts for $T_k = 0^\circ\text{K}$.

It can be concluded that the monochromatic electron gun can eliminate capacitive lag at fast scan rates, but it cannot eliminate the loss of read-out efficiency and dielectric delay in an imperfect capacitance, such as the ASOS photoconductor, nor does it improve the loss of beam modulation caused by electron reflection. The monochromatic

electron gun would be an ideal solution for continuous-exposure read-out from a high-capacitance sensor without dielectric lag, except for a mesh-imaging problem. The standard electron gun is adequate for a continuous-exposure read-out from low-capacitance sensors and for slow-scan read-outs with t/C ratios of 50 or larger. In fact, a good *standard* electron gun is necessary for the multiple-frame-read-out mode from a single exposure (discussed subsequently), which depends on a low read-out efficiency per picture frame and the slow exponential potential decay shown in Fig. 36.

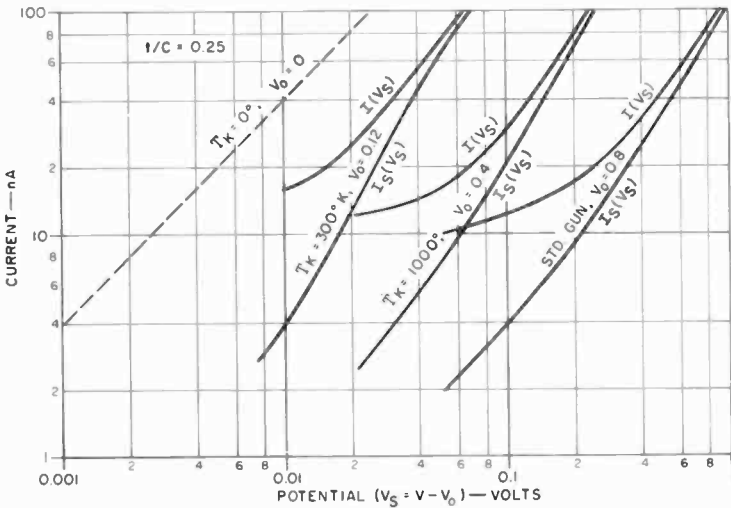


Fig. 40—Effect of read-out bias for $t/C = 0.25$ second/ μF .

Signal Decay and Read-Out Efficiency of an ASOS Photoconductor—

The dielectric delay of the ASOS photoconductor reduces the slow-scan read-out efficiency of the stored charge C_1V , as shown in Fig. 33, because electrons trapped in the series capacitance C_2 prevent a complete charge by the scanning beam. The potential drop during beam contact and recovery between successive beam contacts in a multiple-frame read-out of a single exposure is a function of frame time, as illustrated in Fig. 41 for a capacitance ratio $C/C_1 = 0.5$. A starting potential $V_{(0)}$ of 2 V is assumed. For the slow-scan time of 6 seconds ($t/C = 15$ seconds/ μF), the potential drops during beam contact to $V_c = 1.08$ V at $t/C = (t/C)_0 + 15 = 24.7$, as may be determined from Fig. 36. The potential read out, therefore, is $\Delta V' = 0.92$ V.

For the condition $C/C_1 = 0.5$, one half of $\Delta V'$ appears across each

series capacitance C_1 and C_2 , and the surface potential recovers to $V_t + 0.5\Delta V' = 1.54$ V after the dielectric delay (5 seconds), which is shorter than the frame time. The starting potential for the second-frame read-out, therefore, is 1.54 V, and the potential decays during successive frame times as shown in Fig. 41.

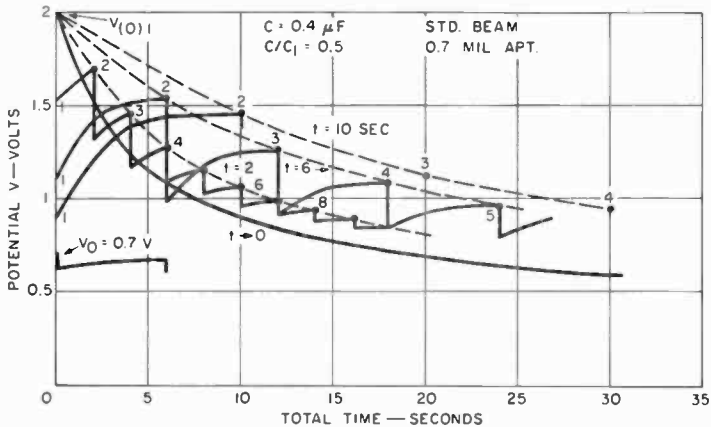


Fig. 41—Potential decay of storage surface with dielectric delay for various frame times after single exposure.

The read-out efficiency η_c is given by

$$\eta_c = \Delta V_s' (C/C_1) / V_{s(0)}, \quad [26]$$

For the first frame, $\eta_c = 0.46/2.0 = 0.23$. A read-out bias V_o of 0.7 V increases the initial potential to $V_{(0)} = 2.7$ V, and the potential drop $\Delta V'$ increases to 1.42 V. The signal potential read-out is the difference $\Delta V' - \Delta V'_o = 1.42 - 0.06 = 1.36$ V, where $\Delta V'_o$ is the black-level signal. The read-out bias V_o , therefore, increases the read-out efficiency η_c to $0.68/2 = 0.34$.

The recovery of potential between beam contacts is incomplete for fast-scan read-outs and disappears for $t/C = 0$, as shown in Fig. 41 by the decay functions computed for shorter read-out times.

The mean read-out current can be calculated from the expression $I = \Delta V/(t/C)$. The decay functions $I(t)$ are shown in Fig. 42. The current I remains constant during the frame time t when the potential is uniform in the format. It is evident that the decay of the signal current is slower for multiple-frame slow-scan read-outs than for fast-scan read-outs.

Actual measured decay functions (shown in Fig. 41) are in general agreement with computed values, but may vary for different operating conditions, because the equivalent circuit model is not an exact representation. There is evidence that the dielectric time constant introduced by electron trapping in the photoconductor is a function of the electron charges injected by the beam. It is observed that

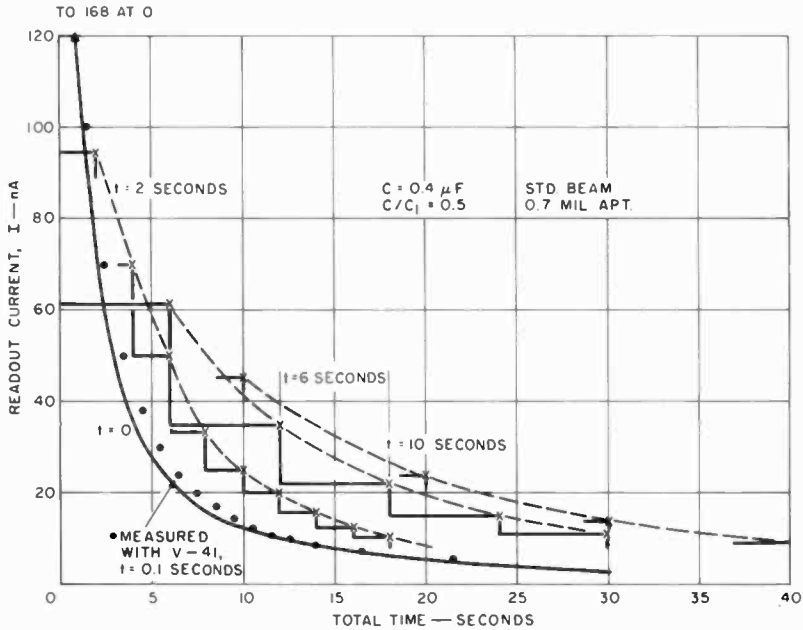


Fig. 42—Decay of signal current with dielectric lag as a function of frame time after single exposure.

signal read-out can be completely “blocked” by a large excess beam current, which does not affect stored charges. The target current decreases to zero and the return beam carries no modulation. Read-out can be blocked by excess beam current with the lens capped for several minutes, and resumed with little loss of signal when the beam current is reduced to a normal value. Excess beam current, therefore, must be avoided, particularly during a multiple-frame read-out of decaying signals.

The efficiency of a fast-scan read-out with a normal electron gun is low, as indicated by the slow potential decay. The stored signal charge in the photoconductor, however, is very large and can provide adequate

signal-to-noise ratios for long observation times, as discussed subsequently.

Signal to Noise Ratios (SNR)—The predominant noise source in return-beam vidicons is the reading beam. For beam modulations that do not exceed 30%, the large-area signal-to-noise ratio SNR_o can be computed with good accuracy from the shot noise of the reading beam as follows:

$$\begin{aligned} SNR_o &= (3.12I_s\tau_m m_b \times 10^9/b\Delta f)^{1/2} \\ &= (62.5I_s\tau_m m_b t)^{1/2} \times 10^4/\bar{N}_e, \end{aligned} \quad [27]$$

where I_s = peak-to-peak target signal current in nA, $b = t/T_f$ = ratio of active reading time to frame time (blanking factor), τ_m = mesh transmittance (typically 0.5), m_b = beam-modulation factor (typically 0.25), t = active reading time per frame in seconds, Δf = frequency channel in Hz, and $\bar{N}_e = (N_x N_v)^{1/2}$ = equivalent pass band (television lines).

A slow-scan read-out of the full definition with a pass band \bar{N}_e of 10,000 lines in the active time t of 6 seconds, and a signal current I_s of 60 nA provides an SNR_o of 53. High-resolution films have signal-to-noise ratios SNR_o of 10 to 20, which indicate satisfactory performance with signal currents of 2 to 7 nA for this read-out time. A hard copy of the full format that contains the full definition requires a high-resolution recorder that has an MTF of 50 to 75% at 10,000 lines.

Fast-scan read-outs are limited to lower pass bands by the available frequency channel. For $\bar{N}_e = 2000$ and equal currents, the SNR values would increase by a factor of 5 and permit a decrease of the read-out time by a factor of 25 (i.e. to 0.24 second), which is too slow for a flicker-free image display on a standard television display tube. The signal currents, therefore, must have larger values or the phosphor decay time must be increased substantially to prevent flicker, as discussed in the following sections.

Single-Exposure Multiple-Frame Read-Out (without storage converter)

—This unusual and very useful operating mode derives from the high storage capacitance of the 50-by-50 mm photoconductor and the voltage-current characteristic of standard electron beams, which reduce the read-out efficiency from single exposures at fast-scan rates to small values. A good portion of this loss in efficiency can be recovered by image storage in a long-persistence phosphor, as discussed in the following section. The low conversion efficiency of a fast-scan read-out

provides a slowly destructive read-out of a large number of frames. For an initial signal current I_s of 90 nA at the start of a 20-frame-per-second read-out ($T_f = 0.05$, $b = 0.7$) and a resolution \bar{N}_c of 2000 lines, the initial signal-to-noise ratio SNR_o , computed from Eq. [27] is 25. The signal-to-noise ratio remains adequate when the beam current is controlled so that it decays in proportion to the signal to maintain a constant beam-modulation factor. The signal amplitude can be held constant by increasing the multiplier gain. These controls are accomplished by use of simple resistance-capacitance circuits, which are inserted at the start of a multiple-frame read-out. The SNR for the above example is 6.45 at the end of a 20-second read-out when the current I_s has decayed to 6 nA. The resolution remains bandwidth-limited because of the high MTF of the camera. Aside from the substantial improvement of the SNR, beam-current control reduces spurious background shading caused by mesh or multiplier nonuniformities in direct proportion to the beam current, to maintain a "clean" image.

Noise Reduction by Multiple-Frame Storage—The signal-to-noise ratio and useful display time of a multiple-frame read-out can be improved substantially by integration of image signals and noise in an image-storage surface because the noise in the video signal of consecutive frames is uncorrelated.⁵ Image storage can be accomplished by a multiple-frame exposure of a photographic film or, for a direct display, by a multiple electron-beam exposure of a long-decay phosphor screen in the display tube. It is self evident that a high stability of the read-out and display rasters is required within the storage time to prevent misregister and deterioration of the spatial-frequency spectrum of high-definition images.

Noise Reduction in Long-Persistence Phosphors—For a uniform excitation of a cathode-ray-tube phosphor by a constant beam current, the excitation of a small sampling area occurs in discrete time increments $\Delta t = T_f$ because of the scanning process. For a total decay time $t_d > T_f$, the mean signal intensity at a time t_o of observation is given by

$$I_s = i_{so} \left| \sum_{t=t_o}^{t_o+nT_f} (i/i_o)_t \right|, \quad [28]$$

where t_o may have a value between zero and T_f , and i_{so} is the initial intensity of excitation. When the beam current is modulated by noise

having an rms value $i_{n(o)}$, the noise in successive frame times is uncorrelated, and the total rms noise is

$$I_n = i_{n(o)} \left| \sum_{t=t_0}^{t_0+nT_f} (i/i_0)_t \right|^2 \Big|^{1/2}. \quad [29]$$

The signal to noise ratio then becomes

$$\text{SNR} = I_s/I_n = \text{SNR}_0 \sum (i/i_0)_t \Big| \sum (i/i_0)_t^2 \Big|^{1/2}, \quad [30]$$

where $\text{SNR}_0 = i_{s0}/i_{n0}$ = the SNR of a single-frame excitation. The sums are evaluated according to Eqs. [28] and [29].

Table V—Numerical Evaluation of SNR for the Decay Functions Shown in Fig. 38.

Function in Fig. 2	t_d/t_f	$t_0 = 0.5 t_f$		SNR	$F_{n(e)}$	F_s
		$\Sigma (i/i_0)$	$(\Sigma (i/i_0)^2)^{1/2}$			
1	0.7	0.03	0.03	1.0 SNR ₀	1.0	0.03
2	7.0	1.59	$(0.7617)^{1/2}$	1.82SNR ₀	3.3	1.59
3	4.0	2.69	$(1.95)^{1/2}$	1.85SNR ₀	3.84	2.69
4	4.0	4.0	$(4)^{1/2}$	2.0 SNR ₀	4.0	4.0
		$t_0 = 0$		SNR		
		Σi	$(\Sigma i^2)^{1/2}$			
1	0.7	1.0	1.0	1.0 SNR ₀		
2	7.0	2.12	$(1.366)^{1/2}$	1.815SNR ₀		
3	4.0	3.09	$(2.5)^{1/2}$	1.96 SNR ₀		
4	4.0	4.0	$4^{1/2}$	2.0 SNR ₀		

A numerical evaluation is given in Table V for four different decay functions $(i/i_0)_t$, illustrated by Fig. 43, in which the summation points are indicated for $t_0 = 0.5T_f$. Function 1 represents the case for a total decay time t_d , shorter than T_f , in which no integration occurs. Function 4 represents a perfect storage surface exposed by an electron beam or by light from a fast-decay phosphor for an exposure time of four frames. In this case, SNR₀ is improved by the square root of the number of stored frames. A noise equivalent storage factor $F_{n(e)}$ may then be defined as the noise equivalent number of integrated frames,

$$F_{n(s)} = (\text{SNR}/\text{SNR}_0)^2. \quad [31]$$

The signal-storage factor is defined by the relative signal increase

$$F_s = \frac{1}{i_0} \sum_{t_0}^{t_0+nT_f} (i/i_0)_t. \quad [32]$$

Table V shows that a similar noise reduction (for high-values of $F_{n(s)}$) can be obtained with decay functions (curve 2 or 3 in Fig. 43) that have a relatively poor signal storage F_s .

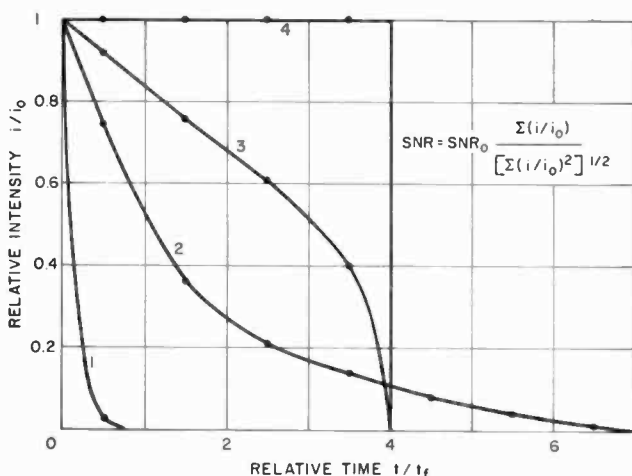


Fig. 43—Decay functions of perfect and imperfect storage surfaces.

The evaluation of a pure exponential decay function of the form

$$i/i_0 = \exp - (t/\tau), \quad [33]$$

where τ = time constant, is of interest and is given in Table VI. For large (τ/T_f) ratios, the sums in Eq. [30] can be replaced by integrals that yield

$$\text{SNR} = \text{SNR}_0 (2\tau/T_f)^{1/2}. \quad [34]$$

Inspection of Table VI shows that this equation is a good approximation for ratios $(\tau/T_f) \geq 1$.

The build-up and decay functions of an actual long-persistence

Table VI—Noise Reduction Factor $\Sigma i / (\Sigma i^2)^{1/2}$ for Exponential Decay Functions

τ/t_f	$t_0 = 0$	$\Sigma i / (\Sigma i^2)^{1/2}$ t_f	$0.5 t_f$	$(2\tau/t_f)^{1/2}$
10	4.52	4.44	4.48	4.48
5	3.16	3.15	3.155	3.16
2	2.018	2.022	2.02	2.0
1	1.47	1.468	1.469	1.414
2/3	1.252	1.24	1.25	1.155

phosphor, P-38 or VC4*, are shown in Fig. 44. The functions were measured with a photomultiplier on a small section of a single-line trace of a 500-line raster of 60 fields per second. The build-up is exponential, but the decay has a longer than exponential tail. The time constant is $\tau \approx 0.47$ second.

Application to High-Resolution Systems—The signal storage in the P-38 or VC4 phosphor is adequate for a perfectly flicker-free image display with 30 fields per second, interlaced 3 to 1; i.e., a frame time $T_f = 0.1$ second for which a 100-MHz pass band can accommodate a 3000-line raster ($N_v = 3000$) and a horizontal resolution N_H of 3800 lines in a square format. If a target signal current I_s of 90 nA with a T_f of 0.1 second is assumed, the video signal-to-noise ratio SNR_o , com-

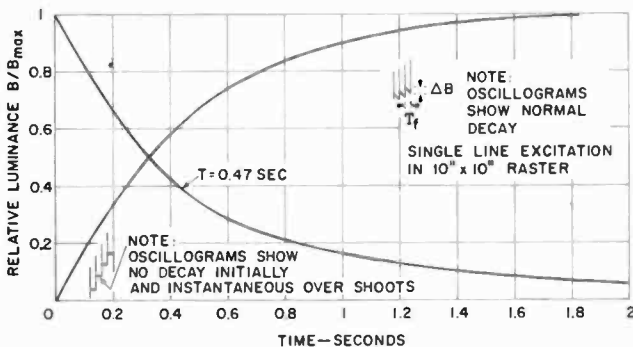


Fig. 44—Build-up and decay characteristics of a long-persistence phosphor.

* Orange-yellow fluoride phosphor.

puted from Eq. [27] for $T_f = 100$ MHz, is 21.6. The noise improvement factor SNR/SNR_0 computed from Eq. [34] for $\tau = 0.47$ is 3.07. The value computed from the actual curve shown in Fig. 44 is 3.76. The SNR in the displayed image, therefore, is $21.6(3.76) = 81$.

The SNR for a signal current I_s of 90 nA, read out from the photoconductor by a noise-free beam (computed with $m_b = 1$ in Eq. [27]) in $T_f = 0.1$ second is 43.2. The noise integration in the phosphor, therefore, provides a much higher SNR than a noise-free reading beam. This condition is not impossible, because the noise in the photoconductor signals is nearly uncorrelated in successive frame read-outs because the total signal charge in the photoconductor is approximately $1/\eta_c = 100$ times larger than the signal read-out in one frame time. The same conditions apply to the equilibrium state of a continuous-exposure read-out of a stationary subject. The actual read-out efficiency is low, but the charge in the photoconductor must build up to a value approximately 100 times larger than that read out in T_f as a signal current to achieve equilibrium of signal input and output. This equilibrium results in an effective conversion efficiency of unity.

The ASOS sensor has a substantially perfect storage surface. Because the total signal charge for the example is larger by the factor of 100, the SNR of the stored charge ($\text{SNR}_q = 43.2\sqrt{100}$) is 432. This theoretical limit can be approached in the continuous-exposure mode by a multiple-frame integration in a storage surface.

It should be noted that the SNR_q in the photoconductor decreases slowly to zero at the end of the total signal decay time from a single exposure, because the stored image charge is decreased progressively by a multiple-frame read-out. The SNR of a phosphor image, however, remains constant during the luminance decay after cessation of

The noise integration by the long-persistence phosphor increases the useful display time to at least 1 minute, even when the scanned format in the camera is reduced to obtain an image magnification of 2 to 1 to observe finer detail.

An initial signal of 90 nA, from the full 50-by-50-mm format for example, decays to approximately 1 nA in 60 seconds (computed for $t/C \rightarrow 0$ and $C = 0.4 \mu\text{F}$), and provides an $\text{SNR}_{(60)}$ of 8.55 for a 100-MHz frequency channel with noise integration in a P-38 phosphor.

The calculation neglects possible effects in the dielectric that could contribute to a longer read-out, and demonstrates that the combination of a pure storage capacitance and a standard electron beam can provide a long read-out time. The long signal storage time requires a low

dark current obtainable by cooling the ASOS photoconductor. For $V_{po} = 8$ V and a photoconductor temperature of 6°C , the depolarization by the mean dark current (11.3 nA) is 1.7 V after 60 seconds.

Fig. 45 shows the virtually noise-free reproduction of an aerial photograph from a 9-by-9-inch paper print on the 17-inch cathode-ray-tube monitor. This reproduction is bandwidth limited to approximately



Fig. 45—Photograph of aerial 9-by-9-inch print reproduced on 17-inch monitor picture tube, bandwidth limited to 1800 lines.

1800 lines by a 60-MHz video pass band and is somewhat degraded by photographing the curved-screen image of the 17-inch picture tube. Figs. 46 and 47 show 9-by-9-mm sections of the same image obtained by underscanning (electronic zoom) of the camera image. All pictures were scanned with 1760 lines, interlaced 3 to 1 at 60 fields per second. A 140-MHz spot wobble is used on the monitor to eliminate visible line structure.

Noise Reduction and Storage Time of the Eye—The signal storage in a long-persistence phosphor provides a continuous image from the point-by-point excitation of a television scan and does not depend on the storage time of the eye. The short-decay sulfide phosphors used in commercial television systems have time constants much shorter than a field time, and high field and frame rates (60 fields, 30 frames



Fig. 46—Detail in 9-by-9-mm area read-out by underscanning.

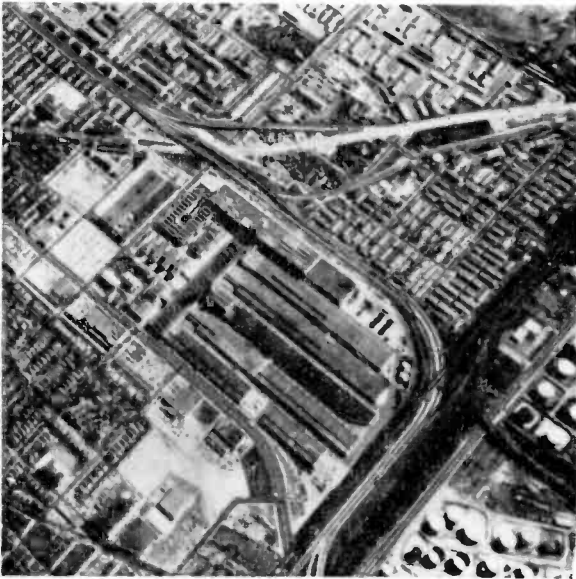


Fig. 47—Detail in 9-by-9-mm area read-out by underscanning.

per second, interlaced 2 to 1) are required to reduce image and line flicker to acceptable values because of the relatively short signal storage time of the eye. Flicker is visible in fine detail at normal luminance values, $B > 2$ foot-lamberts, when the camera tube has a high MTF at the raster line number ($N \approx 480$ lines) because detail within a line width produces signals repeating at the 30-cycle frame rate. This detail flicker cannot be eliminated by defocusing of the display.

In a recent experiment, a well-defined 1500-line raster of 15 fields per second, interlaced 3 to 1 was displayed with a high-resolution electron gun on a fast-decay phosphor to observe the storage characteristics of the eye. Spatial integration by the MTF of the eye was eliminated by observation of a section of the field with adequate magnification. The eye fails completely to integrate the three fields. Only one strongly flickering field, which travels downward because of the interlace, is visible. No trace of illumination from the remaining two fields is detectable in the interline (black) spaces of this field. It is concluded, therefore, that the decay function of the eye decreases to a small value in $1/15$ second and storage is certainly shorter than $2/15$ second, i.e., $t_d < 0.133$ second.

Table V shows that the longest noise equivalent storage time for a given value t_d is obtained with a decay function such as shown by curve 3 in Fig. 43. The noise equivalent storage time of the eye, therefore, is in the order of 0.1 second, which confirms the author's previous evaluation from Blackwell's data.⁴ It follows that the SNR_0 in standard television displays ($T_f = 1/30$ sec) is improved by a factor of $\sqrt{3}$.

Sensitivity

The full quantum efficiency of the present ASOS photoconductor is not realized in single-exposure read-outs because of capacitive and dielectric lag and because high polarizing potentials require a long prepare time with small reading-beam currents. The light exposure of the ASOS photoconductor for daylight is given in meter-candle-seconds by

$$E \approx 0.815 I_s T_f / (A \epsilon \eta_e), \quad [35]$$

where I_s is the target signal current in nA, T_f is the frame time in seconds, A is the area of photoconductor in mm^2 ($=2500 \text{ mm}^2$), ϵ is the

quantum efficiency, which is a function of polarizing voltage, and η_c is the conversion efficiency (a function of T_f and C).

The quantum efficiency ϵ , shown graphically in Fig. 34, was calculated by use of Eq. [35] from measurements of E and I_s , for $T_f = 0.1$ second in the continuous-exposure mode for which $\eta_c = 1$. (The luminance of the white-card test object was measured with a Weston luminance meter to compute E from the lens data.)

For a slow-scan read-out time of 6 seconds and a signal current of 60 nA, the read-out efficiency η_c is approximately 0.3. Operation with a polarizing potential $V_p = 8$ V ($\epsilon = 0.425$) yields the exposure $E \approx 0.92$ meter-candle-second.

A multiple-frame read-out of 10 frames per second that starts with a signal current I_s of 100 nA requires the exposure $E \approx 0.72$ meter-candle-second for $V_p = 8$ V because of the low read-out efficiency $\eta_c = 0.008$.

The exposure values for the continuous-exposure read-out mode are very much smaller because E is computed for $\eta_c = 1$.

Conclusions

The design of flat-field high-resolution electron optics and electron guns that provide small beam diameters for signal read-out from a high-capacitance ASOS photoconductor has increased the resolving power of the television camera to 10,000 lines in a 50-by-50-mm format. Aside from a slow-scan read-out for obtaining a permanent record of the high-resolution image by a photographic recording process, a direct-view display of high-definition images on a high-resolution picture tube is achieved without storage converter by a multiple-frame read-out from a single exposure.

Constant video signals and excellent signal-to-noise ratios are maintained by automatic read-out controls and noise integration in a long-persistence phosphor for observation times in the order of 1 minute.

Acknowledgment

The development of high-definition camera tubes and electron optics was sponsored by the Air Force Avionics Laboratory, Wright-Patterson Air Force Base, Ohio, under Contract AF33(615)-5347. The camera tubes were constructed at RCA Lancaster under the supervision and support of A. L. Morehead and C. B. Johnson. E. G. Ramberg of RCA Laboratories, Princeton, has been most helpful in the mathematical

formulation of the energy spread in electron sources. The camera and 100-MHz test system were built at RCA Harrison with the able assistance of O. H. Schade, Jr. and C. Trushell.

References

- ¹ I. M. Krittman, Final Report, USAF Contract No. AF33(657)-7939.
- ² A. Rose, "The Relative Sensitivities of Television Pickup Tubes, Photographic Film, and the Human Eye," *Proc. I.R.E.*, Vol. 30, p. 293, June 1942.
- ³ P. K. Weimer and A. Rose, "The Motion of Electrons Subject to Forces Transverse to a Uniform Magnetic Field," *Proc. I.R.E.*, Vol. 35, p. 1273, Nov. 1947.
- ⁴ A. Rose, "Electron Optics of Cylindrical Electric and Magnetic Fields," *Proc. I.R.E.*, Vol. 28, p. 30, Jan. 1940.
- ⁵ D. O. North, "An Analysis of the Factors which Determine Signal/Noise Discrimination in Pulsed-Carrier Systems," *Proc. IEEE*, Vol. 51, p. 1016, July 1963.

Stable Solid-State Vertical Deflection for High-Definition Television Systems

Otto H. Shade, Jr., RCA Electronic Components, Harrison, N.J.

Abstract—Vertical-scanning instabilities in return-beam vidicon cameras for high-definition television applications can cause serious masking of picture detail and loss of resolution. Permissible deflection instabilities are a fraction of the scanning-beam diameter; excursions considerably less than 10 percent are detectable in operation with a well-focused beam. Solid-state deflection systems deliver excellent performance when particular attention is devoted to the design of a linear waveform generator and the stable, low-noise amplifier stages that follow it. Peak-to-peak signal-to-noise ratios exceeding 100 dB have been obtained at the amplifier output with a generated waveform nonlinearity of 0.1 percent or less. Measurement and calculations of Johnson noise show that source impedance and collector current level at the amplifier input are of major importance. In addition, power-supply stability requirements are demanding; line isolation and noise and ripple rejection approach the limitations of commercial equipment. Schematic diagrams and oscilloscope test waveforms of amplifiers and a suitable power supply are included and described.

Introduction

The successful display of a high-definition television picture depends upon the performance of many components. This paper is concerned with one aspect of producing good picture quality—the achievement of stable vertical deflection for the television camera. The television chain for which the circuitry was developed has been described by O. H. Shade, Sr.;^{1,2} it has recently been extended in video bandwidth from 60 to 100 MHz. The developmental 2- and 4.5-inch return-beam vidicons are provided by RCA Electronic Components in Lancaster, Pennsylvania. It is possible to display high-quality 4000-line pictures with this system.

In the following sections, some of the degradations in picture quality caused by vertical-deflection instabilities are presented. The development of solid-state deflection circuits is described, along with their

performance limitations. Designs for a differential-configuration amplifier and a passive-feedback-network amplifier are presented in detail, with oscilloscope test waveforms for the latter type.

Power supplies must have good load regulation and excellent isolation from the power line, as well as very low noise. It has been both expedient and informative to develop supplies along with the amplifiers for better determination of performance needs. Because some requirements approach the limitations of commercial equipment, the design for a suitable supply is also described briefly.

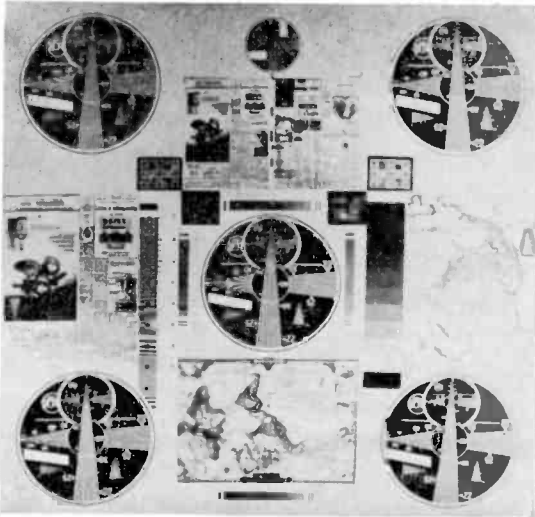


Fig. 1—500-line noninterlaced 10×10 -inch display.

Display Disturbances Caused by Vertical Instabilities in the Vidicon Beam

It is not possible to describe fully the transient visual effects caused by vertical-scanning instabilities with "still" photography. However, a record of the magnitude of some commonly encountered disturbances and the resulting masking of detail can be made. The phenomena to be described occur in high-resolution return-beam vidicons when the scanning-beam size is smaller than the raster pitch and the beam is in good focus. If the vidicon beam is defocused to the degree that the entire target surface is scanned (with some overlap probable) during a field interval, the effects disappear. Although not necessarily a

practical display mode, operation with a small spot and coarse raster pitch provides a sensitive detector for scanning instability, and, to a degree, the effects observed will be present in whatever operational mode is chosen.

Figure 1 shows a 500-line display used for testing vertical stability. The raster on the 2×2 -inch vidicon target has a 4-mil pitch, and the beam diameter is of the order of 0.5 mil. If after scanning a field the beam does not retrace its previous path within a fraction of its diameter, an appreciable amount of "virgin" charge will be contacted on the photoconductor surface. The result is an increased video signal

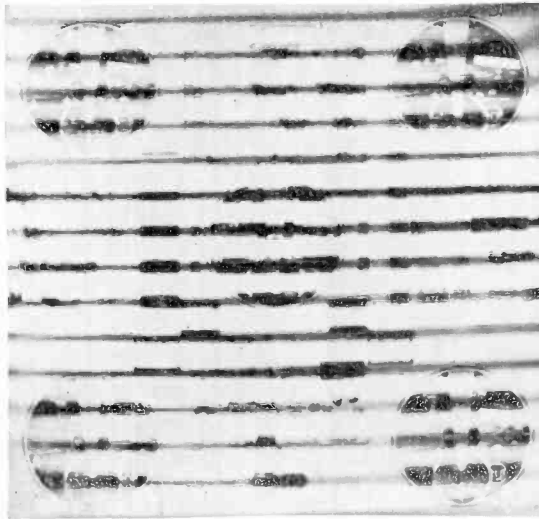


Fig. 2—Same display as in Fig. 1 shortly after a small height change.

amplitude, which produces varying degrees of flare, "skritch", interference, and loss of vertical resolution, depending upon the nature of the beam instability. It has been observed over a period of months that picture stability also improved as the stability of the camera vertical-deflection amplifier and its associated power supplies was improved.

An effect that is commonly encountered in a high-definition system employing return-beam vidicons is shown in Figure 2, where the Figure 1 scanning conditions have been perturbed by a small adjustment in the *height*-control setting. Periodic bands of virgin charge are read out, and the disturbance is observed for 10 seconds or more before a charge equilibrium is re-established. The visual effect is actually

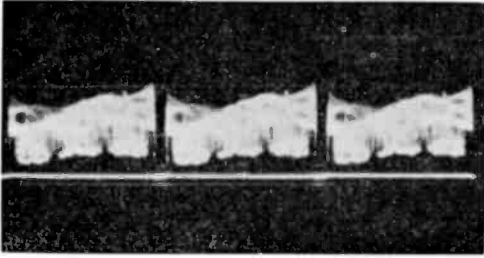


Fig. 3—Integrated video signal for stable test pattern.

considerably greater than suggested by a comparison of the photographs; the latter received only one-fifth the standard exposure to provide a better reproduction. Figure 3 shows the integrated video signal from the camera under the standard Figure 1 test conditions. When the centering-control setting is adjusted slightly, the entire target may present a virgin surface so that the resulting video-signal amplitudes are sufficient to overdrive the amplifiers and shift the black level, as shown in Figure 4. The entire field then flares up in intensity and masks the observation of detail. In both figures the amplitude is 0.5 V/cm and the time base is 5 msec/cm.

At least three additional related disturbances can be attributed to vertical-scanning instabilities. Figure 5 shows the interference patterns produced between the scanning raster and vertical-resolution wedge, and also the interference in the vertically oriented bar pattern on the right. The geometry of the interference diamond observed in the wedge is very sensitive to vertical instability, as is the display produced by a vertical sampling taken through the bar pattern. Either observation permits the detection of movements that are a fraction of the scanning-beam diameter, and is useful for trouble shooting thermal, electronic, and mechanical problems in the scanning circuits. Another

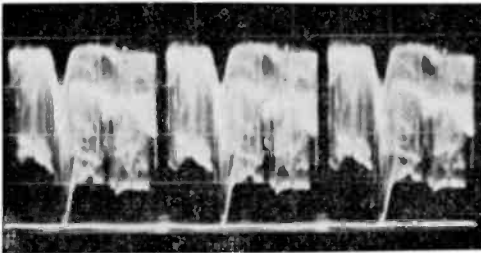


Fig. 4—Video signal shortly after small centering change.

effect not easily captured on film is a usually random (although sometimes ordered) horizontal tearing of lines that has been termed "skritch." This interference is probably related to noise or incipient oscillation in the vertical amplifiers or supplies at frequencies of the order of the horizontal scanning rate (35 kHz in these tests). A continuous low-level oscillation has been seen to produce a faint pattern of many bars, not unlike the Figure 2 display. The signal appeared across

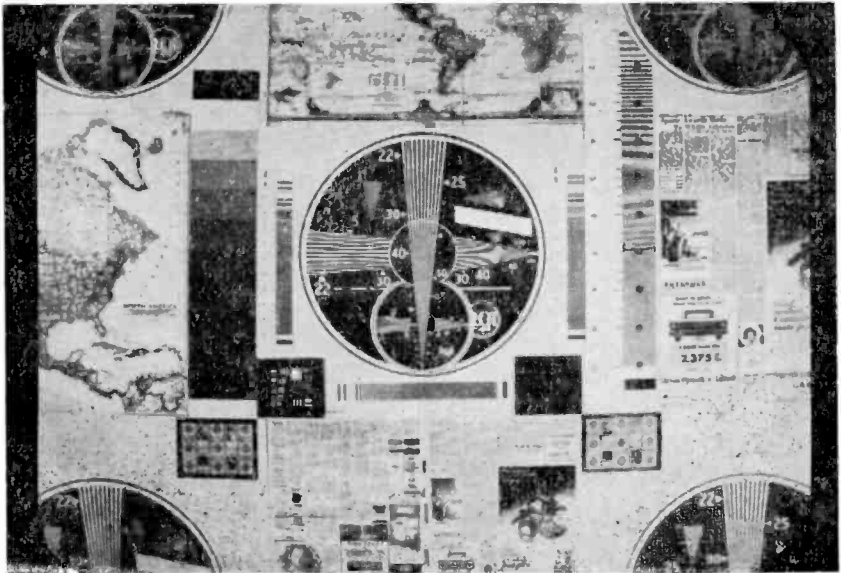


Fig. 5—2:1 monitor overscan showing interference patterns in display line structure.

an electrolytic capacitor at the power-supply output terminals. Finally, occasional localized bursts in picture intensity have been observed, apparently caused by power-line transients that get through the supply regulators. Faulty resistors and capacitors and poor contacts at connectors, potentiometers, and switches can also produce noise, and should be given attention during design and initial test of all associated equipment.

The disturbances observed in the 500-line test operation are still apparent when a higher-resolution scanning mode is used, such as a 2000-line raster. The major concern remains a loss of definition caused by the masking and integrating effects. The phenomena are of concern until the scanned paths of the raster overlap, such as occurs at about

4000 lines (depending upon the spot-intensity distribution). In every case, a new amplifier or power-supply circuit required a thorough initial test procedure before it could be satisfactorily incorporated in the television chain for a final performance critique.

Development of the Vertical-Deflection Amplifiers

The remainder of this paper is concerned with the development of a stable vertical-deflection system suitable for a high-definition television camera. The performance of an existing tube/transistor hybrid amplifier set a minimum stability standard for an all-solid-state circuit. There was also, of course, the desire for further improvement. Better performance was eventually obtained with both a differential-configuration type and a simpler passive-feedback-network type, although the latter has been developed to give the best stability.

The starting point was a circuit featuring a constant-current sawtooth generator and class A output driven by differential stages. D. Dion of RCA Aerospace Systems Division in Burlington, Mass., provided both a design and helpful guidance which, with minor modifications for sync differences, resulted in the amplifier prototype. A series of changes followed, during which signal-to-noise ratios were improved, a buffer circuit was developed, and more sophisticated sync processing was added. Figure 6 shows the development trends in block diagram. In the first version, difficulty was encountered with noise in the differential (Darlington) input stage. A decrease in the input impedance (current gain) provided a substantial noise improvement, but affected waveform linearity by shunting the sweep capacitor excessively. A second design featuring greater input signal and a buffer stage to unload the capacitor was then built. For minimum power loss in the current-sensing (feedback) resistor, a 12-dB amplifier was used to provide the increased feedback signal. It was possible to hold signal distortion levels in this feedback amplifier to less than 0.01%, but apparently it injected $1/f$ noise. A comparison with the third design in Figure 6, which accepted greater feedback-resistor losses, shows the greater noise levels present with the feedback amplifier.

At this point, it is fitting to describe the criteria for evaluating noise. The classification of signal-to-noise ratios (SNR), although a somewhat subjective process, has been made within the following format. All the amplifiers had a bandwidth of the order of 5 kHz.* Johnson noise was classified to occupy the range of 0.5 to 5 kHz, and $1/f$

* A lesser amount slows the retrace, and an excessive bandwidth leads to higher Johnson noise and feedback instability.

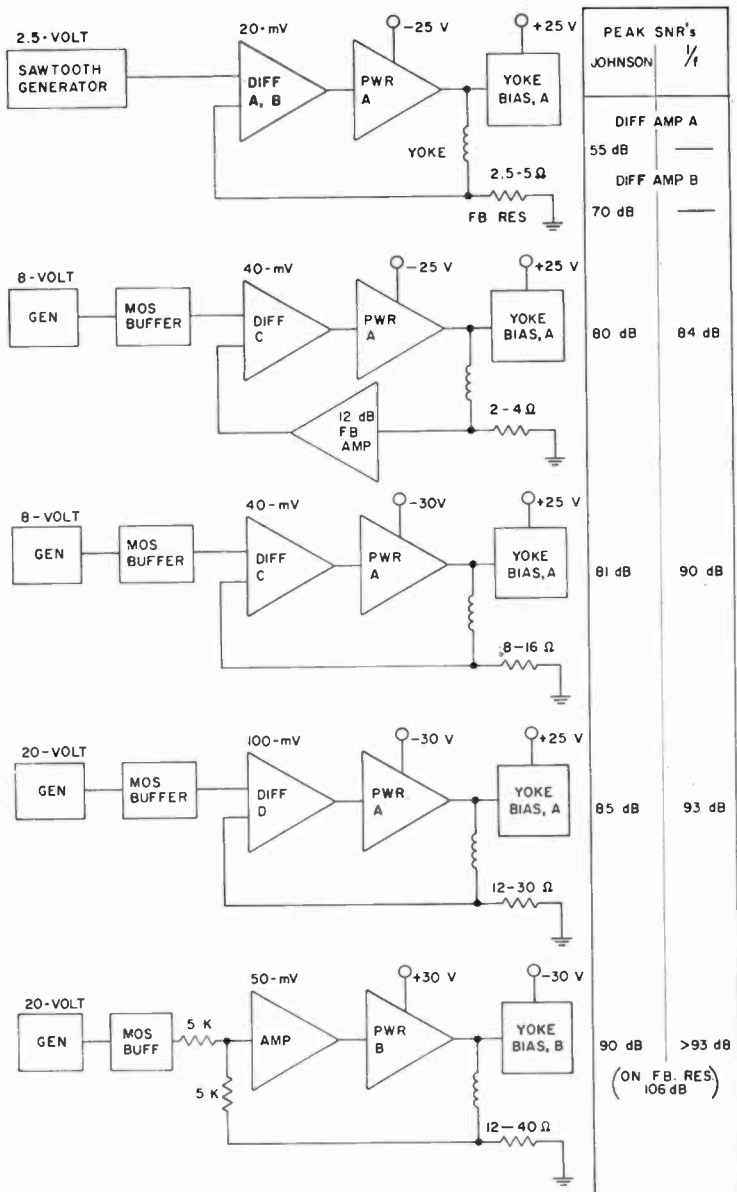


Fig. 6—Vertical-amplifier development.

noise the range from about 1 to 100 Hz. Noise observations were made with a Tektronix type-545 oscilloscope and a type-D (1-mV/cm) differential-input unit. A greater sensitivity would have been advantageous, and is considered necessary for further circuit improvement. All SNR's quoted are a ratio of peak-to-peak signal to peak-to-peak noise, unless otherwise stated. The Figure 6 data were taken at the input to the power transistor, where signal level was highest in the early amplifiers. In later designs having higher signal levels, noise is more readily measured on the feedback resistors.

In the amplifier development, a brute-force approach was employed in the fourth design. Signal level was increased to 20 volts, which required that the integrated circuits in the buffer and input stages be replaced by transistors having higher collector-to-emitter voltage ratings. A further improvement in SNR was obtained, and, for the first time, performance in the television chain exceeded that of the "standard" tube/transistor hybrid. On the other hand, further increases in input and feedback signal levels were limited by power-supply potentials, and attention was again directed to the input-amplifier stage to assure that it operated to best advantage. C. F. Wheatley of the RCA Somerville Integrated Circuit activity provided the encouragement to develop a passive-network feedback circuit in which the input stage is operated at a relatively low current level. This approach has given the best performance to date, and is recommended above the others. It should be realized that power-supply performance was also improved during the development period and influenced the noise levels. If, for example, a feedback-amplifier circuit were designed using the latest amplifier and supply as prototypes, performance might be superior to that obtained in the earlier tests.

Amplifier Description and Performance

A vertical-amplifier circuit featuring a passive feedback network is shown in Figure 7. The section shown in Figure 7(a) includes a CA3000 integrated-circuit constant-current generator that charges a sweep capacitor through transistor Q201. The charging-current waveform shown in Figure 8 indicates a variation of the order of 0.001% in the 50 μ A level.* A sweep capacitor is periodically discharged through Q202 at the upper left by a delayed sync pulse, shown in Figure 9. (A zero-potential reference has been superimposed on the photograph near the pulse peaks.) The resultant sawtooth at the

* Initial tests indicate that lower charging-current levels are feasible, so the sweep-capacitor size for slow-scan operation might be reduced by a factor of three or more.

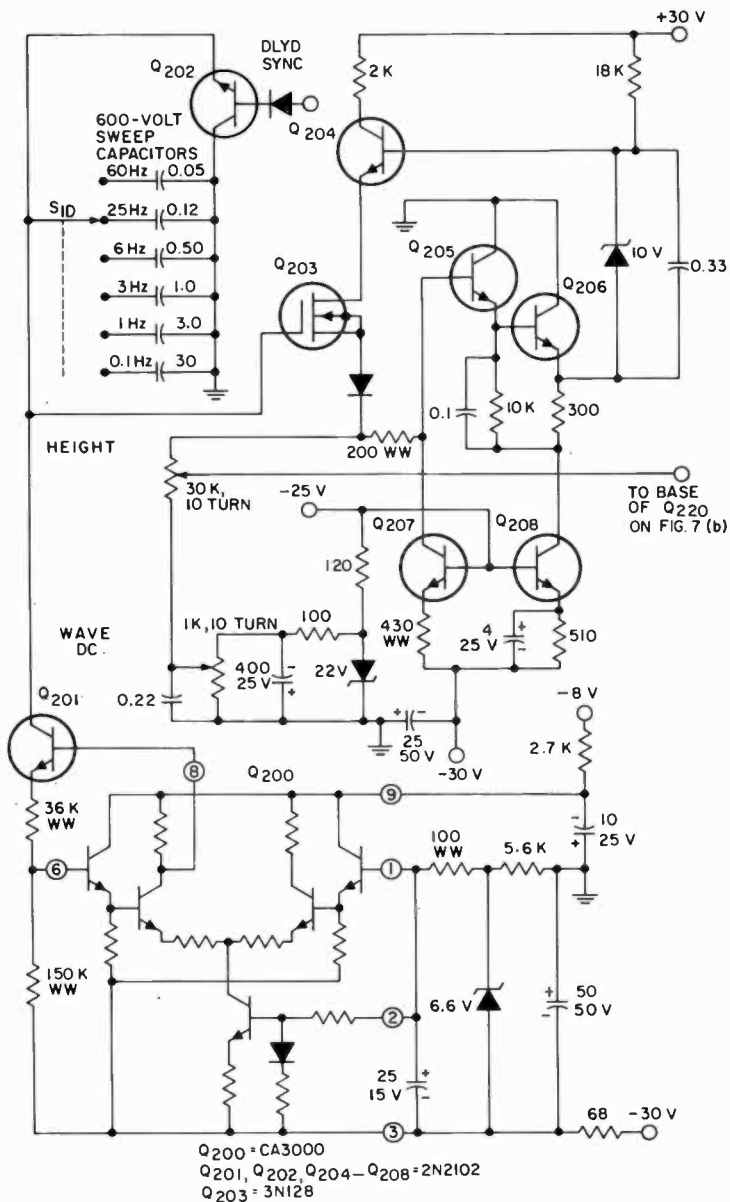


Fig. 7(a)—Vertical-deflection amplifier with passive feedback network.

ing functions, as shown in Figure 12. The variation of height produces a change in dc level that can, of course, be corrected with the centering control. The height-potentiometer resistance would have to be reduced by more than an order of magnitude to avoid this interaction, which would result in an excessive current excursion in Q203 for linearity requirements. A change in height also varies the feedback gain, but the consequences are not detrimental under normal operating conditions, where the control is set near a maximum position.

Input transistor Q220, shown in Figure 7(b), is a low-noise small-signal type operated from a source of about 2500 ohms at 40 μ A collector current. A first-stage voltage gain approaching 20 dB and a feedback-loop gain exceeding 40 dB assure that the noise contribution from the following stages is minimized. A 50-mV difference at the base of Q220 produces about 4 volts of drive at Q224 and a 1-ampere excursion in yoke current for feedback resistances of 20 ohms or less. Figure 11 shows superimposed output-current waveforms for a 1-ampere swing. The dc yoke-bias current was varied from 0.5 ampere (center trace) down to 0.2 ampere and up to 0.9 ampere. A linear range exists for about 1.6 amperes. The "wobble" on the lower waveform is ringing caused by the bias-supply choke during retrace, which occurs in a little less than 1 millisecond with a 12-ohm (minimum) feedback resistance. Figure 12 shows a retrace time under $\frac{1}{2}$ millisecond with a 32-ohm feedback resistance, a common choice for a 4.5-inch return-beam vidicon, which requires about 0.5 ampere of peak-to-peak yoke current. Figure 13 shows the collector-emitter retrace pulse on the output transistor, as limited by a 90-volt Zener diode. A zero potential trace is included for reference.

The feedback resistors are selected to provide 2-dB variations. The usual operating practice employs the greatest feedback consistent with obtaining a fully scanned display for the test conditions; best amplifier stability is achieved by this method. The 0.006- and 0.22- μ F capacitors across the yoke and feedback resistors limit the coupling of horizontal-scanning pulses, and the amplifier bandwidth is established by the 470-pF capacitor on the collector of Q220. Another critical capacitor is found at the base of the height control, where a large bypass capacitor would normally be suitable for fast-scan operation. It is, however, impractical to bypass at low scanning rates without introducing a distortion component on the sweep waveform. Therefore, the capacitor is selected to produce a minimal shunting effect at the highest scanning rate.

Figure 14 shows the voltage-supply network [section (a)] and

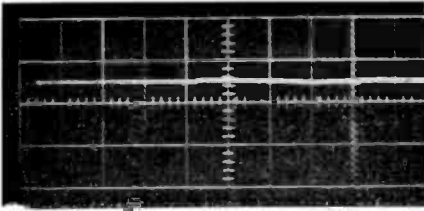


Fig. 8—Charging-current waveform measured at pin 6 of CA3000. Vertical scale, 1 mV/cm (ac); horizontal scale, 5 msec/cm.

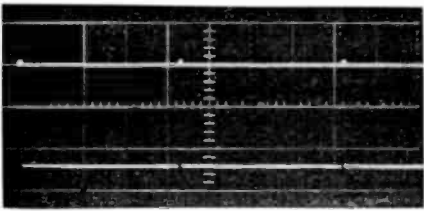


Fig. 9—Delayed sync pulse applied to Q202. Vertical scale, 50 volts full scale (dc); horizontal scale, 5 msec/cm.

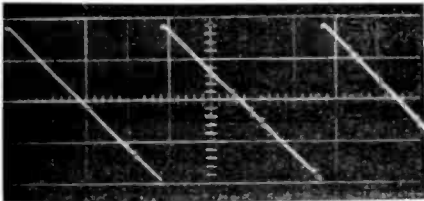


Fig. 10—Sweep waveform measured at source of Q203. Vertical scale, 20 volts full scale (dc); horizontal scale 5 msec/cm.

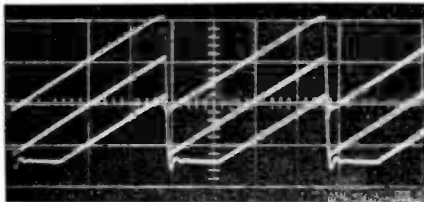


Fig. 11—Output-current waveforms on 32-ohm feedback resistor. Vertical scale, 20 volts full scale (dc); horizontal scale, 5 msec/cm.

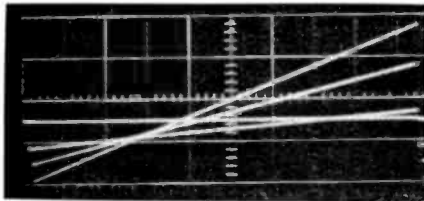


Fig. 12—Output-current variations caused by "height" control measured on 32-ohm feedback resistor. Vertical scale, 20 volts full scale (dc); horizontal scale, 2 msec/cm.

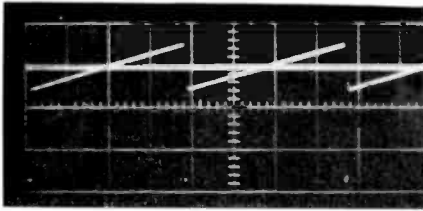


Fig. 13—Collector potential of output transistor. Vertical scale, 100 volts full scale (dc); horizontal scale, 5 msec/cm.

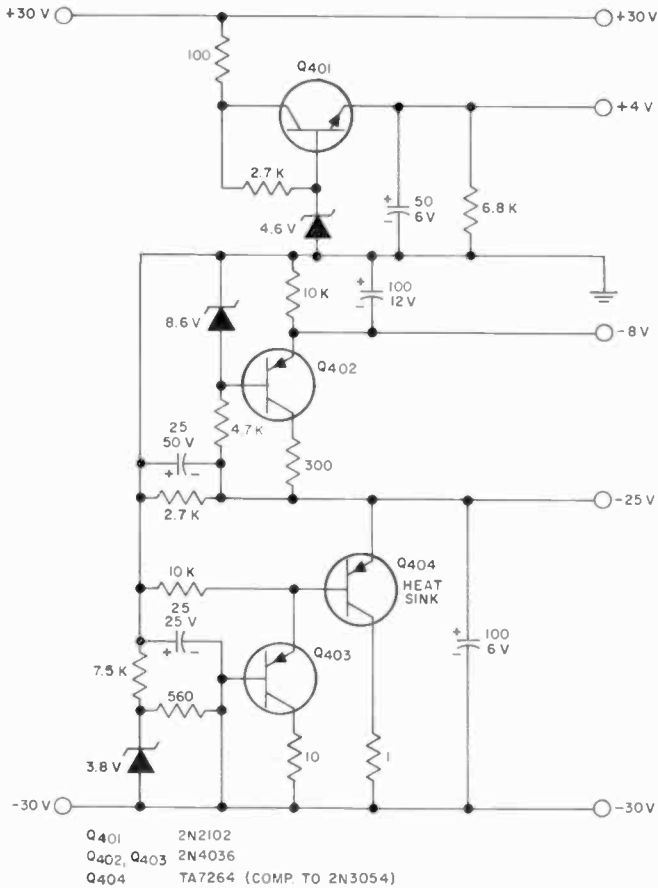


Fig. 14(a)—Voltage supply.

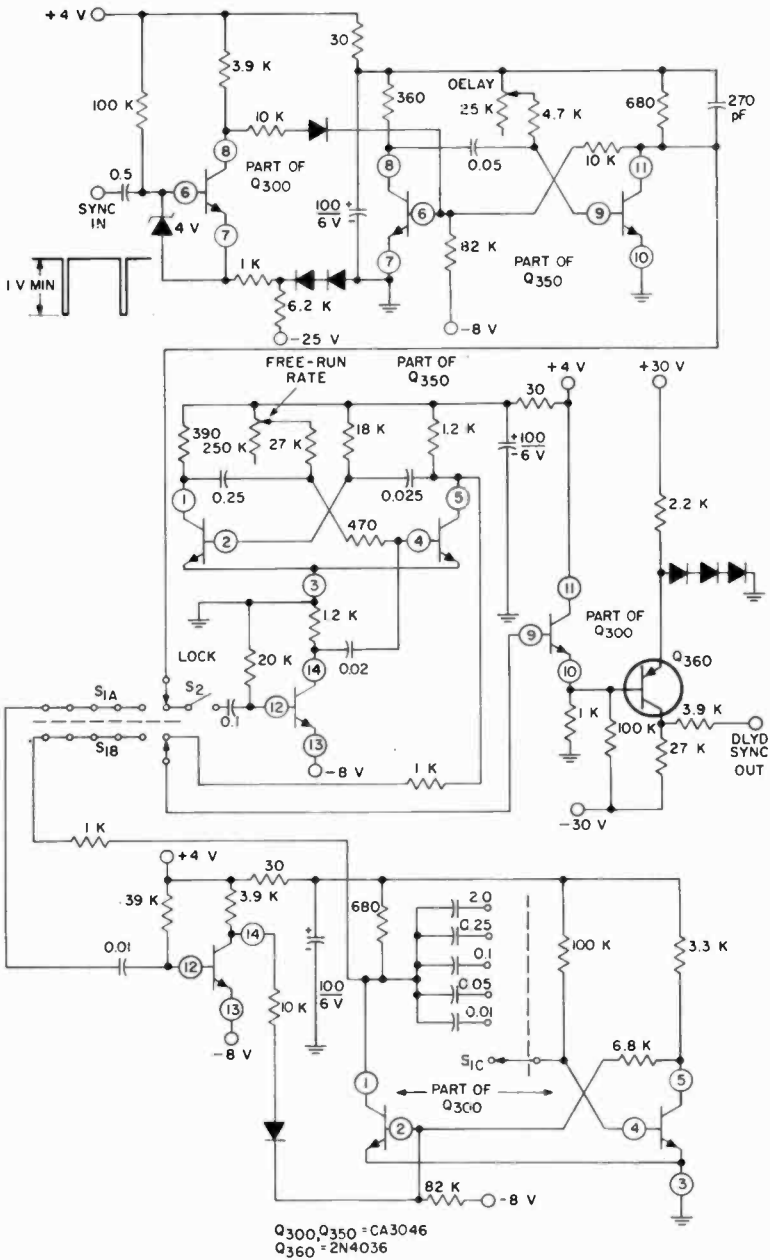


Fig. 14(b)—Sync processing.

sync-processing amplifier [section (b)] for the deflection amplifier of Figure 7. Two high-quality 30-volt 1-ampere power supplies are required. The sync-processing circuits are of straight-forward design and operate successfully with pulses down to 1 volt in amplitude. A multivibrator provides 0.3- to 1.4-msec sync delay and can lock in a second 25- to 200-Hz free-running unit at the normal 60-Hz scanning rate, thereby providing for scanning in the event of a sync failure. A pulse width of about 400 μ sec for capacitor discharge is provided by the pulse-forming network on pin 12 of Q350. At lower scanning rates, the delayed sync is applied to a third multivibrator, which maintains a constant pulse width percentage for 25-, 6-, 3-, 1-, and 0.1-Hz rates. Capacitor coupling is used between most stages to avoid signal radiation caused by the fast rise and fall times of which the transistors are capable.

Figures 15(a) and 15(b) show the schematic diagram for an amplifier having a differential-input configuration. Reasonably low noise levels were attained with this design, and the potential for long-term stability may exceed that available from a passive-feedback-network type. Because the differential-input design was not fully developed, no additional data are presented for this type.

Noise and Stability

The output-current noise for a typical operating condition of a 4.5-inch return-beam vidicon is shown in Figure 16. The noise appears as a broadened oscilloscope trace of the minimum (100-mV) sawtooth, viewed with high oscilloscope gain. An order-of-magnitude greater vertical sensitivity (100 μ V/cm) would have been desirable for a more accurate noise evaluation in the later amplifier designs. The height control is set at a minimum and the waveform is viewed on a 32-ohm feedback resistor. To assure that the noise is generated in the amplifiers rather than appearing on the sawtooth signal, the input network can be bypassed by a 1000- μ F capacitor, as in Figure 17 (or the "Waveform DC" potentiometer replaced by a battery). The 100-mV signal is then reduced to near-zero amplitude, but the 0.1-mV-high oscilloscope trace remains. The noise burst appearing in Figure 16 (fourth reticle column) is presumed to be injected by a power supply; a similar transient was also recorded in Figure 18,* which shows the minus 30-volt supply noise. Either very few of these bursts occurred within the several-minute observation periods, or they were not readily detected by eye.

* During a 1/25th-second exposure.

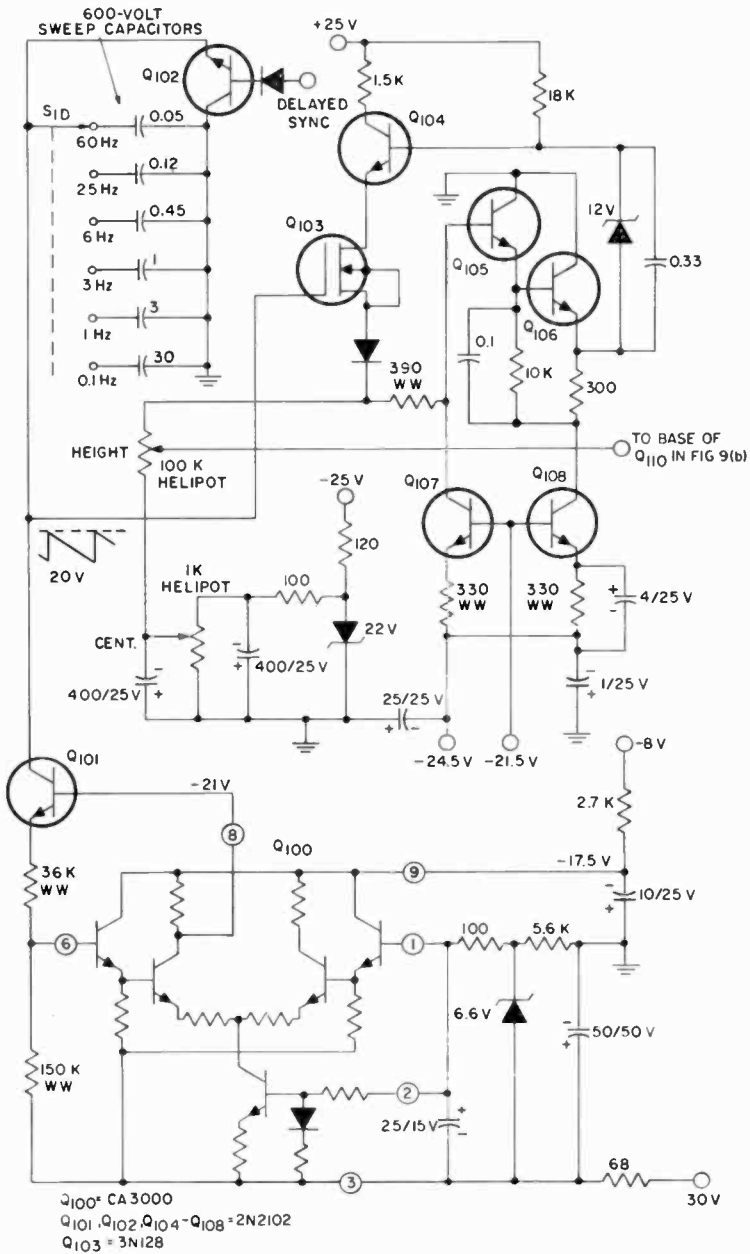


Fig. 15(a)—Vertical-deflection amplifier, differential-input configuration.

An estimate of the required vertical stability can be made by comparing the vidicon target height and beam diameter. In a typical test, a movement of one beam diameter produces an instability of 1 part in 4000, or an equivalent *peak-to-peak* SNR of 72 dB, and the resulting disturbances are severe. Instabilities caused by amplifiers having a 90-dB peak-to-peak SNR are readily observed on the television test chain, and the performance of a 100-dB vertical-deflection system verifies that the effects of movements less than 10 per cent of a beam diameter can be detected. It is hard to appraise how critical the stability requirements could be for a particular application. In general, it has been demonstrated that, when viewing an otherwise still scene

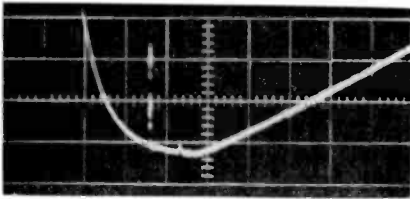


Fig. 16—Output-current noise measured on 32-ohm feedback resistor with minimum "height" setting. Vertical scale, 1 mV/cm (ac); horizontal scale 100 μ sec/cm.

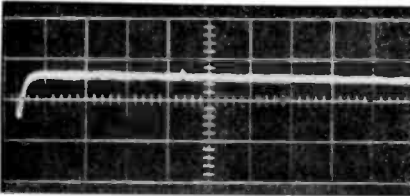


Fig. 17—Output-current noise under Fig. 16 conditions with 1000 μ F on amplifier input network. Vertical scale, 1 mV/cm (ac); horizontal scale, 100 μ sec/cm.

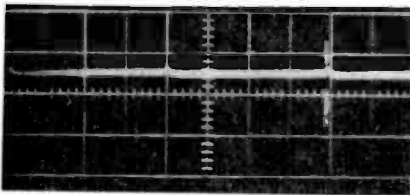


Fig. 18—Noise on 30-volt power supply. Vertical scale, 1 mV/cm (ac); horizontal scale, 5 msec/cm.

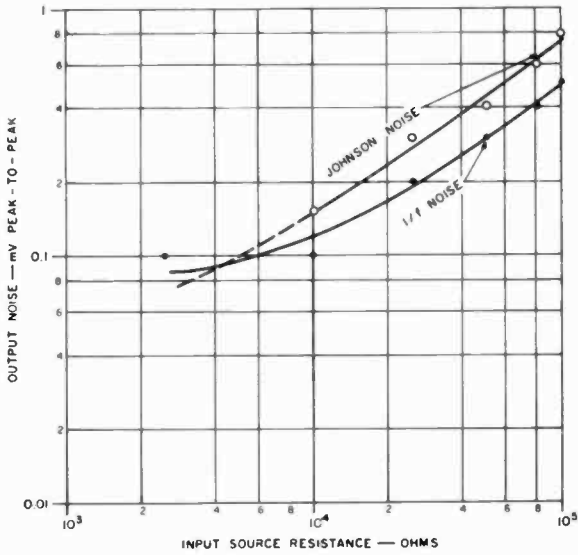
having a good picture quality, an observer is quick to criticize display instabilities, particularly when they interfere with his ability to resolve fine detail.

A further study of noise at the input amplifier Q220 (Figure 7) shows that output noise is a function of the collector current and driving impedance at this stage. Earlier tests at 1 mA and 100 μ A led to the present 40- μ A operation of the 2N4259. Figure 19(a) shows the relationship between Johnson and $1/f$ noise and the source resistance, as determined by an oscilloscope on a 32-ohm feedback resistor.* Measurements made near the detection-sensitivity limit suggest that $1/f$ noise is relatively constant for source resistances between 2000 and 10,000 ohms. Figure 19(b) shows open-loop noise measurements made at the output-transistor base, which have been referred to the amplifier input (with a gain of 80 and a factor of 6.0 to relate peak-to-peak and rms noise levels). Similar relationships between noise and source resistance observed in Figure 19(a) and (b) indicate that input stage design is a major factor for achieving low-noise performance. Figure 19(b) also shows a photograph of multiple 1/25-second exposures of open-loop noise used for estimating the Johnson and $1/f$ "components." The amplitude in this 2500-ohm test is 2 mV/cm, the time base is 200 μ sec/cm, and the interpretation of the photograph is 1 mV peak-to-peak of Johnson noise (the "high-frequency" variations) and 2 mV of change in the dc ($1/f$) signal levels of individual traces. Many such recordings were made at several values of source resistance to acquire the Figure 19 data. Again, no rigorous definition of $1/f$ noise has been attempted, and the data should be interpreted with this reservation.

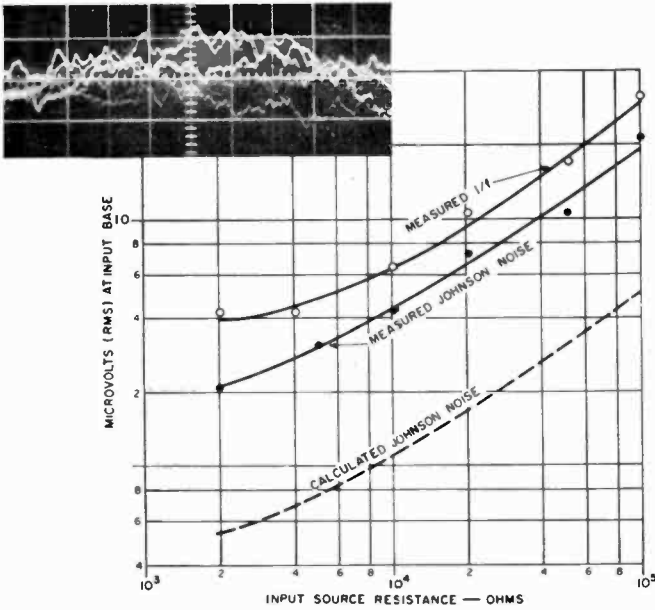
A calculation of Johnson noise permits comparison with measured data to verify that operating conditions are proper. Baxandall has shown³ that, based upon the theoretical studies of Van der Ziel and others, an equivalent circuit for amplifier noise can be represented in the audio range by a source resistance and voltage and current generators driving a noiseless amplifier, shown in Figure 20. The current generator produces a noise current I_N given by

$$I_N = \sqrt{\frac{4kTB}{2\beta/g_m}} \quad (1)$$

* Wire-wound resistors were inserted between the feedback network and transistor base to vary the source resistance.



(a)



(b)

Fig. 19—Noise in the passive-feedback-network amplifier: (a) closed-loop measurements on 32-ohm feedback resistor; (b) open-loop measurements referred to input base.

The short-circuit Johnson-noise-current resistance, R_{Ni} , is given by

$$R_{Ni} = 2\beta/g_m \quad (2)$$

The voltage generator produces a potential V_N given by

$$V_N = \sqrt{4kTB[r_{bb} + (1/2g_m)]}. \quad (3)$$

That is, the Johnson-noise-voltage resistance:

$$R_{Nv} = r_{bb} + (1/2g_m). \quad (4)$$

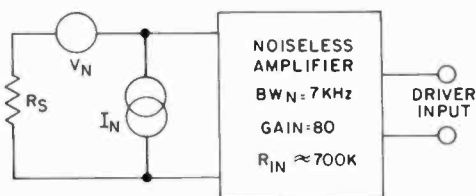


Fig. 20—Equivalent open-loop noise circuit.

In these equations, k is the Boltzmann constant, T is the absolute temperature, B is the noise bandwidth,* and β , g_m , and r_{bb} are the transistor current-transfer ratio, transconductance, and extrinsic base resistance. The 40- μ A operation of the 2N4259 produces the measured values $\beta = 60$ and $g_m = 2200 \mu\text{mhos}$, and r_{bb} is estimated to be about 100 ohms. For a noise bandwidth of 7 kHz and (low-current) junction temperature of 300°K, the factor $\sqrt{4kTB} \approx 1 \times 10^{-8}$, and the resistances can readily be computed as $R_{Nv} = 330$ ohms and $R_{Ni} = 55,000$ ohms. The noise components caused by the voltage generator, source resistance, and noise-generator current through the source resistance (for a high-input impedance operation) may then be summed to produce the dashed line in Figure 19(b). The measured Johnson noise is seen to be a constant factor of four above the computed values. Although agreement is not good enough to assure optimum operation of the transistor, it is not likely that a large improvement would result from revised conditions. The theory calls for a considerable reduction in source resistance to realize significantly better noise performance, a direction which adversely affects sawtooth linearity.

* A value $\pi/2$ times the 3-dB-down bandwidth.³

It is possible that operation at a lower collector-current level might produce somewhat better performance, for Baxandall points out that there is an advantage at very low ($1\text{-}\mu\text{A}$) currents in situations where $1/f$ noise is significant.⁴ This region has not been fully explored. It is cautioned that the noise contribution from later stages must be continually evaluated during amplifier development to assure that full performance is being realized.

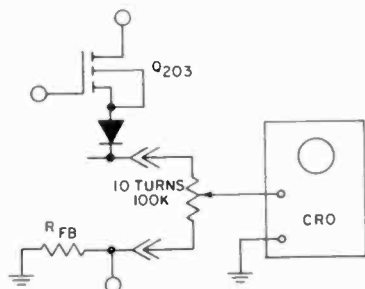


Fig. 21—Circuit for distortion measurements.

Distortion and Linearity

The determination of amplifier distortion—the inability of the amplifier stages to reproduce the generated sweep waveform—can be made with relative ease. Figure 21 shows a multiturn potentiometer at the outer terminals of which the input (MOS-source) and output (feedback-resistor) waveforms are applied. If no amplifier distortion exists, it should be possible to view a horizontal trace (punctuated by retrace pulses) with the proper setting of the potentiometer slider.* The distortion shown in Figure 22 was produced during a 1-ampere peak-current excursion at maximum (20-volt) signal level and represents a worst-case situation. The maximum deviation from the horizontal is of the order of 0.4 mV, or 0.002% of the signal amplitude. The amplifier is therefore capable of reproducing the generated sweep waveform with excellent fidelity.

The linearity of the sweep waveform is more difficult to measure. Although Figure 8 indicates that a sweep capacitor should experience a relatively constant charging current, it is possible that dielectric lag or leakages affect the linearity of voltage rise. The 60-Hz linearity tests

* In the case of the differential-style deflection amplifier, the signals are applied directly to a high-gain differential-oscilloscope input.

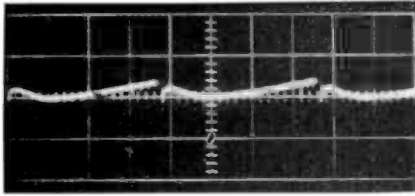


Fig. 22—Amplifier distortion of the input waveform. Vertical scale, 1 mV/cm (ac); horizontal scale, 5 msec/cm.

were made with Mylar* molded tubular 600-volt capacitors. Intermediate scanning rates are achieved with resin-impregnated metallized-paper capacitors, and the 0.1-Hz slow scan is obtained with 600-volt metal-cased paper-oil capacitors. Critical linearity appraisals have not been made for the latter types, and a more thorough study would be necessary to determine how capacitor choice affects linearity.

The 2N2102 discharge transistor Q202 has maximum collector and emitter cutoff-current ratings of a few nanoamperes, and does not appear to cause linearity problems. Although the current pulses in this stage are several tenths of an ampere, the duty cycle is relatively short, and a thermal recovery should occur before high-temperature leakages could cause trouble. The exceptionally high input impedance of the 3N128 MOS transistor makes it ideal for coupling to the capacitor, but only moderate current excursions are permitted in order to restrict waveform distortion. As previously mentioned, the source-resistance requirements of the input stage have resulted in several design compromises.

Measurements of waveform linearity were made by coupling a second set of vertical coils to the existing pair in the circuit of Figure 23.* A constant rate of current change of 1 ampere in 1/60 second produces a dc potential of about 2.5 volts on the 42-mH yoke. Observa-

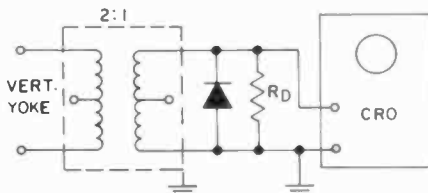


Fig. 23—Circuit for linearity measurements.

* Trademark of E. I. duPont de Nemours, Inc.

* Note that the ability to specify linearity by this method is limited if amplifier distortion levels are approached.

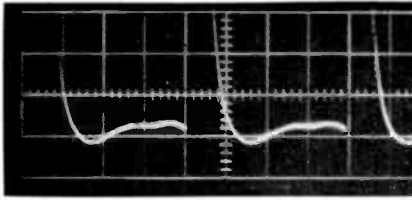


Fig. 24—Sweep-waveform nonlinearity with 20-ohm feedback and 2200-ohm damping. Vertical scale, 1 mV/cm (dc); horizontal scale, 5 msec/cm.

tion of retrace-pulse amplitudes on the primary and secondary coil pair indicated a transformer ratio of 2:1, so that the dc level referred to the secondary is about 1 volt. The degree of nonlinearity will therefore be specified by the fractional deviation from a horizontal oscilloscope trace of a 1-volt dc level. Unfortunately, the measurement can become complicated by pickup of extraneous signals at the coils and ringing from the retrace pulse, as well as by the relatively low dc reference levels produced under slow-scan operation. Figures 24 and 25 show the effects of 120-Hz ripple from steel-enclosed power supplies about 5 feet from the coils, which were oriented for minimum coupling. Selection of a suitable scanning frequency permits the ripple to drift across the oscilloscope, but the interference still hinders observation. In addition, the choice of a damping resistor affects the pulse duration, which can influence a linearity appraisal. The 820-ohm damping of Figure 25 is near the critical value. A further reduction to 750 ohms removes the positive overshoot, but the influence of the pulse becomes more difficult to estimate. The data suggest a deviation of the order of $\frac{1}{2}$ to 1 mV at most—that is, a nonlinearity of 0.1 per cent or less. It has not been possible to assess the effects of leakage in the capacitor-charging circuit or to derive buffer-stage transfer characteristics from the waveform shapes.

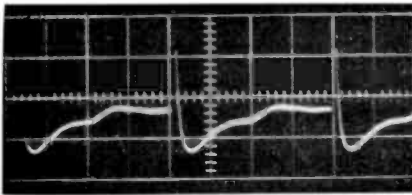
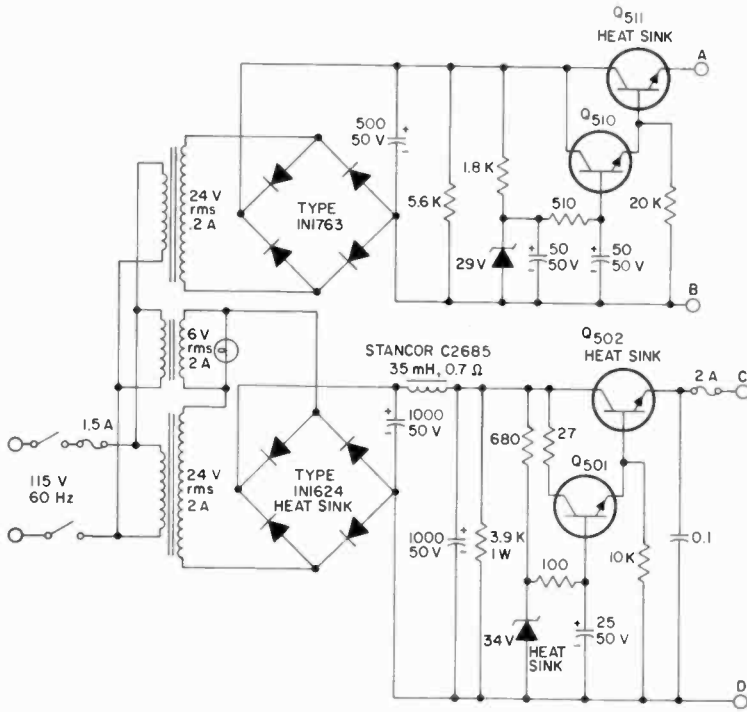


Fig. 25—Sweep-waveform nonlinearity with 20-ohm feedback and 820-ohm damping. Vertical scale, 1 mV/cm (dc); horizontal scale, 5 msec/cm.

Power-Supply Requirements

The power supplies developed for the camera-deflection amplifier provide 1 ampere (nominal) at 30 volts with 0.005% load regulation. Noise and ripple peak-to-peak values are more than 100 dB down and line regulation is better than 0.001% for a $\pm 10\%$ input variation. The



NOTE: TERMINALS A THROUGH D ARE CONNECTED TO CORRESPONDING TERMINALS OF FIG. 26 (b)

Fig. 26(a)—30-volt regulated power supply. 1-ampere load regulation, 0.005%; line regulation, $< 0.001\%$ for $\pm 10\%$ ac input; SNR, dc output to peak-to-peak noise, > 100 dB.

load-regulation figure is probably better than it need be for present applications, for the insertion of an ammeter (resistance) in the line has not caused any observable difficulties. However, good noise rejection and line isolation are very important, and the design features used to obtain them generally result in good load-regulation characteristics as well.

The supply shown in Figures 26(a) and 26(b) has been developed specifically for vertical-deflection service. Its prototype may be found

in the Bureau of Standards Preferred Circuits Handbook.⁵ Refinements include a filter choke, input "roughing" regulators, increased sensing-loop gain, improved Zener diode bypassing, and amplifier and reference-Zener-diode current sinks. The lower "main"-supply portion produces a 33-volt output having a 2.5-mV (1 ampere dc) peak ripple at the rough-

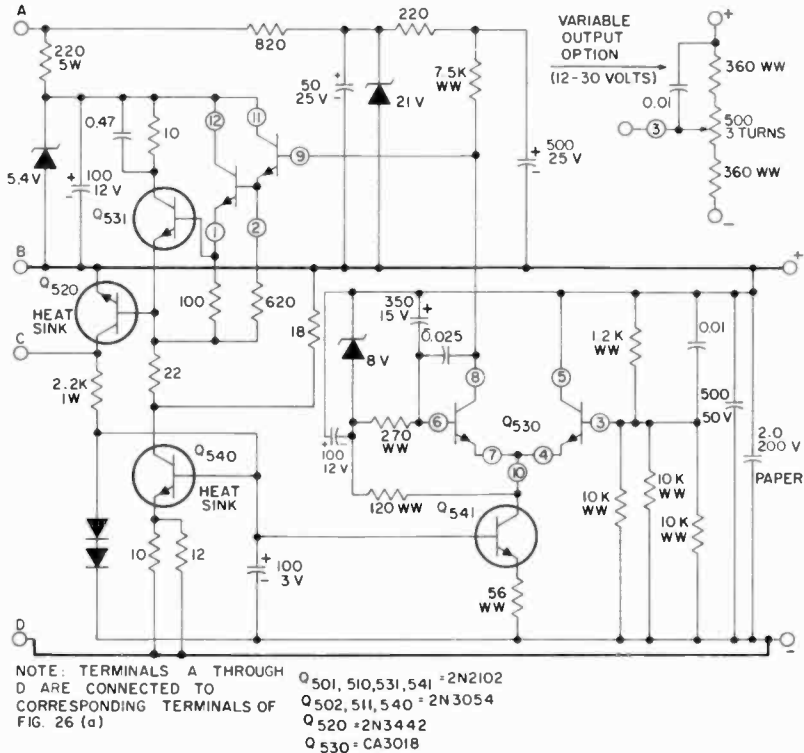


Fig. 26(b)—30-volt regulated power supply (continued).

ing-regulator output, maintained with $\pm 10\%$ line fluctuations. The 2N3442 series regulator is driven by a CA3018 differential amplifier and impedance-matching network through a 2N2102, which can supply the required base-current range with a relatively small loss in driving voltage. An amplifier imbalance of 0.3 mV produces sufficient signal with 54-dB voltage gain to swing the series regulator 1 ampere. Oscillation is suppressed by the 0.025- μ F bypass capacitor at the amplifier load resistor.

A stable low-noise reference potential is produced at the CA3018 pin 6 by a resistor-capacitor network and Zener diode; 350 μ F was

necessary to quiet Zener noise. Zener and differential-amplifier currents flow through sink Q541; current apportionment is established by the 7500-ohm load resistance and voltage reference, and the 120-ohm

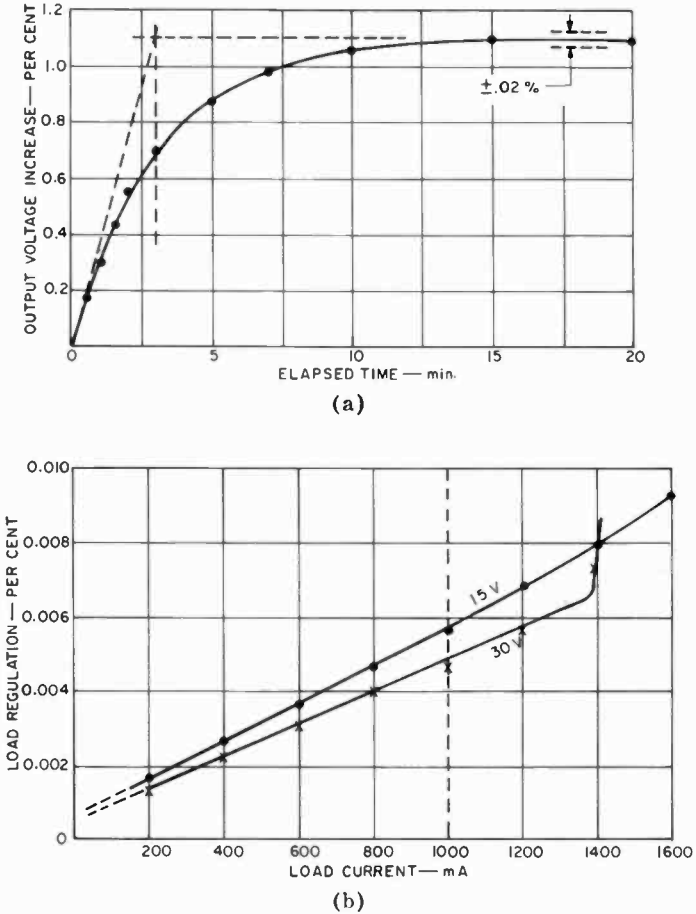


Fig. 27—Some power-supply characteristics: (a) supply warm-up characteristics; (b) supply-load regulation.

resistor and emitter-base junction potential. The upper auxiliary-supply portion provides power for the matching and driving network and a separate, extensively filtered and decoupled reference for the amplifier load resistor. Again, an additional regulator stage (Q510 and Q511) was needed for good line isolation.

Current sink Q540 maintains a no-load current through the series

regulator (by way of the 18-ohm resistor) and assures a constant low-input base current for the matching network. The voltage-sensing divider is composed of several resistors so that temperature-rises in individual legs are similar. This divider is the most temperature-sensitive circuit portion and deserves isolation from possible air-current fluctuations. Because it is not necessary to achieve excellent long-term temperature stability in the television test chain, amplifiers and supplies are relatively underdeveloped in this respect.

The supply warm-up transient is shown in Figure 27(a). A 1.1% exponential rise with 3-minute time constant is followed by stable operation within $\pm 0.02\%$ for the remainder of an hour. The load-regulation curves of Figure 27(b), obtained with the variable-output option of Figure 26, show that the supply will deliver 1.4 to 1.6 amperes before regulation is lost.

Acknowledgment

The need for high-stability vertical-deflection components was made evident and evaluation made possible by O. H. Schade, Sr.'s high-definition test facility in Harrison, N. J. Layout and construction of amplifiers and supplies, as well as much helpful troubleshooting, were performed by C. Trushell.

References

- ¹ O. H. Schade, Sr., "A 60-Megacycle Video Chain for High-Definition Television Systems," RCA REVIEW, June 1965, Vol. 26, No. 2.
- ² O. H. Schade, Sr., "A Solid-State Low-Noise Preamplifier and Picture-Tube-Drive Amplifier for 6-MHz Video System," RCA REVIEW, Vol. 29, March 1968.
- ³ P. J. Baxandall, "Noise in Transistor Circuits," Part 2, "Wireless World," Vol. 74, No 1398, p. 454, Dec. 1968.
- ⁴ See Reference (3), pp. 456, 457.
- ⁵ National Bureau of Standards, "Handbook Preferred Circuits Navy Aeronautical Electronic Equipment", Vol. II, Semiconductor Device Circuits, NAVWEPS 16-1-519-2, April 1962, p. 3-2.

Linear Solid-State Horizontal-Deflection Circuit For High-Definition Television Systems

O. H. Schade, Jr., RCA Electronic Components, Somerville, N. J.

Abstract—The performance of an ideal horizontal-switching circuit that has a ramp generator for linearity correction and that meets the requirements for superior stability and linearity in a high-definition TV system is closely approximated with solid-state circuitry. Careful attention to transformer design demonstrates that a 1- to 30-kHz scanning-rate range is practical; maximum non-linearities of 0.3 to 0.5 per cent have been achieved. Proper application of feedback is shown to correct inconsistencies in component operation and points to further developments that could provide substantial improvements in performance. Graphical determinations of distortion are used to describe the effect on the deflection circuit of failure to provide ramp linearity in the slow-scan mode and switching-circuit capacitor potentials that are constant in the fast-scan mode.

The horizontal switching circuit was developed for use with a 4.5-inch return-beam vidicon, but is adaptable to the 2-inch vidicon as well as to high-definition monitors. Provisions are made in the circuit for electronic selection of slow or fast scan rates and "zoom" operation (camera underscan). The immediate application is to a 4000-line, 100-MHz test chain used in the evaluation of high-definition-system components.

Introduction

High-definition television systems capable of the reproduction of images comparable in quality with aerial photographic images require scanning circuits of superior stability and linearity. Recent efforts at RCA have resulted in the development of stable, low-noise, vertical-deflection circuits¹ with 0.1% maximum nonlinearity, as well as the necessary power supplies and decouplers for the deflection circuits. Further efforts produced the horizontal-deflection circuits described in this paper. The vertical and horizontal circuits together complete the solid-state scanning requirements for a high-definition television test chain. Although developed primarily for the purpose of scanning a 4.5-inch return-beam vidicon, the circuits may be adapted to the 2-inch vidicon and the 17-inch high-definition kinescope monitor, as were earlier deflection circuits.

A nonlinearity approaching the 0.1% level attained by the vertical circuits is not an unrealistic goal for a horizontal-deflection circuit that is to handle more than 4000 picture lines and a 100-MHz video bandwidth. In addition, because the test-chain horizontal circuit may be used to explore a variety of applications, its scanning rate must be flexible; i.e., in the 1- to 30-kHz range. From the various horizontal-deflection circuits studied, a design developed at the RCA Aerospace Systems Division, Burlington, Mass. for a 4.5-inch return-beam-vidicon scan converter was selected as the most suitable for a test-chain prototype. The basic transistor switch circuit with ramp generator for linearity control was considered a sound approach because the evolution of a feedback loop enclosing an increasing number of circuit components could be employed with relative ease during stability investigations. Time limitations prevented the evaluation of yoke-current-sensed feedback or scanning rates below 5 kHz; in addition, power supplies were not available in time for final stability measurements. However, the good distortion levels attained, 0.3 to 0.5% maximum nonlinearity, indicate the value of this approach. In addition, initial tests of the circuit in the television chain show no basic limitations. Transformer measurements indicate that little additional development is necessary to extend the scanning-rate range down to 1 kHz.

Considerable effort was spent on transformer and ramp amplifier design to assure good circuit linearity. Changes were made in the horizontal-switch driving circuit so that it could more effectively sweep charge from the switch bases. Only minor revisions were made to the remaining circuits to suit sync level, centering control, damping, and scanning-speed logic needs.

General Circuit Description and Performance

Fig. 1 shows the circuitry used to operate the relatively simple horizontal switch circuit; the block diagram shows the transistor switch, damper diodes, retrace capacitor (C_R), and the driver transformer used to couple the horizontal yoke. The circuit follows basic solid-state horizontal-circuit operation² and, in addition, makes use of a ramp voltage to compensate for the switch-circuit resistance so that the potential across the reflected yoke inductance, and, therefore, the current rate of change, remains essentially constant. Other features include provision for slow/fast (S-F) scan logic at scan rates of 5 and 30 kHz, "zoom" control (camera-tube underscan), and SCR protection of the switch transistors. Capacitors C_1 and C_2 keep direct currents

from the windings of T_1 and T_2 ; centering current is blocked by the capacitors identified as C_c .

A current ramp of 10 A peak-to-peak flows in the switch circuit; a $6\text{-}\mu\text{s}$ retrace produces a flyback pulse in the order of 2500 V on the yoke and 500 V at the horizontal switch. The 4.3-mH $2.6\text{-}\Omega$ series-connected yoke experiences a maximum ramp current of 2 A peak-to-

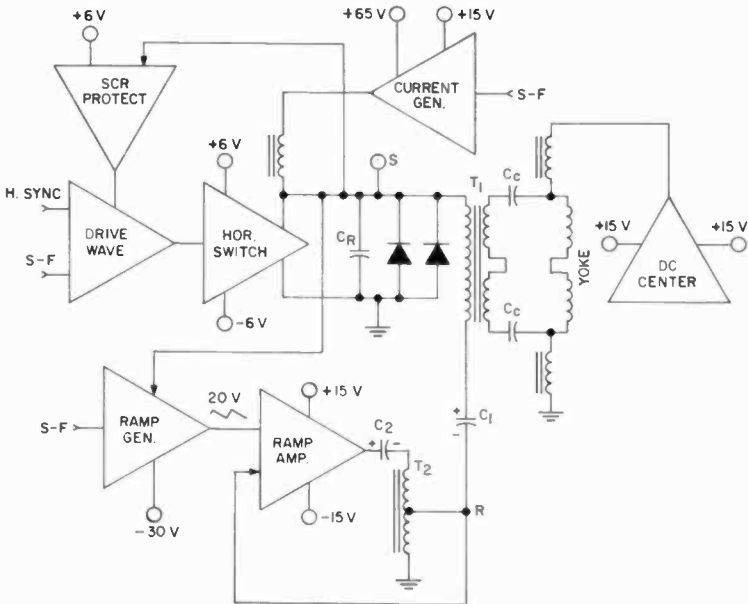


Fig. 1—Block diagram of the horizontal-deflection circuit.

peak; centering currents of ± 1 A are provided. The ramp generator produces a 20-V sawtooth with a maximum nonlinearity of 0.1%; the ramp output transistors provide up to 4 A peak-to-peak. The current generator typically supplies about 650 mA dc while the ramp amplifier draws approximately 1 A, so that deflection power is roughly 70 W at the 30-kHz rate.

Fig. 2(a) represents an idealized, simplified switch circuit comprising capacitance C_1 (which can initially be considered a battery), the ramp generator potential e_r , reflected yoke inductance L_y' , and total switch-circuit resistance R ; L_y' and R define the time constant $\tau = L_y'/R$. To obtain a linear current ramp in this circuit, the combination of capacitor potential e_c and ramp potential e_r must impress a con-

stant potential across L_y' during the scanning period t_s , as shown in Fig. 2(b). Fig. 2(b) represents the 5-kHz rate for the actual horizontal-switching circuit of Fig. 1. Under the fast-scan conditions (30 kHz) represented in Fig. 2(c), the ramp component is small; however, it is quite large and dominates at relatively slow rates (approximately 1 kHz), as shown in Fig. 2(d).

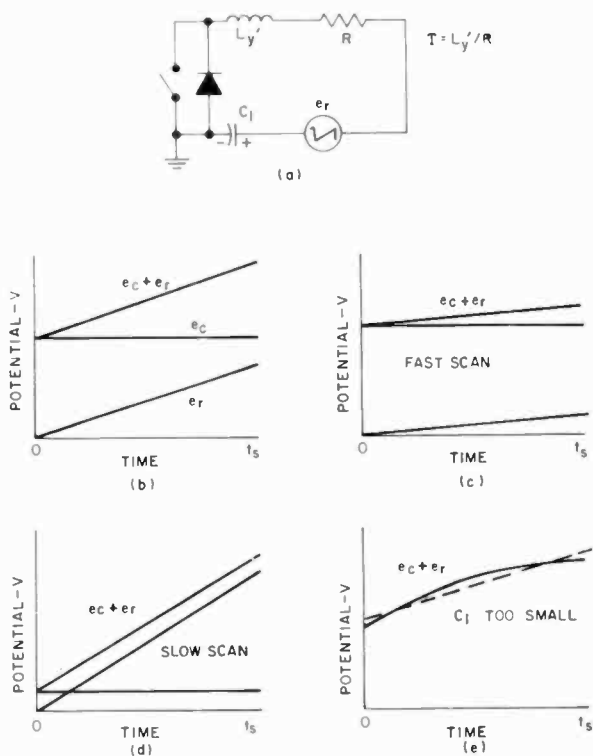


Fig. 2—Ramp and capacitor potentials in an ideal circuit: (a) schematic diagram of circuit, (b) potentials during scanning period t_s , (c) ramp component under fast-scan conditions, (d) ramp component under slow-scan conditions, (e) effect on ramp of too small a value of C_1 .

For a given peak-to-peak yoke current, the ramp voltage in the ideal circuit remains constant and independent of scanning rate because the resistance R remains constant. The constancy of e_c in the fast-scan mode and ramp linearity in the slow-scan mode are the predominant factors in producing a linear deflection.

Fig. 2(e) shows the effect of too small a capacitance C_1 . The clock-

wise current flow through the damper charges this capacitor to a maximum potential as the current goes to zero; the reversed flow through the switch then discharges the capacitor. The dashed line indicates a best-fit linear approximation, and specifies the maximum deviation from linearity. Fig. 3 shows the graphically determined

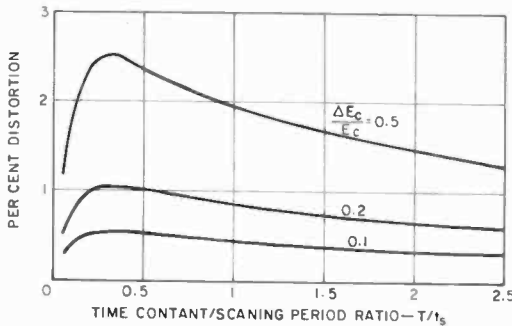


Fig. 3—Distortion of current ramp as a result of capacitor voltage changes.

deviations from linearity in the current flow as a function of τ/t_s for a circuit that has a potential ($e_c + e_r$) with a parabolic rise (deviation) of ΔE_c above E_c ; the normalized change in capacitor potential $\Delta E_c/E_c$ is a parameter. Large ramp components are required to produce time constants that are small compared to t_s ; therefore, the distortion of the dc component in the circuit of Fig. 3 is immaterial as $\tau/t_s \rightarrow 0$. At the other extreme, when the time constant is very large compared to t_s , the inductance does not permit the current to follow voltage nonlinearities, and distortions again approach zero. The scanning circuits developed for a 1- to 30-kHz range operate above and below $\tau/t_s = 1$, so that the region of maximum distortion is liable to be encountered.

The relationship between capacitor size and maximum voltage change ΔE_c may be approximated (neglecting resistive losses) from the following equation:

$$\Delta E_c = \frac{1}{C} \int_0^{t_s/2} i dt, \quad [1]$$

where the ramp current i is $I_{pp}t/t_s$ and I_{pp} is peak-to-peak switch current.

Solution of Eq. [1] for capacitance C yields

$$C = \frac{I_{pp} t_s}{8 \Delta E_c} \quad [2]$$

The capacitor (battery) potential required for the current ramp is

$$E_c = L_y' \frac{I_{pp}}{t_s} \quad [3]$$

For a percentage change, K , in E_c ,

$$\Delta E_c = K E_c = K L_y' \frac{I_{pp}}{t_s} \quad [4]$$

From Eq. [2]

$$C = \frac{t_s^2}{8 K L_y'} \quad [5]$$

From the graphical evaluation of maximum distortion in Fig. 3, the following relationship may be obtained:

$$K \approx \frac{\text{percent distortion}}{5} \quad [6]$$

Finally, maximum distortion and capacitor size, at least for levels of 3% or less, may be expressed as

$$C \approx \frac{5}{8 L_y' (\text{percent distortion})} t_s^2 \quad [7]$$

For a scanning rate of 5 kHz with $t_s = 200$ microseconds, $L_y' = 170 \mu\text{H}$, and percent distortion = 0.25, the required value of C is $600 \mu\text{F}$; at a 1-kHz scanning rate, the capacitor size would have to be 25 times larger, or $15,000 \mu\text{F}$. Therefore, a circuit in which capacitors are changed with scanning rate is suggested as one means for keeping capacitor size reasonable. For example, C_1 may be switched from a value of $600 \mu\text{F}$

at 15 volts for the 5-kHz scanning rate to a 20- μ F, 75-V unit at 30 kHz. The circuit of Fig. 1, however, uses a 600- μ F 150-V capacitor for both 5- and 30-kHz rates.

The ramp-voltage component E_R must be equal to the potential impressed across the switch-circuit resistance E_{R_0} . A mismatch produces a nonlinearity whose value can be determined by graphical analysis. Fig. 4 shows the distortion produced by a ramp-voltage mismatch, with the inductive time constant as a parameter. The graph shows that the ramp generator must produce essentially the full ramp magnitude for slow-scan conditions (where typically τ is less than t_s) to keep distortion below the 1% level.

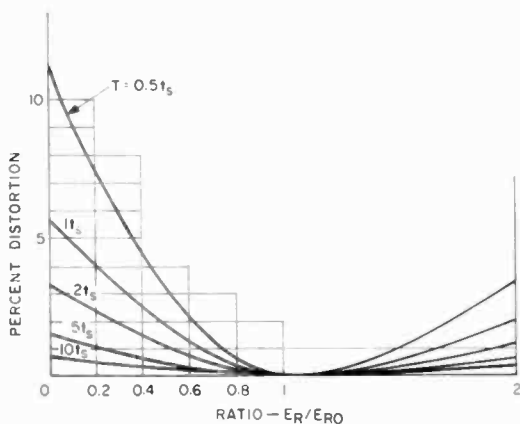


Fig. 4—Distortion produced by a ramp-voltage mismatch; parameter, inductive time constant.

Transformer Requirements

Transformers T_1 and T_2 in Fig. 1 must be carefully designed if good performance is to be obtained over a broad scanning-rate range. Excitation current must not be excessive at low scanning rates; thus, sufficient primary inductance must be provided. Coupling between windings must be good so that leakage inductance does not adversely affect the wave shape at fast scanning rates. Core and copper losses should be minimized, and winding capacitances balanced for most effective control of ringing. In addition, permeability must be uniform within the maximum flux excursion. Such properties are more easily attained in a transformer of practical size if direct currents are excluded from the windings. It also appears that ferrite cores are more

suitable than tape-wound silicon-iron cores.

Tape-wound cores were used in the driver transformer and ramp auto-transformer in an early deflection circuit. Material data indicated that permeability values near 50,000 should produce a primary inductance of 40 mH in the driver transformer, but subsequent measurements showed that only 1 mH was obtained. The reason for the dis-

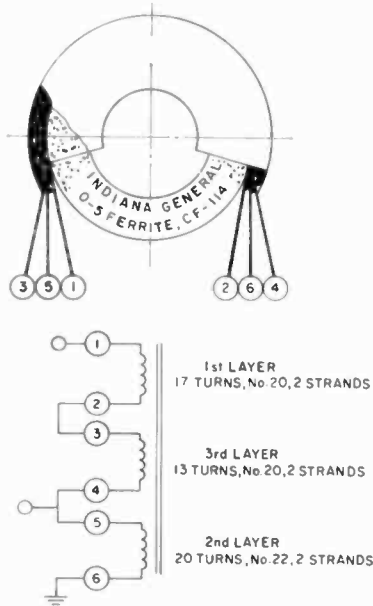


Fig. 5—Construction of the ramp autotransformer.

crepancy was not resolved and, because additional tests continued to show iron saturation and low inductance, a change was made to ferrite cores. Moderate increases in size were required for operation at a permeability value of 3000, but specifications and actual test measurements were in agreement for both driver transformer and ramp auto-transformer designs; consequently, the ferrite-core transformers were adopted. Table I gives the specifications and measured performance values of various transformer designs. Note the superior coupling (low-leakage inductance percentages) obtained in the ferrite designs by splitting and overlapping the windings. In addition, note that H_{max} in the ferrite cores is conservatively below the saturation value, making possible the extension of slow-scan operation to 1 kHz with little or no change in transformer design.

The ramp autotransformer is shown in Fig. 5. Two-strand windings

Table I—Comparison of Horizontal-Deflection Transformers

Core	Driver Transformer		Ramp Auto-Transformer	
	Tapewound Silicon-Iron toroid	(2) CF-618 0-5 Ferrite (2) C-cores	Tapewound Silicon-Iron toroid	CF-114 0-5 Ferrite toroid
Area (cm ²)	0.151	1.01	0.151	0.60
Length (cm)	8.97	16.0	6.98	8.0
Primary (turns/No. wire)	60T/No. 22	48T/No. 18	54T/No. 21	48T/No. 18
Secondary (turns/No. wire)	300T/No. 25	228T/No. 22	21T/No. 21	19T/No. 18
R_{pri} (milliohms)	243	76	62	37
R_{sec} (milliohms)	980	830	24.8	14.8
L_{pri} (millihenries)	1.2	5.8	0.33	6.8
L_{leak} (microhenries)	44	6	14	36
Coupling	0.963	0.9990	0.957	0.9950
5-kHz X_L (ohms)	38	182	10.4	214
μ (calculated)	1580	3200	415	3140
H_{max} (oersteds) (calculated)	3.0	0.28	5.9	0.23
H_{sat} , oersteds	0.2-0.4	1-2	0.2-0.4	1-2

are used to simplify wire layout to make winding easier. The first and second layers are wax-impregnated and tape-covered to form a continuous surface for subsequent layers. The primary is split for better coupling to the secondary. An earlier design using a single, tapped layer that completely covered the core had 10 times the leakage inductance, as shown in Table I.

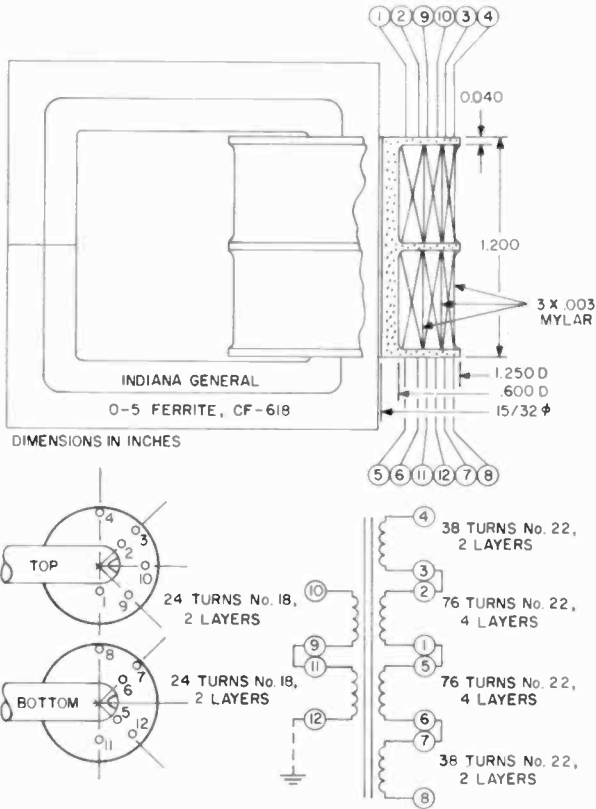


Fig. 6—Driver-transformer coil and winding details.

Fig. 6 shows the driver-transformer coil and winding details; the secondary is split for good coupling, and windings are sectionalized to balance capacitances. The relatively heavy wire used for the windings must be carefully wound on the polystyrene form to approach the full number of secondary turns. Experience has shown that even the most careful winding will not quite produce a nominal 1:5 turns ratio. Each layer is separated by one thickness of 0.003-inch Mylar tape of

full winding width. A triple thickness of the same material is used between winding sections. The locations at which wires pass through the coil flanges assure minimum surface-voltage gradients. The C-cores of the driver transformer are clamped together and chassis mounted by two brass screws. Both the driver transformer and the ramp auto-transformer are cool to the touch in operation.

Development of the Ramp Amplifier

The section of this paper on General Circuit Description and Performance stressed the need for a constant blocking-capacitor potential and linear ramp waveform to achieve linear deflection in the ideal circuit. The blocking-capacitor choice is easily evaluated: either the capacitor is of sufficient size, or it is not. The achievement of a linear, 1-MHz, ramp amplifier requires considerably more effort. It was found both convenient and advisable to separately develop a linear, stable, ramp amplifier and to evaluate its performance when operating into a resistive load; the observations noted in this section were made with the ramp transformer terminated in 5- and 0.5-ohm resistors. In the absence of a flyback pulse, the amplifier sweep was triggered by an auxiliary multivibrator.

The horizontal ramp generator and amplifier are described in detail in Fig. 7. At the left in the figure, an RCA-CA3000 constant-current generator charges a sweep capacitor, which is shorted during the retrace period. A slow/fast-scan logic whose ratio is adjusted by the Fast Ramp Set potentiometer selects the generator charging rate; correction for the degree of zoom is made by capacitor selection. The waveform is coupled through a 3N128 MOS transistor whose drain is modulated in accordance with its source potential so that dissipation is restricted at moderately high current levels and a linear transfer characteristic is maintained. A portion of the 20-V ramp is applied to a passive feedback network whose summing point drives the low-noise input of a quasi-complementary amplifier. Because the resistance of the autotransformer is so very low, even a small dc potential on its primary could cause a substantial magnetizing force. Therefore, capacitive coupling is used. The DC Set control in Fig. 7 is adjusted for about 0.5 V of capacitor potential.

A prototype amplifier, unlike the final version described in Fig. 7, took a feedback signal from the emitter/collector output point situated just before the coupling capacitor. A series of transformer tests made on this early amplifier are presented in Figs. 8 through 10. Fig. 8(a)

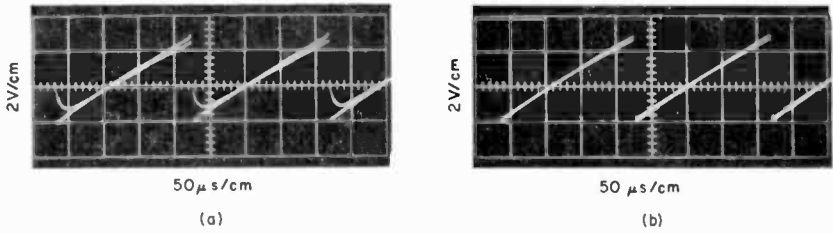


Fig. 8—Output of (a) wound-core design and (b) ferrite-core design at 5 kHz into 1/10 maximum and maximum-rated resistive loads showing improvement in performance of ferrite-core over wound-core design.

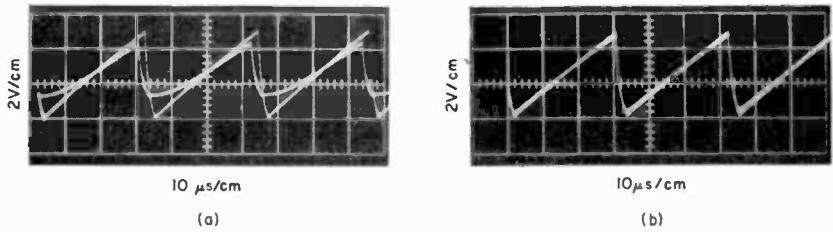


Fig. 9—Output of (a) wound-core design and (b) ferrite-core design at 30 kHz into 1/10 maximum and maximum-rated resistive loads showing improvement in performance of ferrite-core over wound-core design.

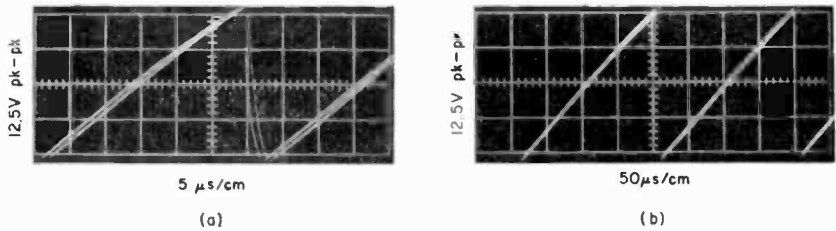


Fig. 10—The current ramp at the transformer primary in an early amplifier design with a resistive load: (a) the ramp at 30 kHz, (b) the ramp at 5 kHz.

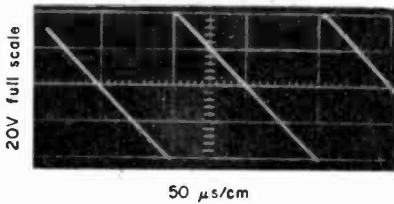


Fig. 11—The 5-kHz waveform produced by the latest ramp-generator circuit.

shows the output of a wound-core-design 5-kHz ramp transformer into one-tenth-maximum- and maximum-rated resistive loads. Both loading and leakage effects are substantial, even at this low scanning rate, and excitation current peaks of 700 mA were measured. The ferrite-core design shown in Fig. 8(b) performs better. Figs. 9(a) and 9(b) describe repeats of these tests at 30 kHz where the leakage inductance differences of the two designs are more dramatic. In all four figures, the ramp shows evidence of an exponential rise. The same rise is also apparent in Figs. 10(a) and 10(b), which were recorded at the transformer primary. This degree of nonlinearity was considered excessive, particularly for 1-kHz slow-scan applications, and a new generator design was undertaken.

Fig. 11 shows the 5-kHz waveform produced by the latest generator design as observed at the Ramp potentiometer. Previous tests of this generator design in vertical circuits showed the waveform nonlinearity to be less than 0.1%.¹ The 5-kHz output at the transformer secondary is shown in Fig. 12. Linearity is improved, but evidence of leakage inductance and winding resistance still exists. Amplifier distortion for a 5- and 0.5-ohm resistive load is shown in Fig. 13. The input and feedback waveforms have been applied to the extremities of a 10-turn

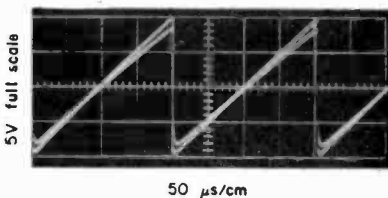


Fig. 12—The 5-kHz output at the secondary of the amplifier transformer with feedback from primary.

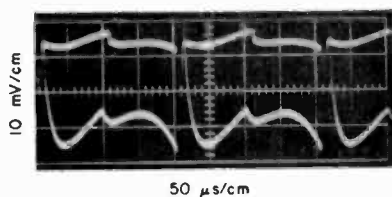


Fig. 13—Amplifier distortion with 5- and 0.5-ohm resistive loads with feedback from primary.

100,000-ohm potentiometer; the signal is taken from the potentiometer slider, which has been adjusted to obtain the most horizontal oscilloscope trace. The central jog in the waveform is crossover distortion in the output stages. An attempt has been made to balance circuit capacitance by adding a trimmer capacitor on one leg of the potentiometer, but complete neutralization is not always feasible, as shown at the left of the full-load curve. The deviation from a horizontal trace is seen to be about ± 5 mV out of the 12.5 V signal, a distortion of less than 0.05%. Therefore, in the tests that follow, distortions in excess of about 0.1% can be attributed to components other than the ramp amplifier.

Fig. 14 shows the potential developed across the 2000- μ F coupling capacitor. The major component of this waveform is due to a capacitor series resistance of about 0.1 ohm. The capacitive effect is a smaller parabolic component visible on the ramp. A large portion of the deviation from a constant potential is therefore a linear one, and affects only the regulation due to load changes.

Fig. 15(a) shows the 30-kHz output at the transformer secondary in a circuit employing feedback from the transformer primary. Leakage inductance affects linearity in early portions of the ramp. At the right in Fig. 15(b), feedback from the transformer secondary provides

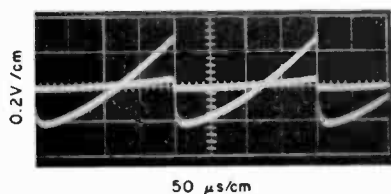


Fig. 14—Potential developed across the 2000- μ F coupling capacitor under 1/10 and full-load conditions.

significant compensation for leakage effects; this method is used in the present circuit. In fact, an increase in feedback gain to 26 dB presently produces even better wave shapes.

The series of tests conducted with resistive loads was terminated at this stage of the development; the following observations were made with the entire deflection circuit in operating condition.

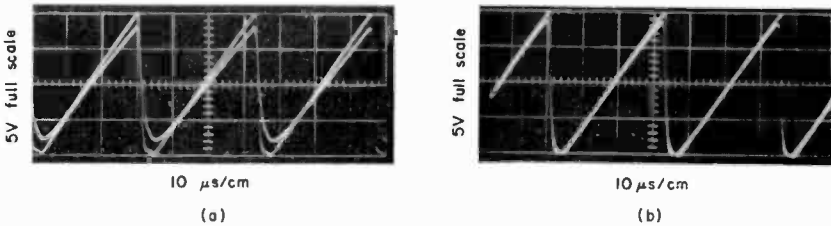


Fig. 15—The 30-kHz output at the transformer secondary in a circuit employing feedback from (a) the transformer primary, (b) the transformer secondary.

Deflection-Circuit Operation

A schematic of the horizontal switching circuit is shown in Fig. 16; the horizontal-switch transistor circuitry is represented by point S and the ramp generator by point R. At the left of the figure is the current generator. The resistive divider on the zoom selector and the Width potentiometer control the voltage appearing at the choke input for a particular scanning mode. Logic circuits regulate control potential levels and power supplies as required for slow- and fast-scan modes. Across the secondary of T_1 is a circuit that damps ringing. Capacitor adjustment is reasonably critical and is accomplished by monitoring current on a $\frac{1}{2}$ -ohm resistor inserted in the center tap of T_1 . The network on the yoke is the same as that found in broadcast deflection circuits and is intended to balance capacitive currents in the windings. DC centering is accomplished by use of a complementary output stage, and is capable of full format excursions to aid in developmental camera-tube evaluations.

The full-scan 5-kHz yoke current is shown in Fig. 17(a); this measurement was taken with a $\frac{1}{2}$ -ohm resistor inserted at the center tap of the yoke. At first, linearity appears good, but a critical appraisal shows the commutation of damper and horizontal-switch currents and the nonlinear dips on either side of the curve. Fig. 17(b) shows the

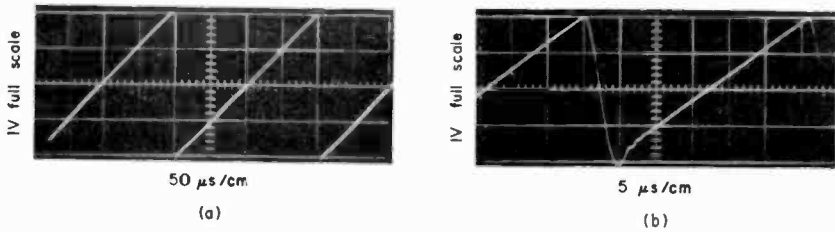


Fig. 17—(a) 5-kHz and (b) 30-kHz yoke current under full-scan conditions.

30-kHz full-scan yoke current; some ringing is apparent at the beginning of the trace. In subsequent tests in the television chain the ringing was visible at the extreme left of the picture; attempts to reduce the ringing further are considered necessary. Figs. 18(a) and 18(b) show the same scanning conditions at the secondary center tap of the driver transformer. In the figures, linearity is visibly poorer and commutation much more apparent; substantial ringing is evident under fast-scan conditions. The primary reason for displaying these waveforms is that they were compared to the (linear) input ramp to determine the distortions. It was not practical to compare the actual yoke-current waveforms to the input ramp because of unsolved pick-up problems. Therefore, the distortion wave shapes shown in Fig. 19(a) and 19(b) are worst cases to the degree that the secondary waveforms are poorer than those of the yoke. If the commutation pulses (which are not evident in the yoke current) are disregarded, the nonlinearity in the 5-kHz curve is less than ± 5 mV out of 1 V, or less than 0.5%. The 30-kHz nonlinearity is probably less than 0.3% although difficulties with circuit capacitance neutralization restrict viewing of the entire distortion waveform.

The distortions shown in Figs. 19(a) and 19(b) are primarily a

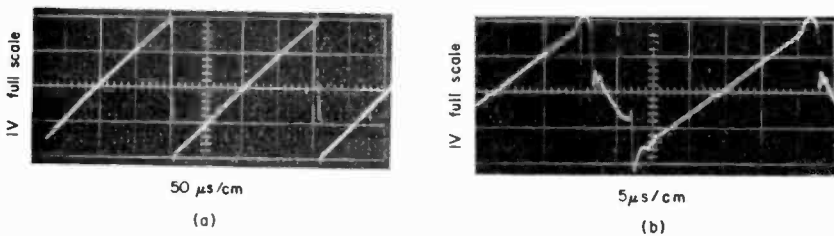


Fig. 18—(a) 5-kHz and (b) 30-kHz drive-transformer secondary current.

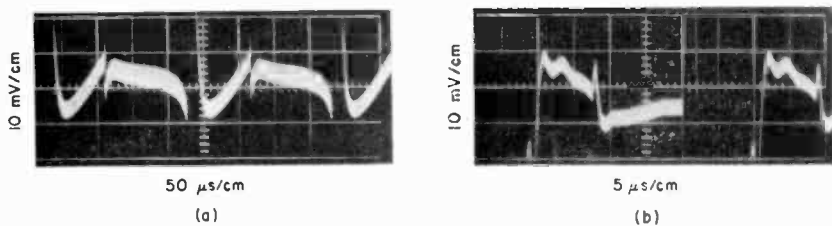


Fig. 19—Nonlinearity observed by comparing secondary-current and ramp generator waveforms at (a) 5 kHz and (b) 30 kHz.

result of a change in the switching-circuit resistance when conduction changes paths from damper to horizontal switch. A single ramp cannot properly compensate for varying resistance values, and a compromise solution must be sought. It is possible to add resistance to the lower value, but the dynamic changes still occur. A greater (constant) resistance elsewhere in the switching circuit could reduce this distortion at the expense of greater ramp power and “loss” of inductive time constant, but the effectiveness of this approach is limited.

The 30-kHz 20-to-1 zoom mode of Fig. 20 contains a sizable distortion due to resistance differences. Fig. 20(b) shows the diode and switch potentials present in the zoom mode; the resistance inequality becomes obvious when the zero-potential trace is considered. Fortunately, the much reduced power levels of the large zoom modes permit class-A operation of the horizontal switch. By adjusting the drive-waveform multivibrator so that the commutation point is moved to the extreme left of the trace, superior linearity may be achieved. Fig. 21 contains the horizontal-drive and switch schematic and includes the drive-waveform controls.

Also shown in Fig. 21 are the 2N3512 switch drivers that were a part of the initially developed amplifier, but that were destroyed during a testing mishap; slower, higher-capacitance 2N2102 transistors

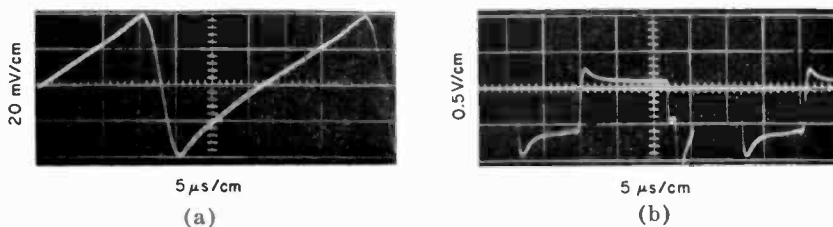


Fig. 20—(a) The 30-kHz yoke current at a 20-to-1 zoom ratio and (b) collector voltage on the horizontal-switch transistors in the 20-to-1 zoom mode.

were used while awaiting replacements. The 3- μ s period required to sweep out the switch charge shown in Fig. 22 is considered excessive and complicates system sync considerations. The emitter leads of the Delco DTS 402 transistors are linked by one turn through a ferrite bead, a good, low-loss method for apportioning currents. The 3.5-A collector-current rating, 700-V V_{CEX} , and 1.2- μ s fall-time rating of these transistors ensures conservative operation. Fig. 23 shows the 500-volt 6- μ s flyback pulse imposed on the switch collectors at fast scan. This pulse (in the form shown in Fig. 24) also triggers the ramp generator through a zener network.

In the event that the flyback pulse exceeds 600 V, a 2N3228 SCR is triggered and removes the supply voltage from the switch drive-waveform generator. A sweep-failure logic circuit should therefore be provided for camera-tube or kinescope protection. A possible alternative to the use of a logic circuit requires the removal of the SCR's and the absorption of the voltage surge in zener diodes without interrupting the scanning cycle. Fig. 25 shows the 30-kHz ramp-generator waveform at full scan. The waveform indicates that, at the negative extreme, the ramp should be slightly reduced to avoid clipping at the 2N2102 charging transistors.

Considerations for Circuit Improvements and Extended Operation

Circuit performance could be improved if it were feasible to extend the feedback loop around driver transformer T_1 . A 0.5-ohm sensing resistor at the transformer or yoke center tap would produce a 1-V signal at full scan; a (linear) differential amplifier with a gain of 5 to 8 could match the ramp-generator level. A successful design incorporating these circuit improvements would provide several benefits: feedback compensation for T_1 , and a reduction of the commutation pulse in the secondary circuit. These circuit changes might also make the choice of capacitor C_1 more flexible because it would be included in the feedback loop. In the event that the circuit modifications proved unsuitable, good performance at 1 kHz would still be possible if the capacitor network described in the section of this paper on Development of the Ramp Amplifier were used in place of C_1 . Capacitors C_c would also be increased in size to accommodate the network.

Measurements of circuit noise and supply stability have not been made because of time limitations. If the ramp-generator signal proves adequate, it may be possible to reduce its level to 10 V so that the generator can run from the -15-volt line. With a few other minor

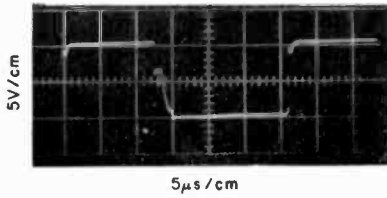


Fig. 22—The drive waveform at the bases of the horizontal-switch transistors at 30 kHz.

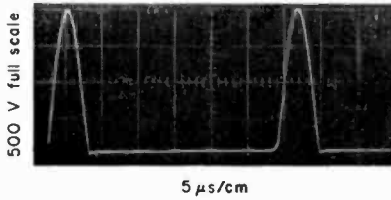


Fig. 23—The flyback pulse on the switch transistors under full-scan conditions at 30 kHz.

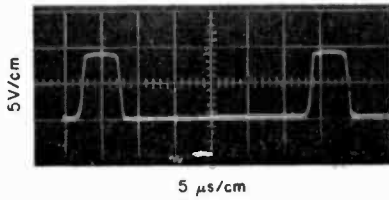


Fig. 24—Ramp generator trigger pulse at 30 kHz.

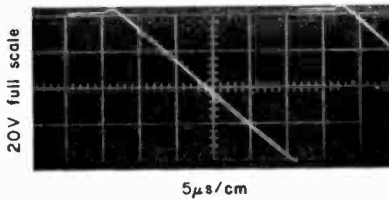


Fig. 25—The 30-kHz ramp-generator waveform.

changes, the -30 volt supply could then be removed. The values of resistance used in the potential-divider that controls zoom require minor adjustments, and the ramp component should be re-evaluated to assure the best compromise under zoom conditions. Provision could also be made for "automatic" selection of class-A operation in the zoom modes. A better method of width control is desirable for a greater range of scanning rates.

Further circuit development by O. H. Schade, Sr. and C. Trushell subsequent to the writing of this paper has produced superior performance. It was found that the 2N3512 driver circuit for the switch transistors could be optimized for 1- μ s turn-off time. These changes have been reflected in the schematic of Fig. 21. In addition, a change to a lower-impedance deflection yoke permitted a reduction of the turns ratio of transformer T_1 to 1:2.5. Auto-transformer secondaries were wound on the same core; the existing primary windings were utilized. As a result, coupling was improved and ringing was greatly reduced, suggesting that a direct-drive circuit could be used beneficially.

Finally, suitable protection circuits must be designed, built, and tested. The operation of a flexible, high-definition television chain for the testing of developmental components requires careful deliberation if costly failures are to be avoided.

Acknowledgments

The author thanks D. F. Dion for providing prototype circuit information, transformer cores for evaluation, and much helpful discussion of circuit operation; C. Trushell for designing decoupling and centering circuits, laying out and building all circuitry and transformers, and ably assisting during the troubleshooting phases of development; many Somerville engineers for providing circuit information, supplying developmental dampers, and aiding in the choice of commercial devices; and O. H. Schade, Sr., for helping to delineate the need for good solid-state horizontal circuits and advising during development.

References

- ¹ Schade, Jr., O. H., "Stable Solid-State Vertical Deflection for High-Definition Television System," *RCA Review*, March 1970.
- ² Wheatley, C. F., "Design Considerations for Transistorized Television Deflection Circuits," *IEEE Trans. Broadcast and TV Receivers*, July 1963.

October

- "Coherent Microwave Instabilities in a Thin-Layer Solid-State Plasma," G. A. Swartz and B. B. Robinson, **Jour. Appl. Phys.**
- "Computer Optimization of Recognition Networks," H. Drucker, **IEEE Trans. GC**
- "The Heterode Strain Sensor: An Evaporated Heterojunction Device," R. M. Moore and C. J. Busanovich, **IEEE Trans. GED**
- "Laser Writing," R. S. Braudy, **Proc. IEEE (Letters)**
- "Microwave Oscillation in Al(x)Ga(1-x) As Avalanche Diodes," C. Yeh, S. G. Liu, and F. Z. Hawrylo, **Proc. IEEE (Letters)**
- "A Neglected Form of Technical Communication—The New Product Release," H. K. Mintz, **IEEE Trans. GEWS**
- "Noise Power Spectrum Characteristics for an He-Ne Laser Operating under Various Discharge Conditions," A. Waksberg and J. Wood, **Rev. Sci. Instr.**
- "A Qualitative Model of the Avalanche Diode," B. B. Robinson, **Proc. IEEE (Letters)**
- "RCA . . . Pioneer in Pacific Communications," H. A. Mortara, **Signal**
- "A Review of the Issue," I. M. Seideman, **IEEE Trans. GEWS**
- "Stabilization of Supercritical Transferred-Electron Amplifiers," F. Sterzer, **Proc. IEEE (Letters)**
- "Energy Levels of Ce(2+) in CaFe," R. C. Alig, Z. J. Kiss, and Coauthors, **Phys. Rev.** (10 October)
- "200-Watt IC Stereo Amplifier," J. C. Sondermeyer and Coauthor, **Radio-Electronics**
- "Absorption of Oxygen in Silicon in the Far Infra-red," W. Hayes and D. R. Bosomworth, **Phys. Rev. Letters.** (13 October)

November

- "Are Strong Irradiance Fluctuations Log Normal or Rayleigh Distributed?" D. A. De Wolf, **Jour. Opt. Soc. Amer.**
- "Automated Plating for Printed Circuits," H. F. Scheilack, **Solid-State Tech.**
- "Comparison of Liquid-Encapsulated and Solution-Grown Substrates for Efficient GaP Diodes," I. Ladany, S. H. McFarlane III, and Coauthor, **Jour. Appl. Phys.** (Communications)
- "Design of an Ultra-Portable Color Television Camera System," M. H. Mesner, F. Lang, D. Binge, and F. J. Bingley, **Jour. SMPTE**
- "Holography and Parametric Image Conversion: Part II" A. H. Firester, **Jour. Appl. Phys.**
- "A Low-Loss N-Way Optical Power Divider for a Ku-Band Low Sidelobe Phased Array," C. E. Profera, Jr., **Microwave Jour.**
- "A Method of Measuring Phase Jitter Statistics for Very High Repetition Rate Pulses," A. L. Waksberg and J. I. Wood, **Rev. Sci. Instr.** (Notes)
- "Parametric Image Conversion: Part I," A. H. Firester, **Jour. Appl. Phys.**
- "Conduction-Induced Alignment of Nematic Liquid Crystals: Basic Model and Stability Considerations," W. Helfrich, **Jour. Chem. Phys.** (1 November)

December

- "Coherent Emission from Indium Antimonide with Closely Spaced Coplanar Contacts," G. A. Swartz, **Jour. Appl. Phys.**
- "Designing High-Frequency Diffused Resistors," R. E. Kleppinger, **RCA Review**
- "Digital Logic for Radiation Environments: A Comparison of Metal-Oxide-Semiconductor and Bipolar Technologies," W. J. Dennehy, A. G. Holmes-Siedle, and K. H. Zaininger, **RCA Review**
- "Effects of Transverse Magnetic Field for He-Cd Laser," K. G. Hernqvist, **Jour. Appl. Phys.** (Communications)

- "Hybrid Integrated 10-Watt CW Broad-Band Power Source at S Band," E. F. Belohoubek, A. Rosen, D. M. Stevenson, and A. Presser, **IEE Jour. Solid-State Circuits**
- "Integrated-Circuit Metalized Plastic Symmetrical Millimeter Trough Waveguide System with Nonreciprocal Elements," C. P. Wen, **RCA Review**
- "A Multiple Computer Linkage," O. Aberth, **IEEE Trans. GC (Short Notes)**
- "Parallel Processing for Phased-Array Radars," J. E. Courtney and H. M. Halpern, **RCA Review**
- "A Photodetector Array for Holographic Optical Memories," J. M. Assour and R. D. Lohman, **RCA Review**
- "Prediction of the Dielectric Behavior of Titanate Dispersions," J. M. Guiot, **RCA Review**
- "Pulsed Heat Conduction in a Layered Semiconductor-Metal Transferred-Electron Oscillator Geometry," B. S. Perlman, **RCA Review**
- "Radiative Recombination and Equilibrium between Near-Band-Edge Tail States in n-Type GaAs," P. D. Southgate, **Jour. Appl. Phys.**
- "A Reflex Electro-Optic Light Valve Television Display," D. H. Pritchard, **RCA Review**
- "Stabilized Supercritical Transferred Electron Amplifiers," T. E. Walsh, B. S. Perlman, and R. E. Enstrom, **IEEE Jour. Solid-State Circuits**
- "Study of Noise in Television Broadcast Equipment," K. Sadashige, **Jour. SMPTE**
- "A Technical and Economic Appraisal of the Use of Microwave Energy in the Freeze-Drying Process," A. C. Grimm, **RCA Review**
- "Transferred Electron Amplifiers," F. Sterzer, **IEEE Jour. Solid-State Circuits**
- "Tunable L-Band High-Power Avalanche-Diode Oscillator Circuit," P. A. Levine and S. Liu, **IEEE Jour. Solid-State Circuits**
- "UHF Integrated Power Amplifiers," W. E. Poole, **IEEE Jour. Solid-State Circuits**
- "A Word-Organized Photodetector Array," D. H. R. Vilkomerson, R. S. Mezrich, and J. M. Assour, **IEEE Jour. Solid-State Circuits**
- "Nonlinear Coloration Effects in Transition-Metal-Doped SrTiO₃ Crystals," J. J. Amodèi, **Phys. Rev.** (15 December)
- "Polaron Effects in Semiconducting CdF₂: Cyclotron Resonance and Far-Infrared Properties,(2)" D. R. Bosomworth and Coauthors, **Phys. Rev.** (15 December)
- "Sound Absorption in Liquid Helium Below 0.6 K," R. K. Wehner and R. Klein, **Phys. Rev. Letters** (15 December)
- "Optical Properties of Single-Crystal Films of CdCr₂S₄," S. B. Berger and L. Ekstrom, **Phys. Rev. Letters** (29 December)

Patents Issued to RCA Inventors Fourth Quarter 1969

October

- Wayne M. Austin**, System for Producing Indications of Time Relationship of Electrical Signals (3,473,052)
- Appleton D. Cope, Eduard Leudicke and Ojars J. Ziemelis** Television Camera Including an Image Isocon Tube (3,471,741)
- Luke Dillon, Jr.** Integrated Arrangement for Integrated Circuit Structures (3,474,094)
- Joseph J. Hanak** Deposition of Crystalline Niobium Stannide (3,472,694)
- Michael F. Lamorte and Paul Nyul** Method of Making Diode Arrays (3,471,923)
- Charles B. Meyer** Automatic Lamp Changing Apparatus (3,471,745)
- Austin J. Mortimer** Self-Regulating Switching Circuit (3,471,771)
- Frederick H. Nicoll** Methods of Electrophotographic and Electrostatic Recording (3,475,170)
- William N. Parker** Dielectric Heating (3,474,209)
- Robert F. Sanford** Synchronization System for Television Signals with Auxiliary Information Transmitted During the Vertical Blanking Interval (3,472,962)
- Joseph H. Scott, Jr.** Vapor Deposition of Silicon-Nitrogen Insulating Coating (3,472,689)
- John Stark, Jr.** Automatic Frequency Control (RE26686)
- George F. Stockdale** Glass Seal Manufacture (3,472,640)
- Richard G. Stoudenheimer and Lawrence A. Ezard** Image Tube Having a Gating and Focusing Electrode (3,474,275)
- Chih C. Wang** Growing Monocrystalline Stoichiometric Magnesium Aluminate (3,472,615)
- Donald H. Willis** Video Amplifier Transient Response Control Circuit (3,472,954)

November

- James A. Amick** Method of Depositing Refractory Metals (3,477,872)
- Robert L. Bailey and Claude E. Doner** Paralleling Active Circuit Elements (3,477,032)
- William H. Barkow** Penetration Color Displays (3,478,245)
- Frederick W. Brill and Morris R. Weongarten** Method of Cleaning Stem Leads for Electron Devices (3,477,835)
- Donald R. Carley** Strip-Line Power Transistor Package (3,478,161)
- George W. Carter** Gain Control Biasing Circuits for Field-Effect Transistors (3,480,873)
- James F. Delany and Gerard O. Walter** Photocomposing Apparatus Support Structure (3,479,934)
- Nicholas A. Del Vecchio** Timing Arrangement for Document Processor (3,480,762)
- George J. Gilbert** Encapsulation and Connection Structure for High Power and High Frequency Semiconductor Devices (3,479,570)
- Milton J. Grimes, Donald F. Henrikson, and Herbert R. Meisel** Method of Providing Contact Leads for Semiconductors (3,478,420)
- Joseph J. Hanak** Magnetic Heads (3,479,738)
- Leopold A. Harwood** Linear Frequency Modulation System Including an Oscillating Transistor, an Internal Capacity of which is Varied In Accordance with a Modulating Signal (RE26,715)
- Fred Herzfeld and Frans Van Hekken** Cathode Ray Tube and Method of Manufacture (3,476,025)
- Charles J. Hirsch** Converter for VHF-Omnirange (VOR) Receiver (3,478,360)
- Neal W. Hursh and Ronald R. Mooreland** Shield (3,479,566)
- Bernard J. Lechner** Ferroelectric Control Circuits (3,478,224)

- Abraham Lichowsky** Data Storage Apparatus Including Laminated Annuli Transducer Supports Concentric with the Data Storage Means (3,478,339)
- Zeev Lieser** Condition Indicator for Appliance (3,480,940)
- Donald H. Montgomery** Memory Driver Monitoring Circuit (3,479,650)
- Philip E. O'Connell** Spindle Adapter (3,477,727)
- Louis Pensak** Testing for the Presence of a Contaminant in an Insulating or Semiconducting Medium (3,478,260)
- Orville T. Rhyne** Hybrid Circuit Arrangement (3,479,617)
- Paul H. Robinson** Assembly Having Adjacent Regions of Different Semiconductor Material on an Insulator Substrate and Method of Manufacture (3,476,617)
- Ralph E. Simon, Brown F. Williams, and Ralph Wasserman** Photo-multiplier or Image Amplifier with Secondary Emission Transmission-Type Dynodes Made of Semiconductive Material with Low Work Function Material Disposed Thereon (3,478,213)
- Walter F. Speer and James M. Simmons** Detent System (3,477,299)
- Chitoor V. Srinivason** System for Automatic Correction of Burst Errors (3,478,313)
- Martin C. Steele and Francesco P. Califano** Production of Amplitude Modulated Light by a Solid State Oscillator (3,477,041)
- David A. Vigil** Method of Spacing a Plurality of Magnetic Heads from the Surface of a Magnetic Drum (3,478,262)
- Lawrence P. Wennik and Phillips B. Scott** Electrical Neuron Circuit that Includes an Operational Amplifier (3,476,954)

December

- George E. Anderson and Donald H. Willis** Video Peaking Control Network (3,487,165)
- Alda V. Bedford** Self-Propelling Hose (3,485,237)
- Walter H. Buchsbaum** Protective System (3,482,243)
- Te N. Chin** Magnetostrictive Delay Line Having a Flat, Thin Sheet of Magnetostrictive Material (3,482,191)
- Louis S. Cosentino and Wilber C. Stewart** Cryoelectric Memories (3,482,220)
- Andrew G. F. Dingwall** Thermoelectric Device with Embossed Graphite Member (3,485,679)
- Ronald E. Enstrom and John R. Appert** Superconductors (3,484,208)
- Gardner L. Fassett and Marinus Van Renssen** Cathode Ray Tube Manufacture (3,482,286)
- Robert A. Gange and Eugene M. Nagle** Balanced Matrix Driver Arrangement (3,483,517)
- William A. Gottfried** Printed Circuit Boards (3,483,615)
- Dal F. Griepentrog** Intermediate Frequency Coupling Network Having a Sharply Tuned Sound Carrier Cancellation Trap Inductively Coupled to the Input Circuit (3,487,339)
- Karl G. Hernqvist** Sputter Resistive Cold Cathode for Low Pressure Gas Discharge Device (3,486,058)
- William L-C Hui and George R. Auth** Integrated Array of Thin-Film Photovoltaic Cells and Method of Making Same (3,483,038)
- Leonard A. Kaplan and Oliver P. Hart** Automatic Gain Control System Employing Multiple Insulated-Gate Field-Effect Transistor (3,482,167)
- Werner Kern** Silicate Glass Coating of Semiconductor Devices (3,481,781)
- Arnold Matzelle and Arthur E. Hahn, Jr.** Three-Terminal Semiconductor Device for Converting Amplitude Modulated Signals into Frequency Modulated Signals (3,487,338)
- Henry E. Roys** Transducer with Curved Surface for Cartridge Tape Player (3,485,959)
- Anatole Turecki and Johnny Vallee** Multiple State Logic Circuits (3,482,172)
- Henry R. Warren** Asynchronous Drive System (3,481,214)
- Henry R. Warren** Wide Band Recording and Reproducing System (3,482,038)
- Cheng P. Wen** Laser Color Control (3,487,329)
- Robert O. Winder** Threshold Gates and Circuits (3,487,316)

AUTHORS



Bertrand E. Berson received his Bachelor of Electrical Engineering degree from City College, New York, in 1960; and his Master of Science degree from the University of Rochester, Rochester, New York, in 1963. He has had additional schooling at the University of Rochester, UCLA Extension, Mt. San Antonio Junior College, and the Newark College of Engineering. From 1962 to 1966 he was a Senior Physicist with General Dynamics in Pomona, California. While with General Dynamics he was involved in research in the areas of thin films and thin-film micro-electronics, organic semiconductors, and plasma oscillations in indium antimonide.

Since joining the RCA Advanced Technology Laboratory, Mr. Berson has been engaged in research in the area of GaAs and silicon microwave devices. He is presently leader of a group pursuing research in these areas.

Mr. Berson is a member of the IEEE and the American Physical Society.



Ronald E. Enstrom received the S.B., S.M., and Sc.D. degrees in metallurgy from the Massachusetts Institute of Technology in 1957, 1962 and 1963, respectively, and has had extensive experience working on various materials. From 1957 to 1960 he worked at Union Carbide and Nuclear Metals, Inc., on materials for high temperature oxidation resistance and nuclear fuel elements, respectively. At M.I.T., his doctoral thesis focussed on the metallurgy and superconductivity of the three compounds in the Nb-Sn system, and at RCA Laboratories he was instrumental in making Nb₃Sn ribbon a highly successful high-field magnet material.

More recently, Dr. Enstrom has worked on the vapor phase synthesis and characterization of GaAs and GaAs-GaP alloys for high power rectifiers and solid-state microwave oscillators, and on the vapor-growth of GaAs-InAs alloys for infra-red sensitive negative electron affinity photocathode applications.

Dr. Enstrom is a member of Sigma Xi, AIME, the American Physical Society, and the Electrochemical Society.



Paul G. Herkart received the B.S. and M.S. degrees in Electrical Engineering in 1935 from the Massachusetts Institute of Technology. From 1935 until 1943 he was engaged in power tube manufacturing at the RCA Victor Division in Harrison, N.J. Since 1943 he has been with the RCA Laboratories in Princeton, New Jersey. Mr. Herkart's early work was on television pick-up tubes, storage tubes, and color television. He later lead a group working in the technology and production of semiconductor materials (such as germanium, silicon, gallium arsenide, and gallium phosphide), thermo-electrics materials, (such as bismuth telluride and its associated alloys), and of other materials with diverse uses (such as cadmium mercury telluride, antimony sulfide, and cadmium arsenide). Mr. Herkart headed a Materials Technology Group at the Laboratory, working on III-V compounds and other alloys and compounds, thin-films production of cadmium sulfide, epitaxial growth of gallium arsenide, phosphors, and laser materials. He is presently involved in research on the lubrication of cadmium sulfide transducers for piezoelectric applications.

Mr. Herkart is a member of IEEE and of Sigma Xi.



Kaare Karstad majored in Electrical Engineering, graduating from Norway's Technical University, Trondheim, in 1942. While a postgraduate student in 1943, he worked as an instructor in radio engineering at the University. In early 1944 he was employed at the ASEA concern in Vesteråas, Sweden, in remote control techniques. For the next two years, Mr. Karstad was an officer in the Royal Norwegian Navy, serving Norway and Great Britain in the technical branch of underwater sound. From 1946 to 1952 he was in charge of the Sonar Section in the Electronics Department of the Norwegian Navy. From 1948 to 1950, on leave of absence and as an Honorary Fellow of the American Scandinavian Foundation, Mr. Karstad worked at the RCA Laboratories Division, Princeton, N.J., on television problems. He returned in 1952 as a member of the technical staff. A major part of his work has been research in the field of color television, including system and circuit work in receivers as well as transmitters and overall system evaluation of NTSC standards. A year and a half was spent at the RCA West Coast Electronic Product Division doing Systems Engineering in the field of Electronic Countermeasure Techniques, in the range of 8-12 kMHz. For a year he was active in the field of infra-red systems, primarily measuring and evaluating IR detectors. Since 1961 his work has encompassed instrumentation related to research in thin magnetic films and ferrites, pulse-circuit techniques, and selection matrices. Recently, the research has included the area of piezoelectric transducers and ultrasonics for generation and propagation of strain pulses for a digital magnetosonic storage system.

Dr. Karstad is a Senior Member of IEEE and a member of Sigma Xi.



Henry Kurlansik received a Bachelor's degree in Engineering Physics from Cornell University in 1962, and a Master's degree of Business Administration from Cornell in 1963. In 1965 he received a M.S. in Physics from the University of Pennsylvania, and is currently enrolled in the Moore School of Electrical Engineering, working toward the Ph.D. He joined RCA Laboratories in 1963, and worked in the areas of luminescence and integrated logic circuits. Most recently, he has worked in the field of thin magnetic films for use in computer memories.

Mr. Kurlansik is a member of IEEE, and Phi Kappa Phi.



Shing-gong Liu received his B.S. degree in electrical engineering from Taiwan University, Taipei, Taiwan, in 1954, the M.S. degree in electrical engineering from North Carolina State College, Raleigh, North Carolina, in 1958, and the Ph.D. degree in electrical engineering from Stanford University, Stanford, California, in 1963. From 1958 to 1959 he worked with the IBM Laboratories, Poughkeepsie, New York. He was a research assistant at the Hansen Microwave Laboratories, Stanford University, where he worked in the field of microwave ferrites. He joined RCA Laboratories, Princeton, New Jersey, in 1963, and has since worked

principally in the areas of semiconductor microwave devices.

Dr. Liu is a member of Phi Kappa Phi, Sigma Xi, and the American Physical Society.



Lubomyr S. Onyshkevych received a B.E.E. degree from City College of New York in 1955. He worked at the Research Laboratory of Electronics of the Massachusetts Institute of Technology in the area of multiaperture magnetic logic from 1955 to 1957, receiving a M.S. degree in Electrical Engineering in 1957. In 1957, he joined the RCA Laboratories where he worked in the areas of magnetic logic and memory systems, parametric oscillators, and tunnel diodes. In 1959 he returned to MIT, where he received the E.E. degree in 1962. During the period 1961-1963 he worked at the MIT Lincoln Laboratories, in the field of

thin magnetic film memories. In September 1963 he rejoined RCA Laboratories, where he has been working in the area of sonic film memories.

Mr. Onyshkevych is a member IEEE, Tau Beta Pi, Sigma Xi, and Eta Kappa Nu.



James F. Reynolds received his B.E.E., M.E.E., and Ph.D. from Rensselaer Polytechnic Institute in 1964, 1965, and 1967, respectively. His doctoral thesis investigated methods of stabilizing gaseous magnetoplasmas by controlling the magnetic field geometry. His earlier graduate research was concerned with the use of microwave techniques for plasma diagnostics. Since joining the staff of the Advanced Technology Laboratory of RCA in 1967, Dr. Reynolds has been working in the area of high power epitaxial GaAs Gunn effect devices.

Dr. Reynolds is an associate member of Sigma Xi.



John J. Risko graduated from RCA Institutes T-3 program in 1962 and is now an evening student at Newark College of Engineering. He joined RCA laboratories in 1962 and has worked in the research and development area of gallium antimonide tunnel diodes, gallium arsenide varactor diodes and more recently silicon avalanche diodes. He is currently engaged in work involving the high-efficiency mode avalanche diode.

Mr. Risko is an associate member of IEEE.



Rabah Shahbender received a B.E.E. from Cairo University, Cairo, Egypt, in 1946. He received an M.S. in Electrical Engineering from Washington University, St. Louis, Mo., in 1949, and a Ph.D. in Electrical Engineering from the University of Illinois in 1951. From 1946 to 1948 he was employed by the Anglo-Egyptian Oilfields Ltd. and undertook work in seismic exploration. From 1951 to 1955, he was on the staff of Honeywell, Brown Instruments Division, Phila., Penna., where he conducted research in the behavior of nonlinear closed loop systems. He joined RCA in Camden, N.J., in 1955, working in the areas of adaptive systems, nonlinear filters, electron beam devices, ultrasonic devices, and airborne fire control systems. He transferred to RCA Laboratories, Princeton, N.J. in 1959, where he has been active in the area of high-speed digital memory systems. He is presently Head of the Digital Devices Research in the Digital Systems Research Laboratory. From 1960 to 1966, Dr. Shahbender was Chairman of the Department of Electronic Physics, at La Salle College, Evening Division, Phila., Pa.

Dr. Shahbender is a Senior Member of Sigma Xi, and Eta Kappa Nu, and a Fellow of the University of Illinois.



Otto H. Schade, Jr., received the B.E.E. degree from Rensselaer Polytechnic Institute in June, 1953, after which he joined RCA's Receiving Tube Engineering Group at Harrison, N.J. His early work included the development of beam power tubes, damper diodes, and advanced electron devices, investigating their mechanical, thermal, high-voltage, and electron-optical requirements. In 1961, he took part in the feasibility study and initial development of thermoelectric modules for the SNAP-10A program, where he was responsible for electrical and thermal test and evaluation for the project. During 1963 and 1964, he designed and developed

high-efficiency gaseous fuel burners for T/E generators, which led to novel liquid-fuel burner designs. In 1966, Mr. Schade transferred to the RCA Somerville semiconductor activity, where he was responsible for design, development, and evaluation of silane deposition equipment, photomask alignment stages, and collimated-light printing techniques. This work was followed by steady-state and transient thermal analysis of failure mechanisms in overlay power transistors. In March 1968, he became engaged in the study and assisted in the development of a high-definition test facility at Harrison, N.J., where he worked on solid-state deflection circuits. Since May 1969, he has been active in the integrated-circuit design of operational amplifiers.

Mr. Schade is a member of IEEE and Eta Kappa Nu.



Otto H. Schade, Sr. was born and educated in Germany; he came to the United States in 1926. He joined RCA Electronic Components and Devices, Harrison, New Jersey, in 1931. Since 1938, he has specialized in television circuits, camera tubes, and picture tubes. From 1944 to 1957 he worked on a unified general method of image analysis and specification, including practical methods for measuring the "aperature" effect (square-wave and sine-wave response function) and fluctuation levels (noise) of optical, photographic, and electronic image-system components and the eye. He has had the responsibility for the thermal and

electrical design of nuvistor tubes. More recently, he has developed an accurate method for calculating the resolving power of television and photographic imaging systems to assist in the evaluation of high-definition television systems, and a new electron optic providing minimum aberrations and uniform focus in television camera tubes with larger (50 × 50 mm) image surfaces. Dr. Schade has received numerous honors, including the Modern Pioneers Award of the National Association of Manufacturers (1940), the Morris Liebmann Memorial Prize of the Institute of Radio Engineers (1950) and a Fellowship (1951) from the Institute of Radio Engineers. In 1951 he was made a Fellow, and also was the first recipient of the David Sarnoff Gold Medal Award, of the Society of Motion Picture and Television Engineers. In June 1953, he was invested with the honorary degree of Doctor of Engineering by Rensselaer Polytechnic Institute. In 1960, he received the Progress Medal Award of the Society of Motion Picture and Television Engineers for his outstanding technical contribution in the engineering phases of the motion picture and television industries.

LOHNES AND CULVÉR

MAY 25 1970

~~FILE~~ ~~ELD~~
~~ENC~~ ~~FDV~~

Statement of Ownership

Statement of Ownership, Management and Circulation (Act of October 23, 1962, Section 4369, Title 39, United States Code).

1. Date of filing: October 3, 1969. 2. Title of publication: RCA REVIEW. 3. Frequency of issue: Quarterly. 4. Location of known office of publication: RCA Laboratories, Princeton, New Jersey, 08540. 5. Location of the headquarters or general business offices of the publishers: RCA Laboratories, Princeton, New Jersey, 08540. 6. Names and addresses of Publisher, Editor, and Managing Editor: Publisher, RCA Laboratories, Princeton, New Jersey; Editor, C. C. Foster, RCA Laboratories, Princeton, New Jersey; Managing Editor, R. F. Ciafone, RCA Laboratories, Princeton, New Jersey. 7. Owner: RCA Corporation, 30 Rockefeller Plaza, New York, New York 10020. 8. Known Bondholders, Mortgagees, and other security holders owning or holding 1 percent or more of total amount of bonds, mortgages or other securities: Metropolitan Life Ins. Co., 1 Madison Ave., New York, New York; New York Life Ins. Co., 51 Madison Ave., New York, New York.

I certify that the statements made by me above are correct and complete.

Ralph F. Ciafone, Managing Editor

